

**ISET JOURNAL OF EARTHQUAKE TECHNOLOGY**

Vol. 46

No. 2

June 2009

**CONTENTS**

<b>No.</b>	<b>Paper</b>	<b>Page</b>
503	Performance of Exterior Beam-Column Joints under Seismic Type Loading <b>K.R. Bindhu, P.M. Sukumar and K.P. Jaya</b>	47
504	<u>29th ISET ANNUAL LECTURE</u> Estimation of Earthquake Ground Motion in Mexico City and Delhi, Two Mega Cities <b>Shri Krishna Singh</b>	65
505	Seismic Retrofit of Columns in Buildings for Flexure Using Concrete Jacket <b>Gnanasekaran Kaliyaperumal and Amlan Kumar Sengupta</b>	77
	<b>Technical Note</b>	
	Two-Dimensional Static Deformation of an Orthotropic Elastic Layered Half-Space due to Blind Strike-Slip Fault <b>Shamta Chugh, Kuldip Singh and Dinesh Kumar Madan</b>	109

**Financial Assistance from DST, New Delhi for the Publication of ISET Journals for 2009–2010 is duly acknowledged.**

## **PERFORMANCE OF EXTERIOR BEAM-COLUMN JOINTS UNDER SEISMIC TYPE LOADING**

K.R. Bindhu\*, P.M. Sukumar\*\* and K.P. Jaya\*\*

\*Department of Civil Engineering

College of Engineering, Thiruvananthapuram-695016

\*\*Structural Engineering Division

Anna University, Chennai-600025

### **ABSTRACT**

The objective of the present study is to compare the behaviour of exterior beam-column joint sub-assemblages with transverse reinforcements detailed as per IS 456 and IS 13920. A six-storeyed RC building in the zone III is analyzed, and one of the exterior beam-column joints at an intermediate storey is designed. The earthquake analysis and design are carried out by incorporating all the modifications as per the latest revisions of IS 1893 and IS 13920. Four one-third scaled specimens, two detailed as per IS 456 and SP 34 and the other two as per IS 13920, were tested under a reverse cyclic loading. The specimens were tested under two different axial loads to evaluate the effect of axial load on the behaviour of joints. The test results indicate that the latest revisions for joint design assure the beam failure to take place before the joint failure. Enhancements in the performance of beam-column joints detailed as per IS 13920 in the reversal of loading were also observed.

**KEYWORDS:** Beam-Column Joint, Confinement, Detailing, Seismic Analysis, Strong-Column Weak-Beam Concept

### **INTRODUCTION**

Severe reverse cyclic loading due to earthquakes causes large inelastic deformations in the beam-column joints of high-rise buildings. If the joints are not designed and detailed properly, their performance can significantly affect the overall response of the moment-resisting frames. Due to the restriction of space available in the joint block, the detailing of joint reinforcement assumes more significance than elsewhere. One of the basic assumptions of the frame analysis is that the joints are strong enough to sustain the forces (i.e., moments, and axial and shear forces) generated by the loading, and to transfer the forces from one structural element to another (i.e., from beams to columns in most of the cases). The analysis with the assumption of joint being rigid fails to consider the effects of high shear forces developed within the joint (Subramanian and Rao, 2003).

Recent earthquakes have demonstrated that even when the beams and columns in a reinforced concrete frame remain intact, the integrity of the whole structure is compromised if the joints, where these members are connected, fail. Beam-column joints are susceptible to failure earlier than the adjacent members due to the destruction of joint zone. This failure is mainly for the external joints. Therefore, ductility and energy absorption capacity of the beam-column joints are of paramount importance in the seismic resistance of structures (Murthy et al., 2000). Further, reinforcing bars have to meet the requirements of strength and ductility under the repeated reversed deformations. Also, while designing the joint core, it is necessary to verify the shear resistance and anchorage conditions of the reinforcement passing through the joint region.

As per the Indian code of practice for plain and reinforced concrete (BIS, 2000), joints are not specially designed, with the attention being restricted to the provision of sufficient anchorage for the beam longitudinal reinforcement. This may be acceptable when the frame is not subjected to earthquake loads. The poor design practice of beam-column joints is compounded by the high demand imposed by the adjoining flexural members (i.e., beams and columns) in the event of mobilization of their inelastic capacities to dissipate the seismic energy. An unsafe design and detailing within the joint region jeopardizes the entire structure, even if other structural members conform to the design requirements.

Experimental results on the performance of beam-column sub-assemblages of modern structures indicate that current design procedures could sometimes lead to excessive damage of the joint regions

(Tsonos, 2007). Several researchers have studied the influence of axial load on the behaviour of joints under cyclic lateral loading. Uzumeri (1974) tested exterior beam-column sub-assemblages under high constant axial compressive forces and concluded that large axial compressive forces applied to the concrete struts are detrimental to the joints. Bonacci and Pantazopoulou (1993) conducted a parametric investigation of interior joint mechanics based on the variables such as axial load, amount of transverse reinforcement, concrete strength, presence of transverse beams, and bond demand on strength. Agbabian et al. (1993) tested three interior beam-column sub-assemblages with 10%, 5%, and 0% axial load capacities. These test results have indicated that the overall displacement response of sub-assemblages decreases by 22% for a decrease in axial load from 10% to 5% of the squash load. From the above studies, it can be seen that the effect of axial load on the behaviour of joints needs to be verified.

IS 13920 (BIS, 1993) covers the requirements of design and ductile detailing of the reinforced concrete structures subjected to seismic forces. In the proposed revision of IS 13920, guidelines on beam-column joints are included (Jain and Murty, 2005b). The basic requirement of design is that the columns above and below a joint should have sufficient flexural strength when the adjoining beams develop flexural overstrengths at their plastic hinges. This column-to-beam flexural strength ratio is an important parameter to ensure that possible hinging occurs in the beams rather than in the columns or in the joint region. A joint should also have adequate shear strength to avoid the shear failure.

The role of transverse reinforcement and mechanism of shear transfer in a joint for seismic resistance are matters of much debate (Hwang et al., 2005). IS 13920 (BIS, 1993) assumes the role of hoops as to confine the joint core. The real function of hoops may be both to confine the joint core and to carry shear as tension in a tie and hence to constrain the width of cracks. The special confining reinforcement serves three purposes. First, it provides shear resistance to the member. Second, it confines the concrete core and thereby increases the ultimate strain of concrete, which gives greater ductility to the concrete cross-section and enables it to undergo large deformations. Last, it provides lateral restraint against buckling to the compression reinforcement. The experimental studies reveal that the usage of rectangular spiral reinforcement significantly improves the seismic capacity of external beam-column connections (Karayannis et al., 2005).

## **SCOPE OF THE STUDY**

The present work aims mainly at carrying out an experimental investigation to compare the behavior of exterior joints with transverse reinforcement detailed as per IS 456 (BIS, 2000), with additional U-bars as per SP 34 (BIS, 1987b), and IS 13920 (BIS, 1993). The amendments proposed for earthquake analysis and design (Jain and Murty, 2005a, 2005b) are incorporated for arriving at the geometry and reinforcement detailing of all test specimens. The detailing of transverse reinforcement at the joint is chosen as the major variable parameter. The effect of axial load on the behavior of joint is also considered in this study.

## **ANALYSIS AND DESIGN OF BEAM-COLUMN JOINT**

A six-storeyed RC building in the zone III and on the medium soil was analyzed, and the shear forces, bending moments, and axial forces around the exterior beam-column joint due to the induced earthquake loading were calculated. The joint marked "A" in Figure 1 was considered for the design. The columns were 3 m long with 450×300 mm cross-section, and beams were with 300×450 mm cross section. A live load of 3 kN/m<sup>2</sup> and floor finish of 1 kN/m<sup>2</sup> was taken for the analysis. The thicknesses of peripheral and internal walls were taken as 250 mm and 150 mm, respectively. The M30 grade concrete and Fe 415 grade steel were used for the design. The plane frames constituting the joint region were analyzed. The design was carried out based on the proposed amendments (Ingle and Jain, 2005) to IS 1893 (BIS, 2002) and IS 13920 (BIS, 1993). The detailing of transverse reinforcement in the beams, column, and exterior joint were done by considering the detailing criteria of IS 456 (BIS, 2000) and including additional U bars as per SP 34 (BIS, 1987b) for one case, and by incorporating the ductile detailing as per IS 13920 for the second case.

Plane frames were analyzed, and force resultants for various load cases such as dead load, live load, and earthquake load were estimated in the beam AB of the short frame. The design moment and shear force from the critical load combinations for the beam AB were 160.05 kN-m and 112.8 kN, respectively.

The longitudinal reinforcement details of transverse beam and longitudinal beams near the exterior joint are shown in Figures 2(a) and 2(b). The spacing of stirrups on the beam AB near joint was calculated as per IS 456 (BIS, 2000) and as per IS 13920 (BIS, 1993). Two-legged stirrups of 8 mm diameter were provided at a spacing of 100 mm centre to centre near the joint and at 150 mm centre to centre near the mid-span.

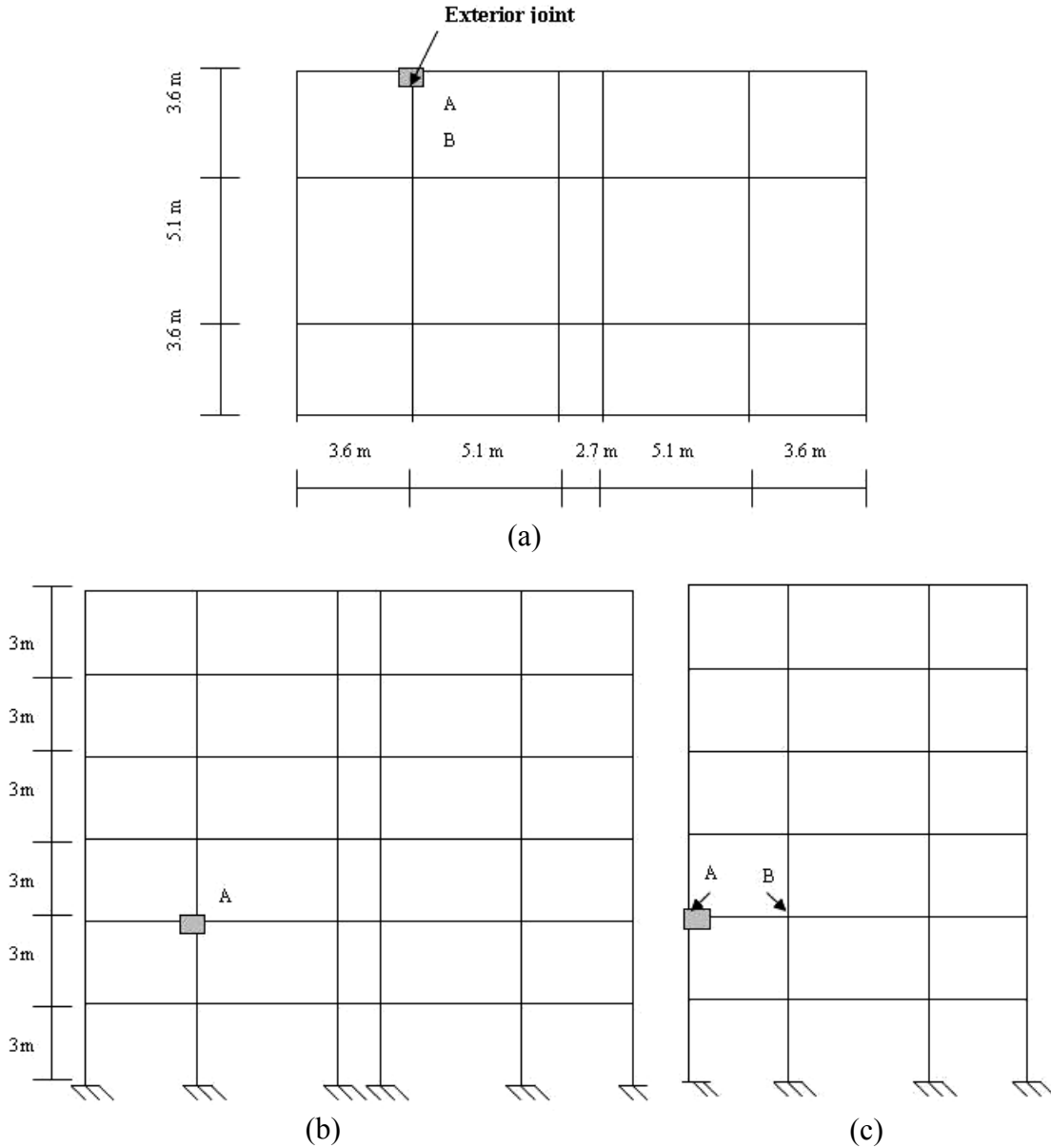


Fig. 1 Details of the building: (a) plan of the building, (b) elevation of the longitudinal frame with the joint A, (c) elevation of the transverse frame with the joints A and B

The exterior column was designed for an axial load of 953 kN and a moment of 86.3 kN-m, which were the critical values obtained from the thirteen different load combinations. Eight 20-mm diameter bars were provided, with the bars distributed equally on all faces of the column. The joint was designed for the strong-column weak-beam condition, for the earthquake ground motion in the X- and Y-directions, as per the draft revision of IS 13920 (BIS, 1993). Special confining reinforcements were provided in the joint region for the detailing as per IS 13920. In the detailing as per the Indian concrete code of practice IS 456 (BIS, 2000), joints were not provided with stirrups, but U-bars were provided for confining the joint core as described by SP 34 (BIS, 1987b).

### 1. Design of Exterior Joint

The joint shear strength and strong-column weak-beam condition for the earthquake ground motion in the X- and Y-directions were checked as per the draft revision of IS 13920 (BIS, 1993) and were found to be satisfactory.

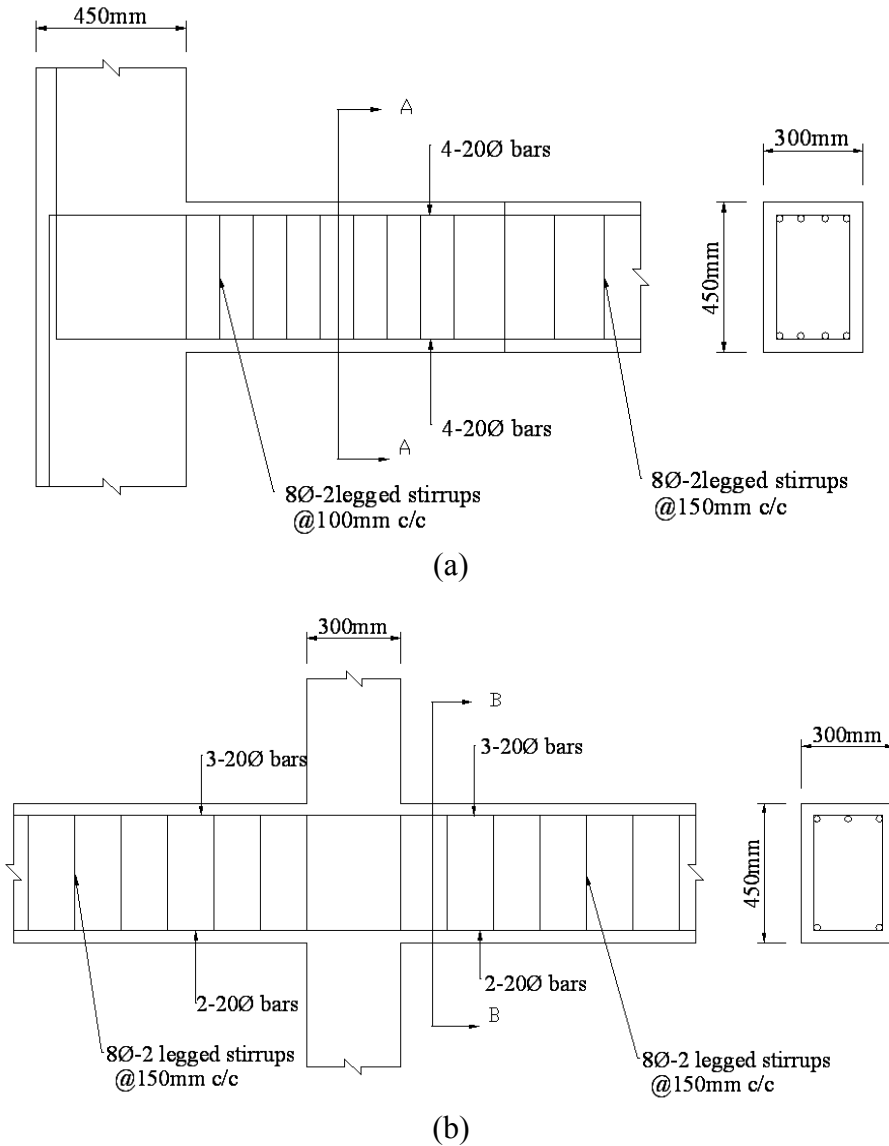


Fig. 2 (a) Reinforcement details of the transverse beam near the joint A; (b) Reinforcement details of the longitudinal beams near the joint A

Since equal reinforcements were provided at the top and bottom of the transverse beam,  $V_{col}$ , the column shear for sway to right or to left during the earthquake loading in the Y-direction, was obtained as 74.50 kN. The force  $T_1$  developed in the top reinforcement of beam was 651.55 kN. Thus, the joint shear force  $V_{joint}$  is obtained from Equation (1) as 577.04 kN:

$$V_{joint} = T_1 - V_{col} \quad (1)$$

For the earthquake loading in the X-direction, the column shear for sway to right or to left,  $V_{col}$  was obtained as 98.50 kN. The force  $T_1$  developed in the top reinforcement of the right longitudinal beam was 488.66 kN. The force  $T_2$  developed in the bottom reinforcement of the left longitudinal beam was 325.78 kN. Thus, the joint shear force  $V_{joint}$  is obtained from Equation (2) as 715.94 kN:

$$V_{\text{joint}} = T_1 + C_2 - V_{\text{col}} \tag{2}$$

where  $C_2$  is the compressive force in the left beam, which is equal to the tensile force  $T_2$  developed in the left beam. The effective width  $b_j$  of the joint as per the draft revision of IS 13920 (BIS, 1993) is lesser of (i)  $b_j = b_b + 0.5h_c$  and (ii)  $b_j = b_c$ , where  $b_b$  denotes the width of the beam,  $h_c$  the depth of the column in the considered direction of shear, and  $b_c$  the width of the column.

The effective shear area  $A_{ej}$  of the joint is equal to  $b_j h_j$ , where  $h_j$  is the depth of the joint which can be taken as the depth of the column. The shear strength of the joint,  $A_{ej} \sqrt{f_{ck}}$ , was obtained as 739.43 kN, which is higher than the joint shear force for the earthquake loading in the Y-direction and in the X-direction. Hence, the joint has adequate shear strength in both directions as per the proposed revision. The column-to-beam flexural strength ratios for the earthquake loading in the Y-direction and in the X-direction of the exterior-joint prototype were obtained as 1.84 and 1.39, respectively. Hence, the requirement of strong-column weak-beam condition was satisfied for the earthquake loading in both Y- and X-directions.

Thus, all the joint sub-assemblages considered for the experimental study were checked for shear strength and the strong-column weak-beam theory. The only difference was in the arrangements of transverse reinforcement. Special confining reinforcement was continued in the joint region with detailing as per IS 13920 (BIS, 1993). In the Indian concrete code of practice, IS 456 (BIS, 2000), joints are not provided with stirrups, but U-bars are provided for confining the joint core as in SP 34 (BIS, 1987b).

**EXPERIMENTAL PROGRAM**

The prototype of the exterior beam-column joint was scaled down to its one-third size. The dimensions and reinforcement details of the test assemblages are shown in Figures 3 and 4 and in Table 1. The specimens were classified into two groups, with two specimens in each group. The specimens in Group 1 were cast with reinforcement detailed as per IS 456 (BIS, 2000). The specimens in Group 2 were detailed as per IS 13920 (BIS, 1993). All the four specimens were tested under constant axial load with cyclic load at the end of the beam. One of the specimens from each group was subjected to an axial load of 3% column axial load capacity and the other specimen was subjected to an axial load of 10% column axial load capacity. The value of axial load on the second specimen was arrived at from the axial force on the upper column of the assemblage at the critical load combination selected for design.

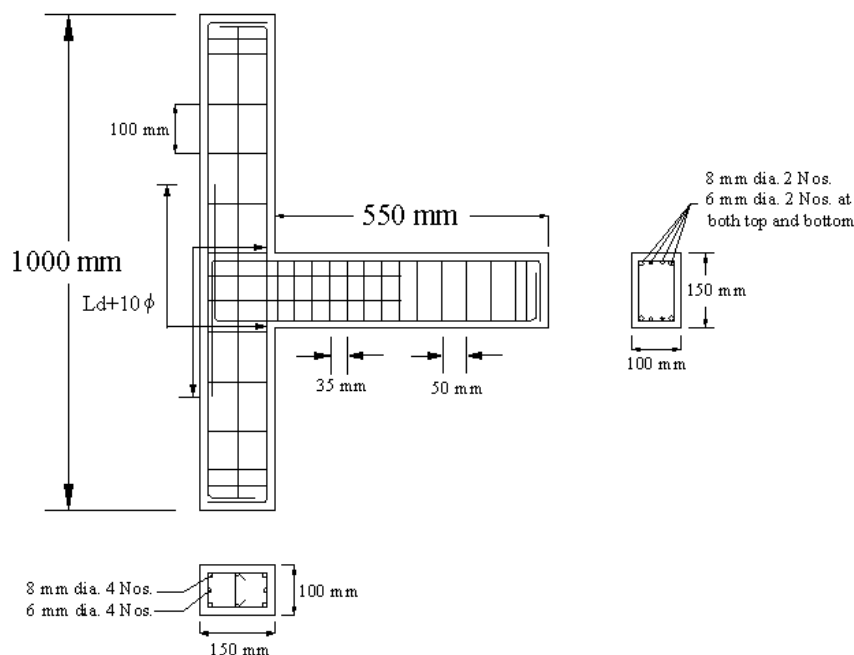


Fig. 3 Reinforcement details of the beam-column joint specimen as per IS 456 (BIS, 2000)

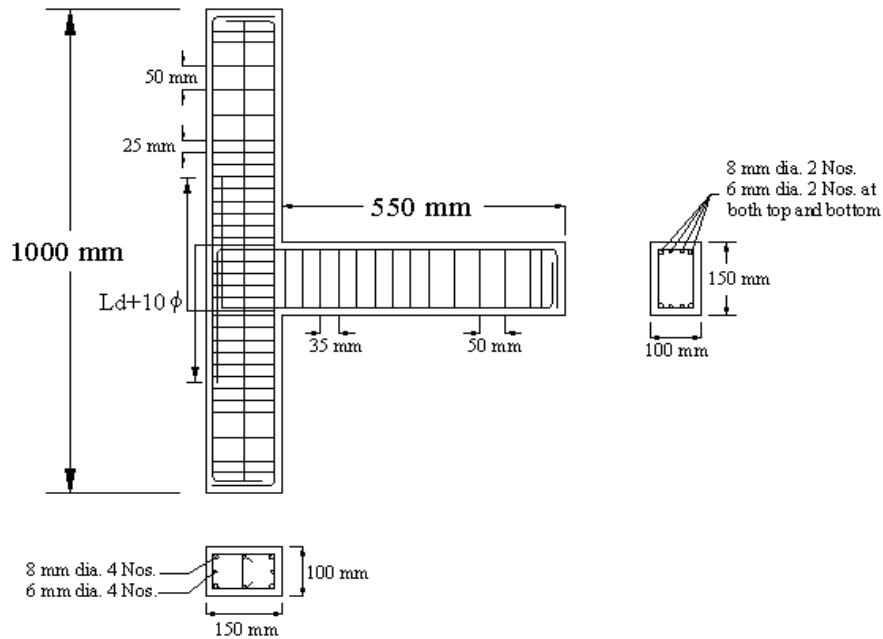


Fig. 4 Reinforcement details of the beam-column joint specimen as per IS 13920 (BIS, 1993)

Table 1: Reinforcement Details of Test Specimens

Specimen Designation	Column Reinforcement		Beam Reinforcement		Joint Reinforcement	Remarks
	Longitudinal	Transverse	Longitudinal	Transverse	Transverse	
A1-456 and A2-456	Four 8-mm diameter and four 6-mm diameter	3-mm diameter at 100 mm centre to centre	Two 8-mm diameter and two 6-mm diameter (at the top and bottom)	3-mm diameter at 35 mm centre to centre for a distance of 270 mm from the joint and 50 mm center to center for the remaining length	Two 3-mm diameter U bars, with development length in tension extended to the beam	No stirrups at the joint, but additional U bars (with hairclip type bend) used for the confinement as per SP 34 (BIS, 1987b)
A1-13920 and A2-13920	Four 8-mm diameter and four 6-mm diameter	3-mm diameter at 25 mm centre to centre for a distance of 230 mm at either side of the joint and 50 mm centre to centre for the remaining portion	Two 8-mm diameter and two 6-mm diameter (at the top and bottom)	3-mm diameter at 35 mm centre to centre for a distance of 270 mm from the joint and 50 mm center to center for the remaining length	3-mm diameter at 25 mm center to centre	Confining reinforcement at the joint as per IS 13920 (BIS, 1993)

## 1. Casting of Specimens

The specimens were cast by using the 53 grade ordinary Portland cement conforming to IS 12269 (BIS, 1987a). Medium river sand passing through 4.75 mm IS sieve and having a fineness modulus of 2.77 was used as the fine aggregate. Crushed granite stone of maximum size not exceeding 8 mm and having a fineness modulus of 3.58 was used as the coarse aggregate. The mix proportion was 1:0.87:1.32 by weight and the water-cement ratio was kept as 0.48. The 28-day average compressive strength from the 150-mm cube test was 44.22 N/mm<sup>2</sup>. The yield stress of reinforcement was 432 N/mm<sup>2</sup>. All the specimens were cast in the horizontal position inside a steel mould on the same day. Those were demoulded after 24 hours and were then cured under the wet gunny bags for 28 days.

## 2. Experimental Setup

The joint assemblages were subjected to the axial load and reverse cyclic loading. The specimens were tested in an upright position and the reverse cyclic loading was applied statically at the end of the beam. One end of the column was given an external hinge support that was fastened to the strong reaction floor, and the other end was laterally restrained by a roller support. A schematic drawing of the setup is shown in Figure 5. The experimental setup at the laboratory is shown in Figure 6.

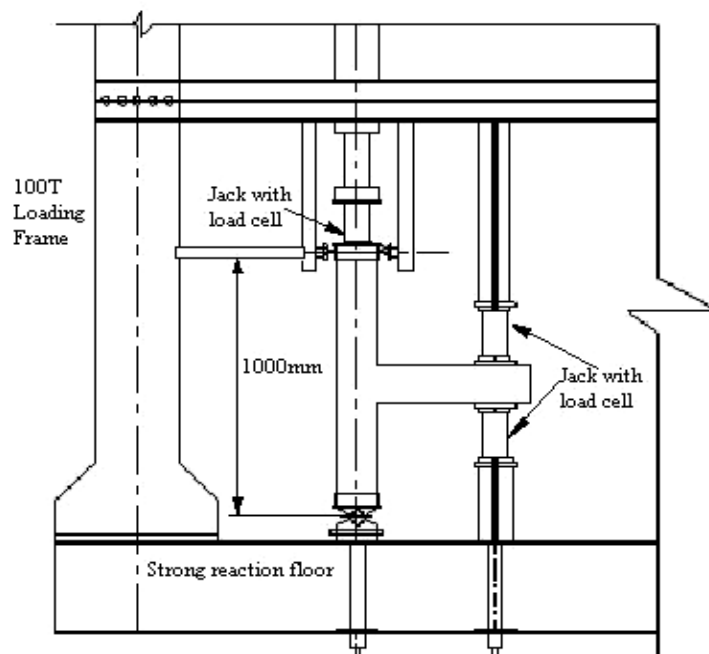


Fig. 5 Schematic diagram of the test set-up

Past theoretical and experimental studies on the influence of the simultaneous changing of the axial load in the column and lateral displacement in the external beam-column joints indicate that significant deterioration is caused in the joint shear strength by the axial load change and P- $\Delta$  effect (Tsonos, 2004). It is not the objective of this study to investigate the effect of varying axial load on the response of the sub-assemblages. The influence of the column axial load on the shear capacity of the joints is considered favorable, since the developed principal stresses in the joint are reduced due to the application of compressive axial load, whereas those reach maximum values when the column axial load is null or is neglected (Chalioris et al., 2008). In the present study, the application of the axial load was controlled in order to maintain a constant value during the entire testing procedure.

A constant column axial load was applied by means of a 392.4 kN (40 t) hydraulic jack mounted vertically to the 981 kN (100 t) loading frame to simulate the gravity load on the column. The axial load was 15.92 kN (1.62 t) for the first-series specimens and 53.06 kN (5.41 t) for the second-series specimens. The cyclic loading was applied by two 196.2 kN (20 t) hydraulic jacks, one fixed to the loading frame at the top and another to the strong reaction floor. The reverse cyclic load was applied at 50 mm from the free end of the beam portion of the assemblage. The test was load-controlled and the specimen was subjected to an increasing cyclic load up to its failure.

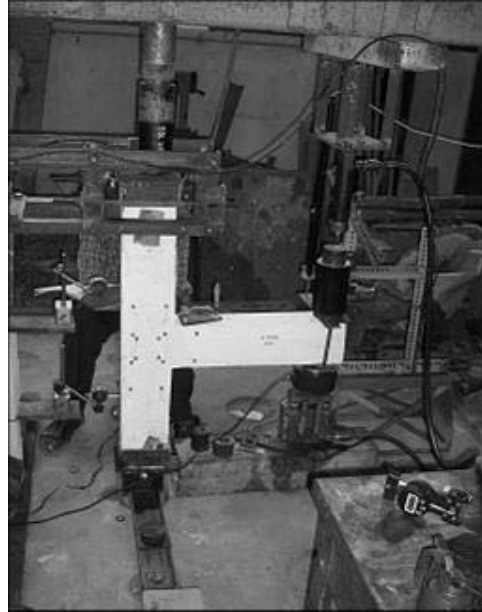


Fig. 6 Test setup in the laboratory

In order to utilize the results obtained from a quasi-static cyclic loading test on structural elements for a general performance evaluation there is a need to establish a loading history that captures the critical issues of the element capacity as well as of the seismic demands. The basic seismic capacity parameters for a structural element are strength, stiffness, inelastic deformation capacity (i.e., ductility), and cumulative damage capacity parameters such as energy dissipation capacity. All these parameters are expected to deteriorate as the number of damaging cycles and the amplitude of cycles increase (Karayannis and Sirkelis, 2008; Chalioris et al., 2008). In order to draw conclusions for the ultimate limit state and to evaluate the performance under arbitrary seismic excitations, a cyclic loading sequence with constantly increasing load and large inelastic excursions was chosen. It may also be emphasised that there is a significant dependence of the demand parameters on the natural period of the structure, of which the structural element is a member. For generic test specimens, there exists a need to obtain these parameters for short-period structures, with the understanding that their values may be very conservative for the long-period structures.

The load increment chosen was 1.962 kN (200 kg). The loading protocol consists only of one cycle, and repeat cycles were not employed. The specimen was first loaded up to 1.962 kN and unloaded and was then reloaded in the reverse direction up to 1.962 kN. The subsequent cycles were also loaded in a similar way. Figure 7 shows the loading sequence of the test assemblages. To record the loads precisely, load cells with the least count of 0.0981 kN were used. The specimens were instrumented with a linear variable differential transformer (LVDT) with the least count of 0.1 mm to measure the deflection at the loading point. A clinometer was fixed on top of the beam element of the specimen to measure rotation near the interface during the loading.

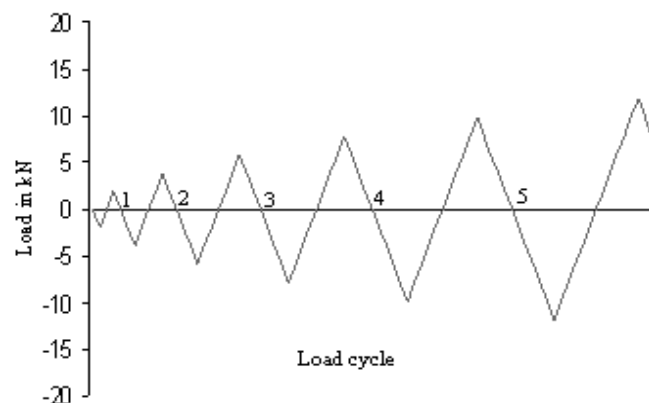


Fig. 7 Sequence of cyclic loading

**DISCUSSION OF TEST RESULTS**

The test results are presented in the form of load-deformation hysteretic curves, envelope curves for load-displacement, energy dissipation curves, stiffness degradation curves, and damage-index and moment-rotation envelopes. The observations made during the test are briefly described in the following sections.

**1. Cracking Pattern and Failure Mode**

In all specimens in the first series (with the axial load of 15.92 kN) the initial diagonal hairline crack on the joint occurred at the second loading cycle, when the load reached 3.924 kN in both positive and negative cycles of loading. However, for the second series (with the axial load of 53.06 kN), the first crack appeared only in the third cycle for a load of 5.886 kN in all specimens. The yield and ultimate loads for the test specimens are shown in Table 2. The specimens in the two series performed in the same manner for their ultimate strengths. However, the axial load improved the cyclic load carrying capacity of the joint. The cracking patterns of the test specimens in the first and second series are shown in Figures 8 and 9, respectively. In almost all specimens, tensile cracks were formed at the interface between the column and beam. The specimens failed due to the advancement of crack width at the interface between the beam and the column. There was a clear vertical cleavage formed at the junction of all specimens. In addition to that, for the first-series specimens, there were some hairline cracks in the joint region. The second-series specimens were tested under the increased axial load, and it may be observed that the performance improved due to the increase in axial load.

**Table 2: Experimental Yield and Ultimate Loads of Specimens**

Designation of Specimen	Experimental Yield Load (kN)			Experimental Ultimate Load (kN)		
	Downward Direction	Upward Direction	Average ( $P_{ye}$ )	Downward Direction	Upward Direction	Average ( $P_{ue}$ )
A1-456	13.73	11.77	12.75	15.69	14.71	15.2
A1-13920	11.77	11.77	11.77	16.18	15.69	15.93
A2-456	15.7	13.7	14.7	18.64	18.64	18.64
A2-13920	15.7	15.7	15.7	17.66	19.62	18.64

Similar to the first series, the specimens in the second series failed due to the vertical cleavage at the beam-column joint interface. Thus, with beam failure having preceded the joint failure, it can be seen that all the specimens have satisfied the strong-column weak-beam theory.



(a)



(b)

Fig. 8 Crack patterns in the specimens in the first series for (a) Specimen A1-456 and (b) Specimen A1-13920

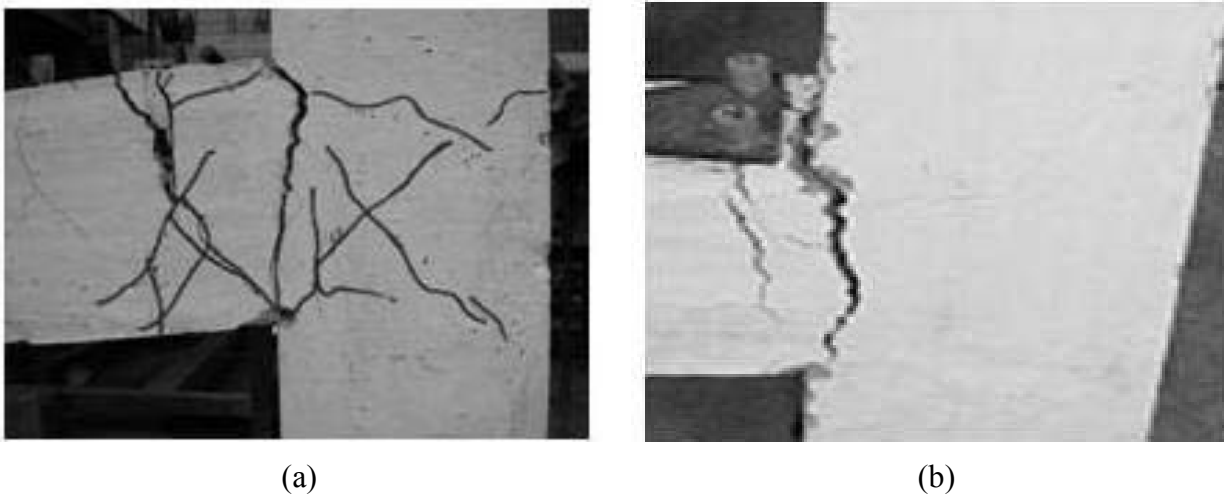


Fig. 9 Crack patterns in the specimens in the second series for (a) Specimen A2-456 and (b) Specimen A2-13920

## 2. Hysteretic Loops

The force-displacement hysteretic loops for the specimens are shown in Figures 10 to 13. It is seen from Table 2 that the ultimate load carrying capacity is increased with an increase in axial load. A relative comparison of the overall force-deformation behavior of all specimens in the first and second series is shown in Figure 14.

## 3. Energy Dissipation

The area enclosed by the hysteretic loop in a given cycle represents the energy dissipated by the specimen during that cycle. Figure 15 shows the cumulative energy dissipated versus cumulative displacement curve of all specimens. The highest energy dissipated (i.e., 995.5436 kN-mm) was for Specimen A1-13920. It may be observed that an increase in the axial load reduces the energy dissipation capacity of specimens. However, the specimens with higher axial loads are found to have sustained greater number of cycles of the seismic type loads than the specimens with lesser axial loads.

## 4. Member Flexural Strength

The section capacities are designed to have the ratio  $\sum M_c / \sum M_b$  of 2.3 for all specimens to ensure that the beams fail before the column. The design and experimental member flexural capacities of the specimens are shown in Table 3. The experimental values of the member capacities show that the specimens have satisfied the strong-column weak-beam concept.

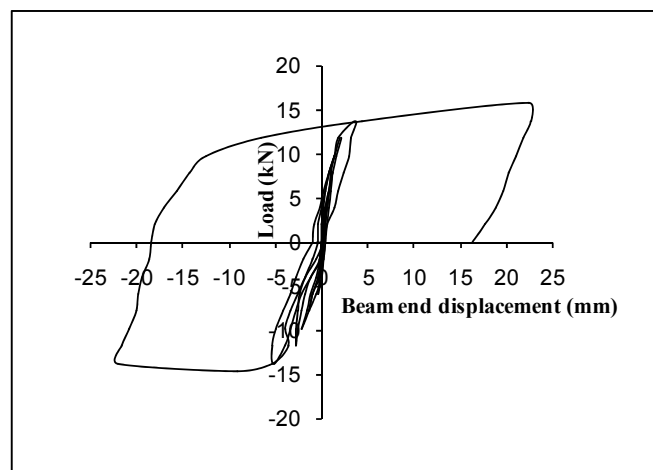


Fig. 10 Load versus displacement curve of Specimen A1-456

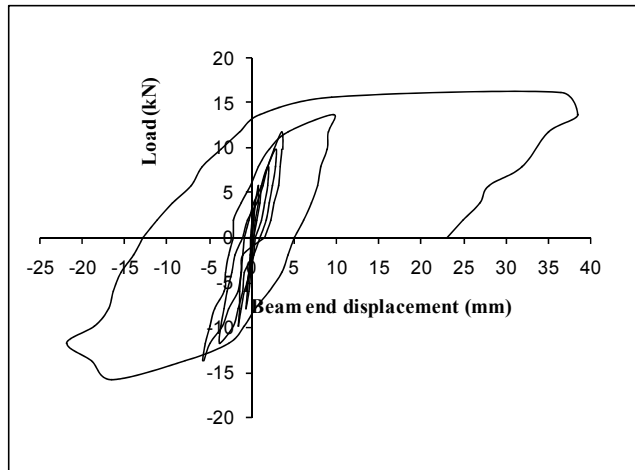


Fig. 11 Load versus displacement curve of Specimen A1-13920

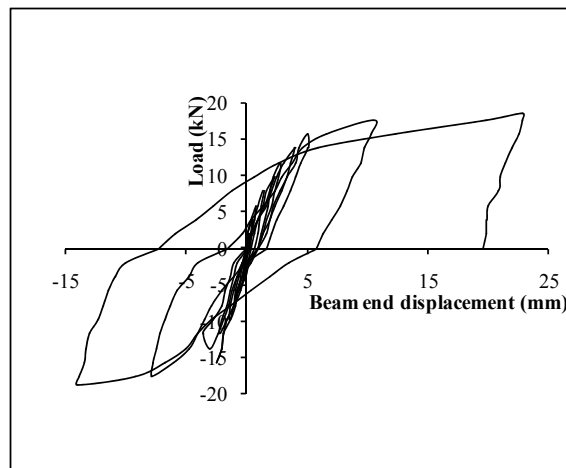


Fig. 12 Load versus displacement curve of Specimen A2-456

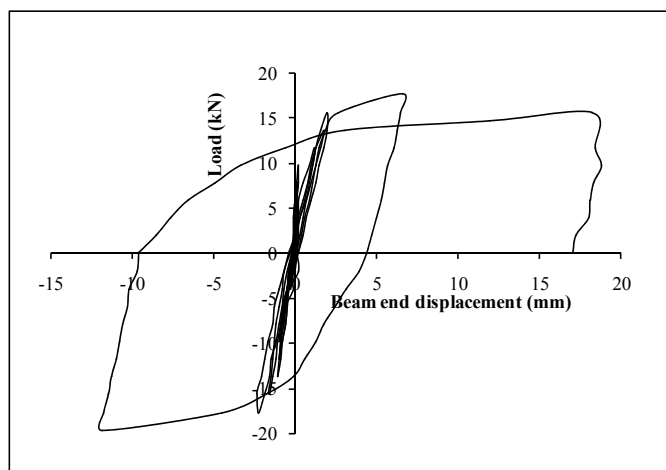


Fig. 13 Load versus displacement curve of Specimen A2-13920

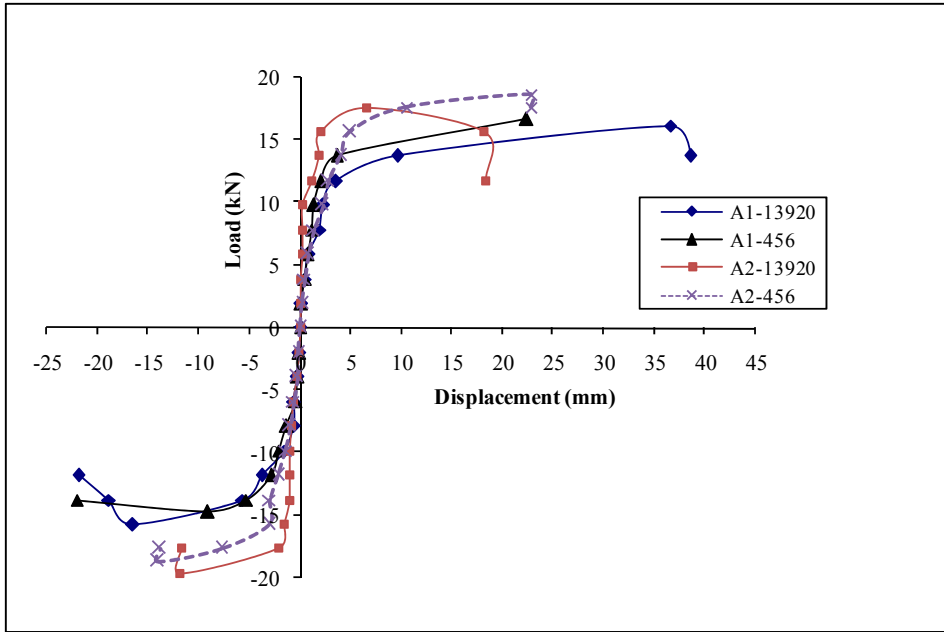


Fig. 14 Load-displacement envelopes of the four specimens

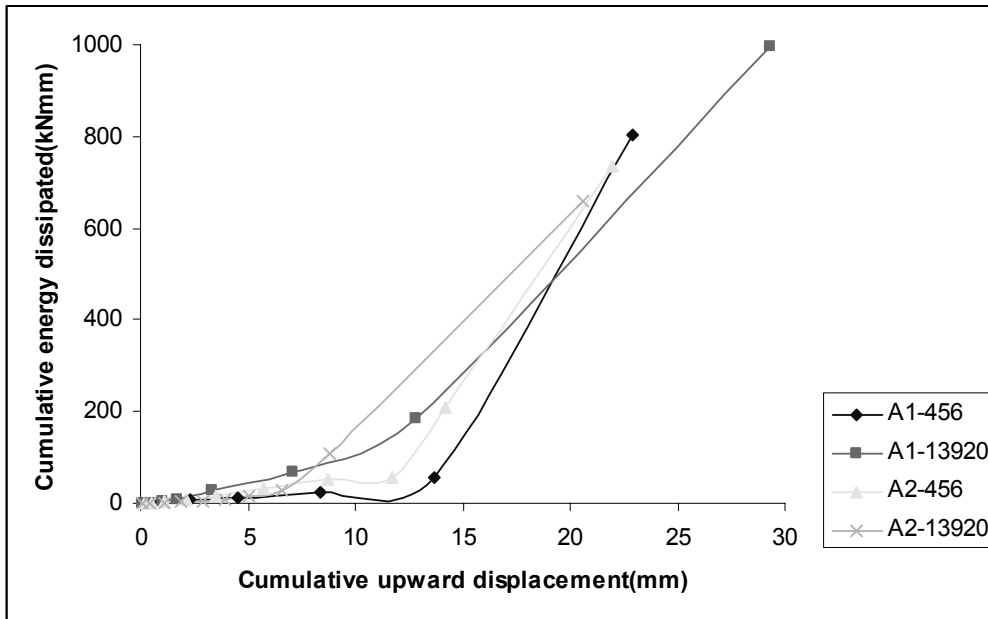


Fig. 15 Cumulative energy dissipation curves of the four specimens

Table 3: Member Flexural Strengths of Test Specimens

Designation of Specimen	Beam Moment Strength (kN-m)			Column Moment Strength (kN-m)			$\frac{\sum M_c}{\sum M_b}$	
	Design	Experimental		Design	Experimental			
		Yield Strength	Over-strength		Yield Strength	Over-strength	Yield Strength	Over-strength
A1-456	5.91	6.865	7.36	5.47	7.90	8.46	2.3	2.3
A1-13920	5.91	6.865	7.85	5.47	7.90	9.02	2.3	2.3
A2-456	5.91	7.85	9.32	5.47	9.03	10.72	2.3	2.3
A2-13920	5.91	7.85	9.81	5.47	9.03	11.28	2.3	2.3

### 5. Joint Stresses

The horizontal shear stress in the exterior joint sub-assembly can be expressed as (Murty et al., 2003)

$$\tau_{jh} = \frac{P}{A_{core}^h} \left( \frac{L_b}{d_b} - \frac{L_b + 0.5D_c}{L_c} \right) \tag{3}$$

where  $P$  denotes the imposed cyclic load at the end of the beam,  $L_b$  the length of the beam,  $L_c$  the length of the column,  $D_c$  the total depth of the beam,  $d_b$  the effective depth of the beam, and  $A_{core}^h$  the horizontal cross-sectional area of the joint core resisting the horizontal shear force.

It is necessary to limit the magnitude of the horizontal joint shear stress to protect the joint against diagonal crushing. The ACI-318 standard (ACI, 2002) limits the horizontal joint shear stress (in MPa) as  $k\sqrt{f'_c}$ , where  $f'_c$  is the cylinder compressive strength in MPa. The factor  $k$  depends on the confinement provided by the members framing into the joint;  $k$  is taken as 1.67, 1.25, and 1.0 for the interior, exterior, and corner joints, respectively.

The ultimate values of the horizontal shear stress induced in the joints are found to be almost equal to or little higher than the ACI-recommended values (ACI, 2002). It may be seen from Table 4 that the shear-resisting capacity is more for the specimens detailed according to IS 13920 (BIS, 1993) than for the specimens detailed according to IS 456 (BIS, 2000) and provided with additional U-bars. Further, an increase in the axial load improves the shear capacity of joints. From the values of  $\tau_{jh}/\tau_{ACI}$ , it may be seen that the specimens with higher axial loads exhibit higher shear capacity. Even at lower axial load levels, the specimens have shear capacity close to the ACI-prescribed limiting value (ACI, 2002). Hence, the design of longitudinal reinforcement and geometry of the section as per the proposed revisions (Jain and Murty, 2005a, 2005b) appear to be adequate.

**Table 4: Comparison of Ultimate Joint Shear Stress with the ACI Code-Prescribed Limiting Values**

Designation of Specimen	$H_u$ (kN)	$H_{u,calc}$ (kN)	$\frac{H_u}{H_{u,calc}}$	$\tau_{jh}$ (MPa)	$\frac{\tau_{jh}}{\tau_{ACI}}$
A1-456	14.71	14.1	1.04	5.48	0.92
A1-13920	15.69	14.1	1.11	5.84	0.98
A2-456	18.64	14.1	1.32	6.94	1.16
A2-13920	19.62	14.1	1.39	7.31	1.23

With  $f'_c = 35.376$  MPa, the maximum permissible shear stress  $\tau_{ACI}$  is equal to 5.95 MPa.

The principal tensile stress (i.e., diagonal tensile stress) developed in the beam-column joint region is calculated as

$$\sigma_t = \frac{\sigma_p}{2} + \sqrt{\frac{\sigma_p^2}{4} + \tau_{jh}^2} \tag{4}$$

where  $\sigma_p = (N_c + P)/b_c h_c$  is the axial compressive stress in the joint area;  $\tau_{jh}$  is the joint horizontal shear stress;  $N_c$  is the axial compressive load in the column; and  $P$  is the imposed cyclic load at the end of the beam.

On computation of  $\tau_{jh}$  using Equation (3), Figure 16 shows the variation of principal stress in the joint with storey drift. From the figure it is deduced that the principal stress developed in the specimens detailed as per IS 13920 (BIS, 1993), i.e., A1-13920 and A2-13920, is higher than that for the corresponding specimens detailed as per IS 456 (BIS, 2000), i.e., A1-456 and A2-456.

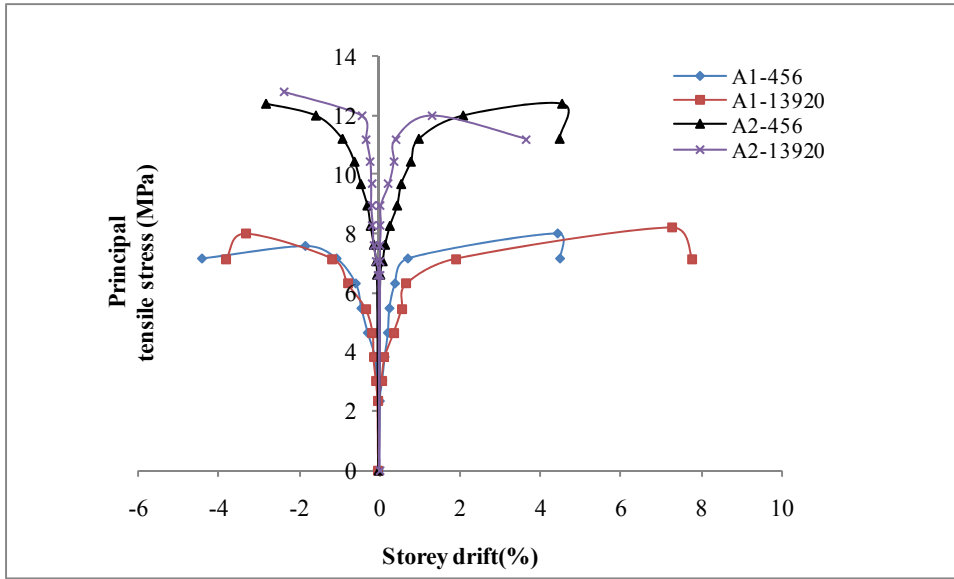


Fig. 16 Principal tensile stresses of the tested specimens

## 6. Damage Index

To assess the effectiveness of joints, the damage index model by Park and Ang (1985) is employed in this study. This model is based on the concept that seismic structural damage can be expressed as a linear combination of the damage caused by excessive deformation and the damage accumulated due to the repeated cyclic loading effect (Sreekala et al., 2007). In terms of damage index this model may be described as

$$D = \frac{\delta_M}{\delta_u} + \frac{\beta}{Q_y \delta_u} \int dE \quad (5)$$

where  $\delta_M$  is the maximum deformation under the earthquake ground motion;  $\delta_u$  is the ultimate deformation under the monotonic loading;  $Q_y$  is the calculated yield strength;  $dE$  is the incremental absorbed hysteretic energy; and  $\beta$  is a non-negative parameter representing the effect of cyclic loading on structural damage. Value of the parameter  $\beta$  is determined in such a way that it represents the nature of damage in the examined specimen as closely as possible.

The confinement ratios for Specimens A1-456 and A2-456 are calculated by considering the additional U-bars in the joint region. The values of damage index by Park and Ang (1985) are presented in Figure 17. From the results it is evident that Specimens A1-13920 and A2-13920 have undergone a lower damage than Specimens A1-456 and A2-456, respectively.

## 7. Stiffness

The stiffness of the beam-column joint is approximated as slope of the peak-to-peak line in each loading cycle (Park and Paulay, 1975; Tsonos, 2000; El-Amoury and Ghojarah, 2002). The variation of stiffness in each cycle corresponding to the maximum displacement in that cycle is calculated and is shown in Figure 18. It may be observed that the stiffness was highest for Specimen A2-13920, and for this specimen, the major reduction in stiffness occurred only after the sixth cycle of loading. Specimen A1-13920 had greater stiffness than Specimens A1-456 and A2-456. This specimen also reached a higher ductility level than the other specimens. While considering the influence of axial load, it may be seen from Figure 18 that the presence of axial load stiffened the joint.

## 8. Moment-Rotation Relation

The envelope curve for the moment in beam near the interface of the sub-assembly and the rotation of the beam element during the downward loading in each cycle are shown in Figure 19. It may be

observed that the rotation was higher for the first-series specimens than for the second-series specimens. Further, Specimens A1-13920 and A2-13920 have exhibited good rotational ductility.

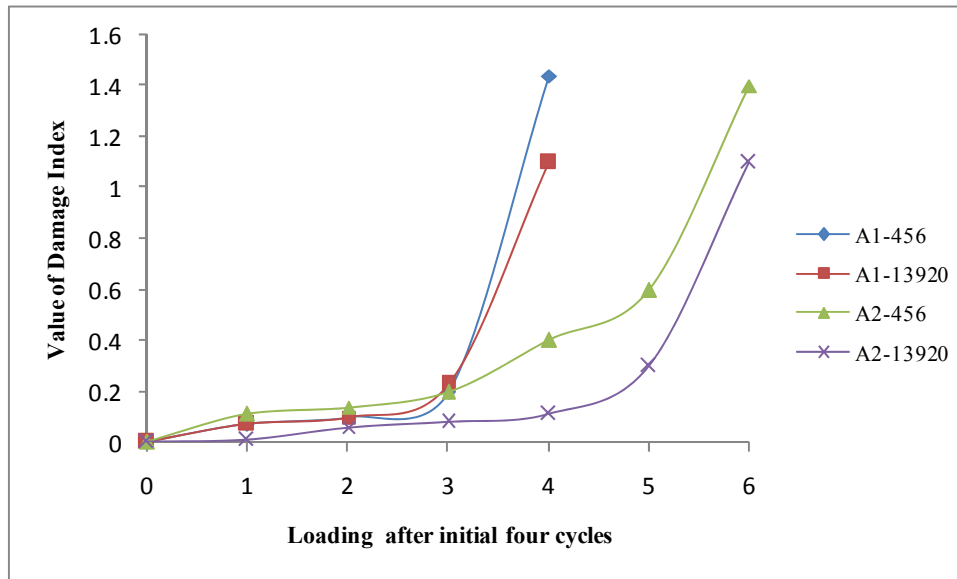


Fig. 17 Comparison of the Park and Ang damage indices of the tested specimens

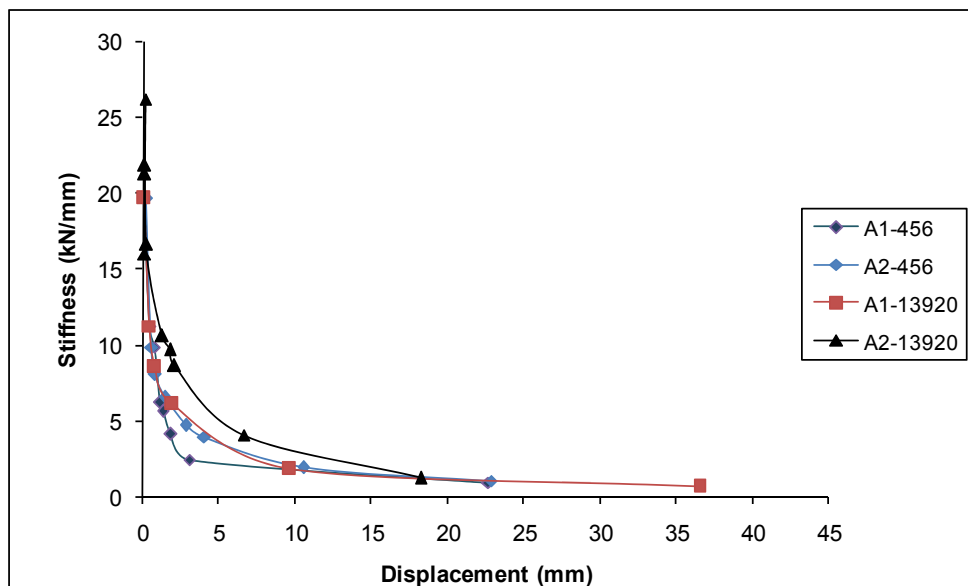


Fig. 18 Stiffness degradation of the specimens

## CONCLUSIONS

The purpose of this investigation was to evaluate the performance of the exterior beam-column joints designed and detailed as per the proposed amendments of IS 1893 (BIS, 2000) and IS 13920 (BIS, 1993) for the earthquake-resistant design. All the specimens were designed for adequate shear strength in the joint and to satisfy the strong-column weak-beam theory. One set of specimens was made with the special confining reinforcement as per the provisions of IS 13920. The effect of special confining reinforcement on the behaviour of joint has been studied by comparing the test results of the companion specimens detailed without the special confining reinforcement but with the transverse reinforcement as required by IS 456 (BIS, 2000) and SP 34 (BIS, 1987b). Following conclusions have been drawn from this study:

1. All the specimens failed due to the development of tensile cracks at the interface between beam and column, and this has ensured that the strong-column weak-beam conditions were satisfied.

2. The joint region was free from cracks except for some hairline cracks, and therefore the joints had adequate shear-resisting capacity.
3. An increase in the column axial load improves the load carrying capacity and stiffens the joints. However, this reduces the energy absorption capacity and ductility of the joint.
4. The specimens having special confining reinforcement as per IS 13920 (BIS, 1993) had an improved energy absorption capacity than the specimens with lateral reinforcement detailing as per IS 456 (BIS, 2000) and SP 34 (BIS, 1987b).

In the present study, for all the specimens the cracks were concentrated at the beam-column interface and not in the beam region. Hence, there is a necessity to develop a detailing pattern of the sub-assemblages in order to shift the plastic hinge towards the beam region.

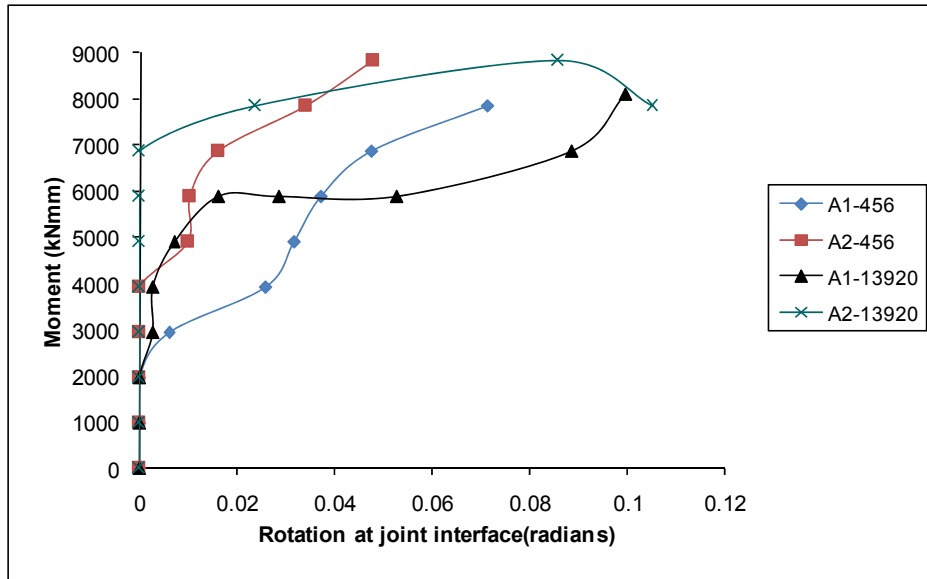


Fig. 19 Moment-rotation relation of the beam element of specimens

## NOTATIONS

- $A_{\text{core}}^h$  = horizontal cross-sectional area of the joint core resisting horizontal shear force
- $A_{ej}$  = effective shear area of joint
- $b_b$  = width of beam
- $b_c$  = width of column
- $b_j$  = effective width of joint
- $C_2$  = compressive force in the left beam
- $d_b$  = effective depth of beam
- $D_c$  = total depth of beam
- $f'_c$  = cylinder compressive strength of concrete
- $h_c$  = depth of column in the considered direction of shear
- $h_j$  = depth of joint which can be taken as depth of column
- $k$  = factor which depends on confinement provided by the members framing into joint
- $L_b$  = length of beam

$L_c$	=	length of column
$N_c$	=	column axial compressive load
$P$	=	imposed cyclic load at the end of beam
$Q_y$	=	calculated yield strength
$T_1$	=	force developed in the top reinforcement of beam
$T_2$	=	force developed in the bottom reinforcement of beam
$V_{\text{joint}}$	=	joint shear force
$V_{\text{col}}$	=	column shear for sway to right or left during the earthquake loading in Y- or X-direction
$\beta$	=	non-negative parameter representing the effect of cyclic loading on structural damage
$\sigma_p$	=	axial compressive stress in the joint area
$\tau_{jh}$	=	joint horizontal shear stress
$\delta_M$	=	maximum deformation under earthquake ground motion
$\delta_u$	=	ultimate deformation under monotonic loading
$dE$	=	incremental absorbed hysteretic energy

## REFERENCES

1. ACI (2002). "Building Code Requirements for Structural Concrete (ACI 318-02) and Commentary (ACI 318R-02)", ACI Standard, American Concrete Institute, Farmington Hills, U.S.A.
2. Agbabian, M.S., Higazy, E.M., Abdel-Ghaffar, A.M. and Elnashai, A.S. (1994). "Experimental Observations on the Seismic Shear Performance of RC Beam-to-Column Connections Subjected to Varying Axial Column Force", *Earthquake Engineering & Structural Dynamics*, Vol. 23, No. 8, pp. 859–876.
3. BIS (1987a). "IS 12269: 1987—Indian Standard Specification for 53 Grade Ordinary Portland Cement", Bureau of Indian Standards, New Delhi.
4. BIS (1987b). "SP 34: 1987—Handbook on Concrete Reinforcement and Detailing", Bureau of Indian Standards, New Delhi.
5. BIS (1993). "IS 13920: 1993—Indian Standard Ductile Detailing of Reinforced Concrete Structures Subjected to Seismic Forces—Code of Practice", Bureau of Indian Standards, New Delhi.
6. BIS (2000). "IS 456: 2000—Indian Standard Plain and Reinforced Concrete—Code of Practice (Fourth Revision)", Bureau of Indian Standards, New Delhi.
7. BIS (2002). "IS 1893 (Part 1): 2002—Indian Standard Criteria for Earthquake Resistant Design of Structures, Part 1: General Provisions and Buildings (Fifth Revision)", Bureau of Indian Standards, New Delhi.
8. Bonacci, J. and Pantazopoulou, S. (1993). "Parametric Investigation of Joint Mechanics", *ACI Structural Journal*, Vol. 90, No. 1, pp. 61–71.
9. Chalioris, C.E., Favvata, M.J. and Karayannis, C.G. (2008). "Reinforced Concrete Beam-Column Joints with Crossed Inclined Bars under Cyclic Deformations", *Earthquake Engineering & Structural Dynamics*, Vol. 37, No. 6, pp. 881–897.
10. El-Amoury, T. and Ghobarah, A. (2002). "Seismic Rehabilitation of Beam-Column Joint Using GFRP Sheets", *Engineering Structures*, Vol. 24, No. 11, pp. 1397–1407.
11. Hwang, S.-J., Lee, H.-J., Liao, T.-F., Wang, K.-C. and Tsai, H.-H. (2005). "Role of Hoops on Shear Strength of Reinforced Concrete Beam-Column Joints", *ACI Structural Journal*, Vol. 102, No. 3, pp. 445–453.

12. Ingle, R.K. and Jain, S.K. (2005). “Explanatory Examples for Ductile Detailing of RC Buildings”, Report IITK-GSDMA-EQ22-V3.0, IIT Kanpur, Kanpur.
13. Jain, S.K. and Murty, C.V.R. (2005a). “Proposed Draft Provisions and Commentary on Indian Seismic Code IS 1893 (Part 1)”, Report IITK-GSDMA-EQ05-V4.0/IITK-GSDMA-EQ15-V3.0, IIT Kanpur, Kanpur.
14. Jain, S.K. and Murty, C.V.R. (2005b). “Proposed Draft Provisions and Commentary on Ductile Detailing of RC Structures Subjected to Seismic Forces”, Report IITK-GSDMA-EQ11-V4.0/IITK-GSDMA-EQ16-V3.0, IIT Kanpur, Kanpur.
15. Karayannis, C.G. and Sirkelis, G.M. (2008). “Strengthening and Rehabilitation of RC Beam-Column Joints Using Carbon-FRP Jacketing and Epoxy Resin Injection”, *Earthquake Engineering & Structural Dynamics*, Vol. 37, No. 5, pp. 769–790.
16. Karayannis, C., Sirkelis, G. and Mavroeidis, P. (2005). “Improvement of Seismic Capacity of External Beam-Column Joints Using Rectangular Spiral Shear Reinforcement”, *Proceedings of the Fifth World Conference on Earthquake Resistant Engineering Structures (ERES V)*, Skiathos, Greece, pp. 147–156.
17. Murthy, D.S.R., Gandhi, P., Sreedhar, D.S., Vaidhyathan, C.V. and Mohanty, O.N. (2000). “Seismic Resistance of Reinforced Concrete Beam-Column Joints with TMT and CRS Bars”, *ICI Journal*, Vol. 1, No. 3, pp. 19–26.
18. Murty, C.V.R., Rai, D.C., Bajpai, K.K. and Jain, S.K. (2003). “Effectiveness of Reinforcement Details in Exterior Reinforced Concrete Beam-Column Joints for Earthquake Resistance”, *ACI Structural Journal*, Vol. 100, No. 2, pp. 149–156.
19. Park, R. and Ang, A.H.S. (1985). “Mechanistic Seismic Damage Model for Reinforced Concrete”, *Journal of Structural Engineering*, ASCE, Vol. 111, No. 4, pp. 722–739.
20. Park, R. and Paulay, T. (1975). “Reinforced Concrete Structures”, John Wiley & Sons, Inc., New York, U.S.A.
21. Sreekala, R., Lakshmanan, N., Kumar, K.S. and Gopalakrishnan, N. (2007). “Evaluation of Damage Indices for RC Beams under Cyclic Loading—A Simple Technique”, *Journal of Structural Engineering*, SERC, Vol. 34, No. 1, pp. 40–47.
22. Subramanian, N. and Rao, D.S.P. (2003). “Seismic Design of Joints in RC Structures—A Review”, *Indian Concrete Journal*, Vol. 77, No. 2, pp. 883–892.
23. Tsonos, A.G. (2000). “Effect of Vertical Hoops on the Behaviour of Reinforced Concrete Beam-to-Column Connections”, *European Earthquake Engineering*, Vol. XIV, No. 2, pp. 13–26.
24. Tsonos, A.G. (2004). “Improvement of the Earthquake Resistance of R/C Beam-Column Joints under the Influence of P- $\Delta$  Effect and Axial Force Variations Using Inclined Bars”, *Structural Engineering and Mechanics*, Vol. 18, No. 4, pp. 389–410.
25. Tsonos, A.G. (2007). “Cyclic Load Behavior of Reinforced Concrete Beam-Column Subassemblages of Modern Structures”, *ACI Structural Journal*, Vol. 104, No. 4, pp. 468–478.
26. Uzumeri, S.M. (1974). “Strength and Ductility of Cast-in-Place Beam-Column Joints”, *Proceedings of the Symposium on Reinforced Concrete Structures in Seismic Zones*, San Francisco, U.S.A., pp. 293–350.

**29th ISET Annual Lecture**

**ESTIMATION OF EARTHQUAKE GROUND MOTION IN MEXICO CITY  
AND DELHI, TWO MEGA CITIES**

Shri Krishna Singh  
Instituto de Geofísica  
Universidad Nacional Autónoma de México  
México D.F., México

**ABSTRACT**

Mexico City and Delhi are subject to strong shaking from large/great plate-boundary, thrust earthquakes located at distances exceeding ~250 km, and from moderate/large local and regional earthquakes. Since the 1985 Michoacan earthquake ( $M_w = 8$ ), which caused severe damage and loss of lives in Mexico City, our capability of ground-motion estimation in the Valley of Mexico for future earthquakes has greatly improved. A seismic alert system has been in operation since 1992, which provides ~60 s of alert time to the city before the occurrence of intense ground motion. Based on real-time recording at a reference station in the city and known transfer functions of hundreds of sites, shake maps are available within ~5 min of the arrival of S waves. Seismic instrumentation in Delhi is sparse. Our knowledge of local and regional seismicity and seismotectonics for Delhi, therefore, remains poor and estimation of ground motions and site effects is subject to large uncertainty. We illustrate some of these deficiencies from an analysis of the well-recorded Delhi earthquake of November 25, 2007 ( $M_w = 4.1$ ).

**KEYWORDS:** Seismic Hazard in Delhi, Ground Motion Estimation in Delhi, Seismotectonics of Delhi, Site Effects in Delhi

**INTRODUCTION**

It was an honour for me to give the 29th ISET Annual Lecture at Indian Institute of Technology Roorkee. I chose earthquake ground-motion estimation in the mega cities of Mexico City and Delhi as the topic of the lecture. I am more knowledgeable about Mexico City since I live and work there. My forays in ground-motion and seismic hazard estimation in Delhi have come about from sporadic collaborations with my colleagues in India.

Tectonic settings of Mexico City and Delhi to some extent are similar: both cities are subject to strong shaking from large/great plate-boundary, thrust earthquakes located at distances exceeding ~250 km, and from moderate/large local and regional earthquakes. For this reason, the experience gained in one city could be useful in the hazard mitigation in the other.

Our capability to estimate ground motion in Mexico City has radically improved since the devastating Michoacan earthquake of 1985 ( $M_w = 8$ ). Although the earthquake was located about 350 km away, it caused unprecedented damage and about 20,000 deaths in the city. It triggered eight accelerographs in the Valley of Mexico. The recordings clearly demonstrated extremely large amplifications and unusually long coda waves in the lake-bed zone of the city. These two characteristics of the ground motion were the main cause of the damage and the destruction. Since 1985 there has been a significant increase in the seismic instrumentation in Mexico (comprising both accelerographs and broadband seismographs). Presently, there are about 100 accelerographs in operation in the city, some of which are located in bore-holes, tall buildings, and on bridges. The data collected since 1985 and its analysis have permitted us a better understanding of the seismicity and source characteristics, attenuation of seismic waves from interplate earthquakes along the Mexican subduction zone and inslab earthquakes in the subducted Cocos plate below Mexico, and amplification of seismic waves in Mexico City. Transfer functions of many soft sites with respect to a reference hard site (denoted as CU) are determined based on the earthquake recordings.

Bore-hole data and interpolation are used to obtain the transfer functions at additional sites. To estimate ground motion in the city we first estimate it at CU (where extensive strong-motion recordings are available since 1965) and, then, compute it at other points in the city via known transfer functions and application of random vibration theory. The validity of this technique is extensively tested.

The fact that the city is located more than 250 km from the foci of potentially damaging interplate earthquakes along the Pacific coast of Mexico has permitted deployment of a seismic alert system (SAS). This system has been in operation since 1992 and consists of 15 accelerometers located along the coast of state of Guerrero, which is a 200 km long segment of plate boundary and is thought to be a mature seismic gap. An algorithm computes the magnitudes of events, which occur in this region, from the near-source accelerograms and issues public and restricted alerts for  $M \geq 6$  and  $5 \leq M < 6$ , respectively. SAS provides an alert about 60 s before the arrival of the large amplitude S-wave group. At present, the system has some deficiencies, e.g., limited areal coverage and error in quick magnitude estimation. Additionally, much still needs to be done to make the system socially useful.

Since the middle of 2006, a new system has been put in operation to produce, in automatic fashion, maps of the ground motion in Mexico City during earthquakes. This system relies on recording at our reference station CU. It is triggered by the detection of an earthquake at CU. As mentioned earlier, this station, located at hard site in the hill-zone of Mexico City, has been in operation since 1965 and has been used as a reference site to compute spectral amplification at all the other instrumented sites throughout the city. Once the end of the motion is detected at CU, a process starts to compute estimated average horizontal response spectra at the nodes of a grid of 1600 points with separation of approximately 500 m, using response spectral transfer functions that are pre-computed and stored in the system. The computed average horizontal response spectra at the 1600 points are used to produce maps of spectral accelerations at four periods, i.e., 0, 0.2, 1, and 2 s. These maps, along with key parameters of the ground motion, are (1) uploaded to an internet site, (2) sent by e-mail to a list of city officials and interested persons, (3) sent by cellular phone to the same list of persons, and (4) sent by radio links to the Civil Protection City Authority (this is still in a test phase).

I reiterate that much of the recent progress in ground-motion estimation in Mexico City has resulted from the improved and enlarged seismic instrumentation. Unfortunately, such instrumentation is still lacking in Delhi. In this context, an analysis of a local earthquake in Delhi, which occurred on November 25, 2007 ( $M_W = 4.1$ ) is interesting and illuminating. This is the best recorded Delhi earthquake ever. This earthquake demonstrates the uncertainty in our present knowledge. It also brings into focus the benefits of an improved seismic network (comprising accelerographs and seismographs) in and around Delhi. In this brief summary, I shall also mention some issues related to seismicity and seismotectonics of Delhi as they have direct impact on the seismic hazard estimation. Finally, the 2007 earthquake also provides the first glance at the site effects in the Indo-Gangetic Plain.

The study of the 2007 earthquake, which is still preliminary, is a collaborative effort among several researchers. I provide below a brief summary of these results. A detailed study will be published elsewhere. For brevity, I refrain from giving references to the publications on Mexico City and provide only a few dealing with Delhi.

## DELHI EARTHQUAKE OF NOVEMBER 25, 2007

### 1. Source Characteristics

Figure 1 shows the epicentre of the 2007 earthquake. The NS components of the accelerations at seven sites in and near Delhi are plotted in Figure 2. We note that the S-P times are nearly the same, suggesting a relative deep source. In fact, the computed depth is 30 km. Although the hypocentral distances are about the same, the ground motions are highly variable, thus reflecting local site effects. The largest acceleration, exceeding 100 gal ( $1 \text{ m/s}^2$ ), was recorded at BHGR (see Figure 1).

Figure 3 shows the source displacement (continuous lines) and acceleration (dashed lines) spectra,  $\dot{M}_0(f)$  and  $f^2 \dot{M}_0(f)$ , retrieved from the recording at NDI (Ridge Observatory), a hard site. Here, we ignore the method and parameters used in the estimation of source spectra. We recall that  $\dot{M}_0(f) \rightarrow M_0$

as  $f \rightarrow 0$ , where  $M_0$  is the seismic moment. The spectra in Figure 3 are reasonably well fit by a  $\omega^2$ -source model with  $M_0 = 1.9 \times 10^{15}$  N-m ( $M_w = 4.1$ ) and corner frequency of 3.92 Hz.

The focal mechanism of the earthquake was determined from the first-motion data and inversion of the displacement waveforms at NDI (see Figure 4). The focal mechanism thus obtained, with  $\phi = 31^\circ$ ,  $\delta = 86^\circ$ ,  $\lambda = -35^\circ$ , is shown in Figure 1. This mechanism is similar to those reported for two other small earthquakes in the area, which have been previously studied in some detail, i.e., on April 28, 2001 with  $H = 15$  km,  $M_w = 3.4$ , and on March 18, 2004 with  $H = 8$  km,  $M_w = 2.6$  (Bansal et al., 2009). All three events show strike-slip faulting with normal component, thus contradicting the results of Shukla et al. (2007) who reported thrust faulting with minor strike-slip component in the region. The focal mechanisms in Shukla et al. (2007) were estimated from a few P-wave polarities. For small earthquakes the first motions recorded at the stations of Delhi telemetered seismic network are often difficult to read. Further, a small number of stations and ambiguous polarities cast serious doubts on the focal mechanisms reported by Shukla et al. (2007).

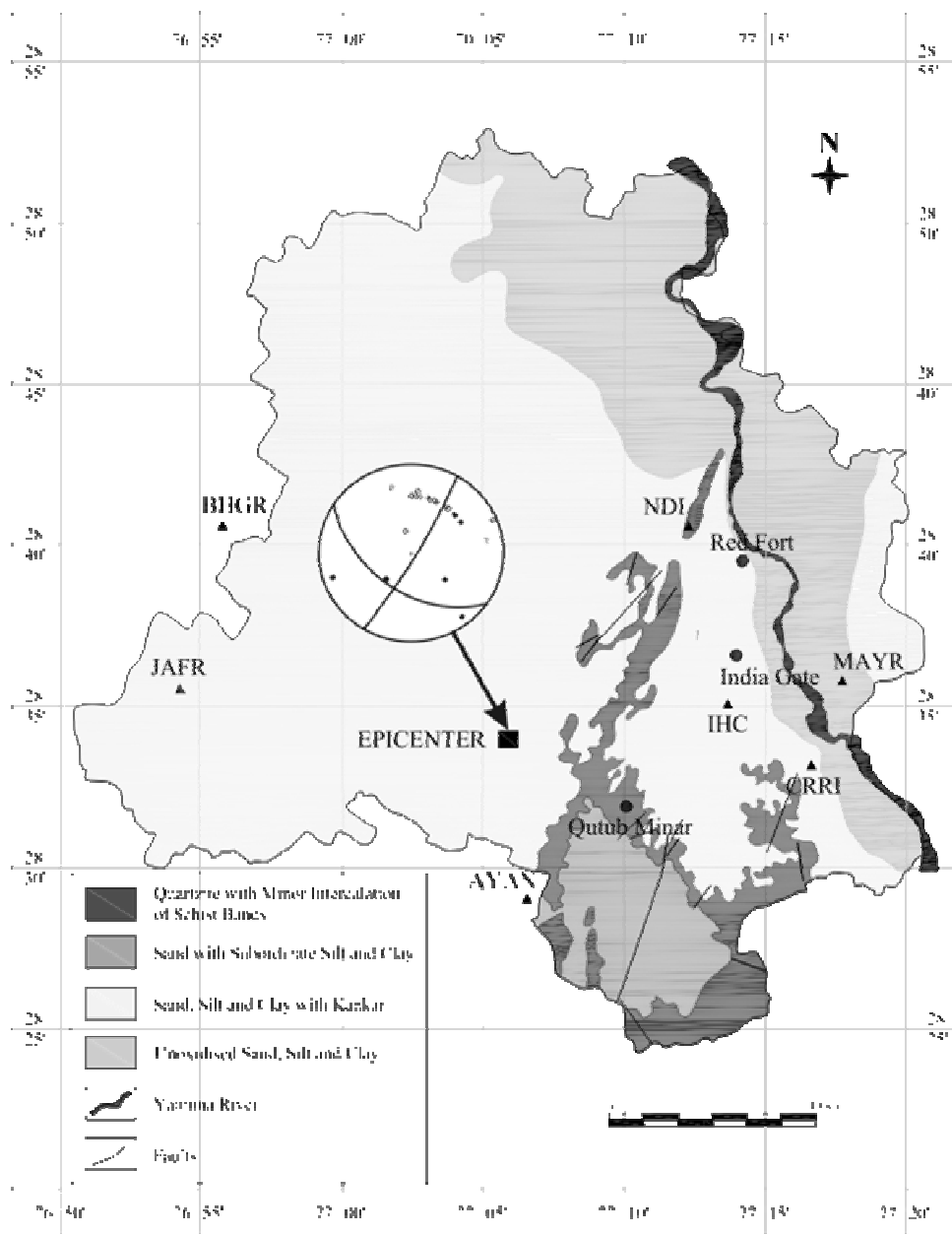


Fig. 1 Location of the November 25, 2007 Delhi earthquake and its focal mechanism determined from the first-motion data and waveform modelling of the NDI displacement traces

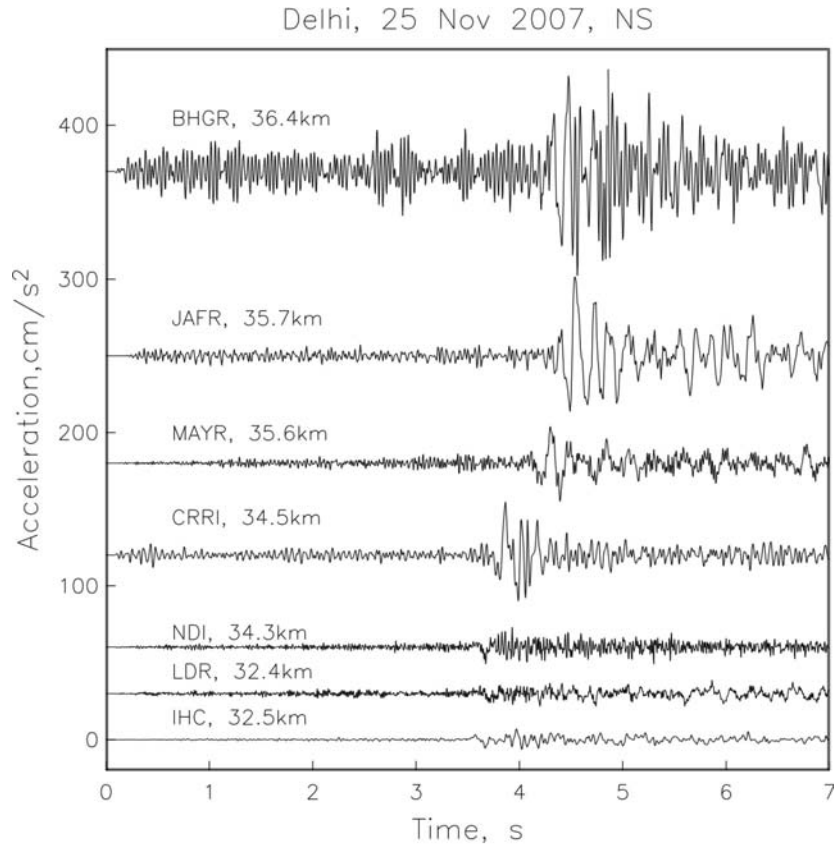


Fig. 2 NS components of the accelerograms recorded at the seven sites in and near Delhi (note similar S-P times and large variability of the ground motions)

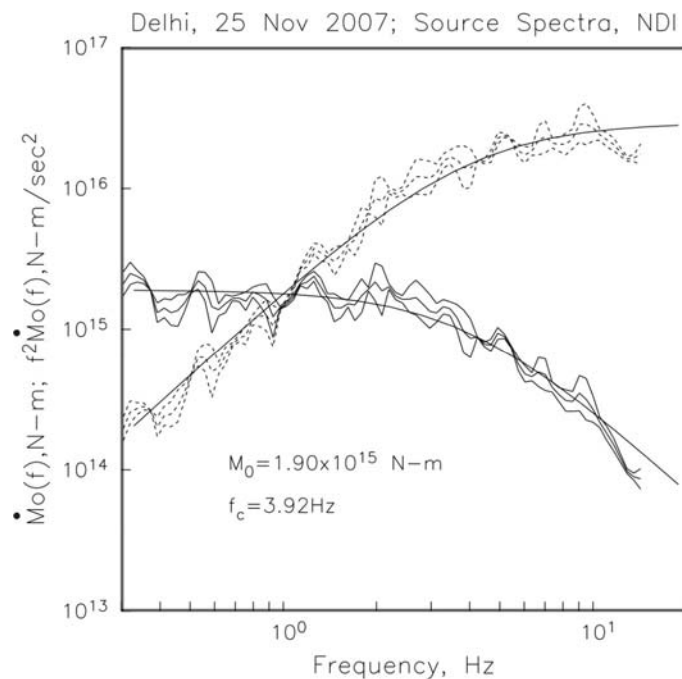


Fig. 3 Source displacement (continuous lines) and acceleration (dashed lines) spectra,  $\dot{M}_0(f)$  and  $f^2 \dot{M}_0(f)$ , of the 2007 earthquake, as retrieved from the recording at NDI, a hard site (the median and  $\pm$  one standard-deviation curves are shown; the spectra are reasonably well fit by a  $\omega^2$ -source model with seismic moment  $M_0 = 1.9 \times 10^{15}$  N-m ( $M_w = 4.1$ ) and corner frequency of 3.92 Hz)

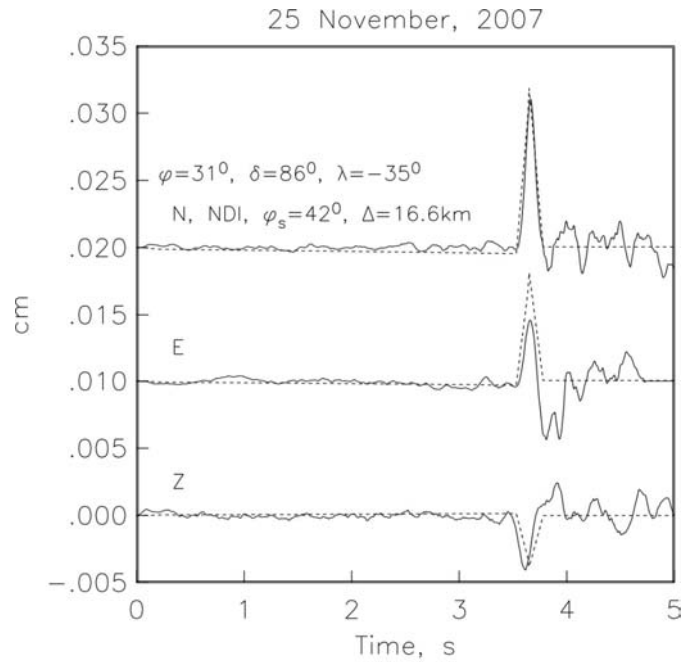


Fig. 4 Observed (continuous line) and synthetic (dashed line) displacements at NDI during the 2007 earthquake (synthetic displacements correspond to a focal mechanism of strike  $\phi = 31^\circ$ , dip  $\delta = 86^\circ$ , and rake  $\lambda = -35^\circ$ )

We also performed a regional moment tensor inversion using the 15–30 s band-pass filtered seismograms recorded by the broadband network of Wadia Institute of Himalayan Geology (see the stations to the north of the epicentre in Figure 5) and by AJMR (i.e., an IMD station located to the south in Figure 5) with the depth fixed at 30 km. The signal-to-noise ratio is low at the long periods for this relatively small earthquake. Figure 6 shows the observed and synthetic seismograms as well as the focal mechanism (with  $\phi = 64^\circ$ ,  $\delta = 81^\circ$ ,  $\lambda = 7^\circ$ ). This mechanism violates some of the first motions and differs somewhat from the one shown in Figure 1. Nevertheless, this confirms a predominantly strike-slip faulting.

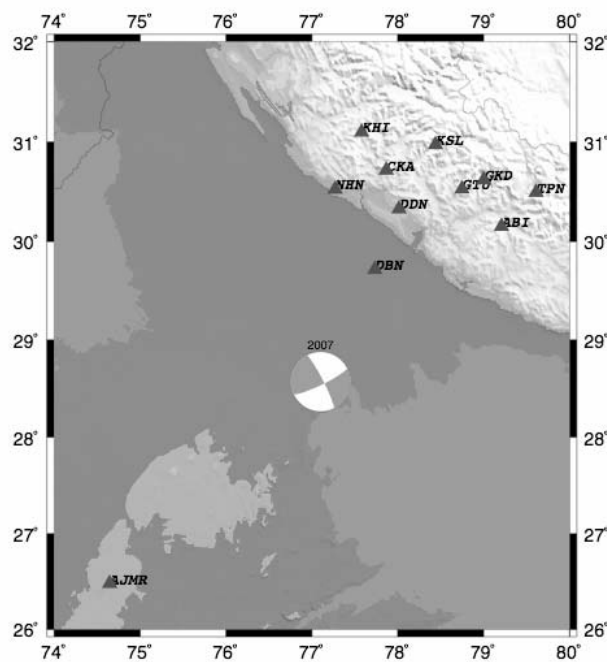


Fig. 5 Stations at the regional distances considered in regional moment tensor inversion (Stations KHI, CKA, ABI, and AJMR were used in the inversion; the focal mechanism is centred at the epicentre of the earthquake)

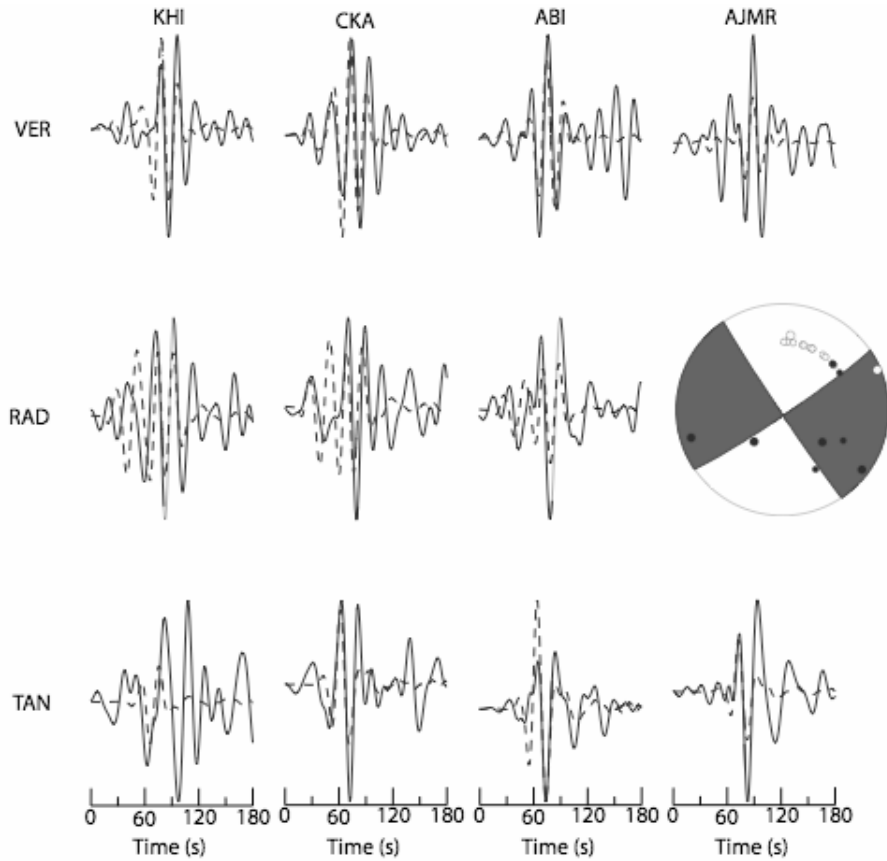


Fig. 6 Observed (continuous line) and synthetic (dashed line) seismograms corresponding to the regional moment tensor solution (the focal mechanism corresponding to the best double-couple solution is also shown in the figure)

We need to know the seismotectonics of Delhi region so that its seismicity can be properly accounted for in the seismic hazard estimation. The 2007 earthquake and the other two previously-studied events suggest a strike-slip mechanism. However, many more reliable mechanisms are needed to fully understand the state of stress in the region.

## 2. Site Effects in Delhi

Site effects can be obtained by simultaneous recording of earthquake ground motions at a reference site and the site of interest and by computing spectral ratio. For Delhi, NDI (Ridge Observatory) provides a convenient reference site. If ground motion at NDI is known (either recorded or predicted), it can be computed at other localities with known site effects through the random vibration theory. Published site effects using earthquake recordings are available only for a few sites (Singh et al., 2002; Nath et al., 2003; Bansal et al., 2009). Earthquake recordings are available at more sites, but those are currently being processed as personally communicated by Kamal and H. Mittal in 2008. Figure 7 illustrates examples of the site effects in Delhi including those obtained from the recordings of the 2007 earthquake.

Microtremors studies (e.g., Mukhopadhyay et al., 2002; various IMD reports), shear-wave velocities inferred from the bore-hole penetration data (Iyengar and Ghosh, 2004), and numerical methods (e.g., Parvez et al., 2004) have also been used to estimate the site effects in Delhi. These methods, however, require extensive validation studies. Lack of validation gives rise to serious doubts about the reliability of the results obtained by these methods. For example, the earthquake data reveals a broadband site amplification exceeding 10 at the soft sites in Delhi (see Figure 7), while the amplification estimated from the penetration data is less than about 3 (Iyengar and Ghosh, 2004). Clearly, an intensive campaign to record earthquakes at many sites in Delhi is urgently needed.

## 3. Attenuation Relation

Peak ground acceleration (PGA) and peak ground velocity (PGV) observed during the 2007 earthquake are plotted as functions of hypocentral distance  $R$  in Figure 8. Here, dots indicate hard sites,

while open circles represent soft sites. As expected, peak values (especially, the PGV values) at soft sites are significantly larger than at hard sites. The figure also shows the predicted PGA values for a  $M_w$  4.1 earthquake, as computed from the attenuation relation developed by Sharma (1998). As the figure illustrates, Sharma’s relation overestimates PGA at both hard and soft sites. This is also true for the attenuation relation of Iyengar and Ghosh (2004), which is similar to that of Sharma (1998). We tested the validity of Sharma’s relation for the Uttarkashi and Chamoli earthquakes (see Figure 9). This relation appears to be inconsistent with the data in Delhi and the broadband data at longer distances. For example, the relation predicts PGA values in Delhi for  $M_w$  5 and  $M_w$  6.5 earthquakes in the Chamoli region about 10 times greater than the observed values.

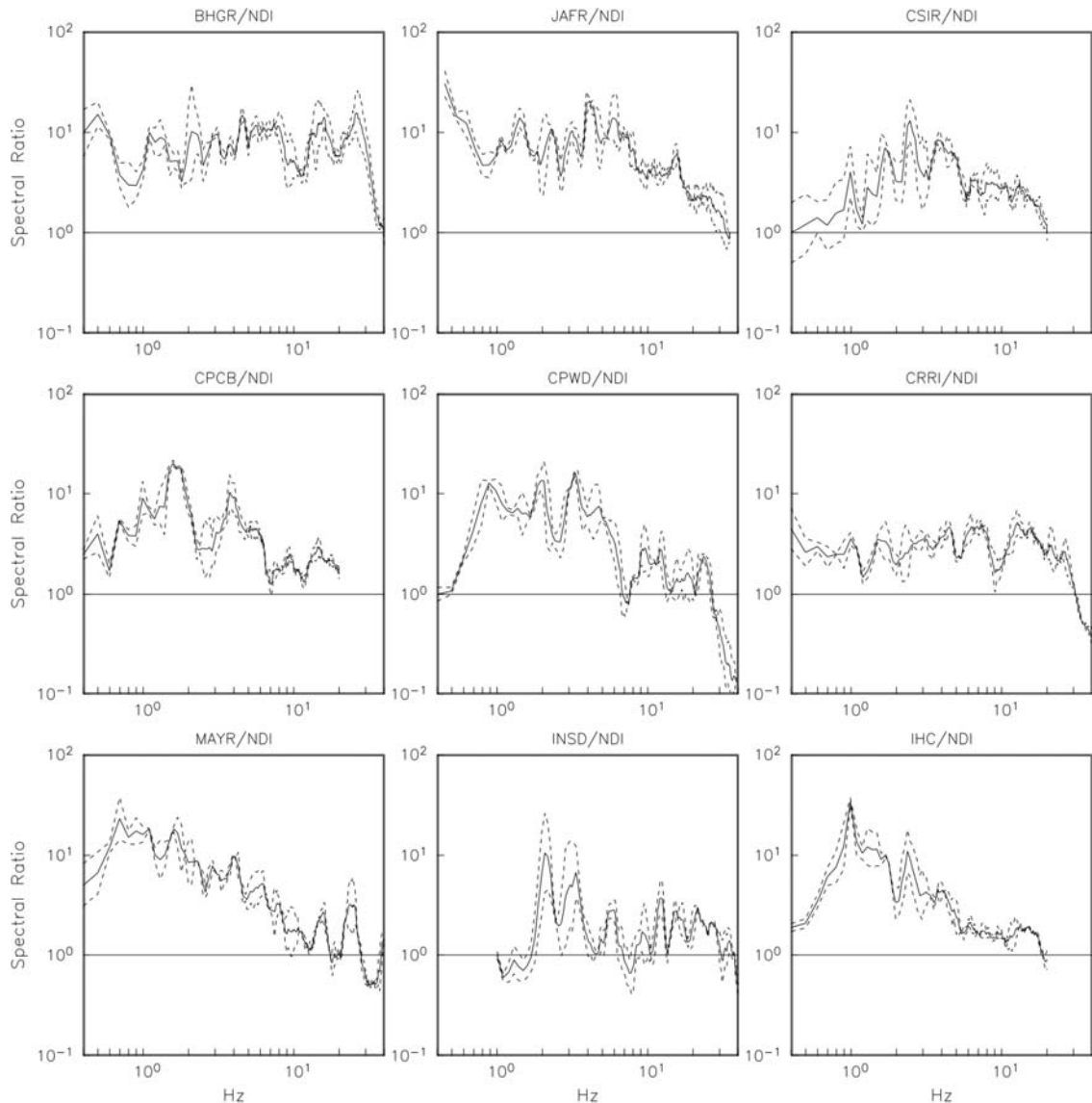


Fig. 7 Examples of the site effects in Delhi as measured by spectral ratio (i.e., the ratio of spectrum at the site of interest to the spectrum at the reference hard site of NDI) using earthquake recordings

Limited data presently available suggests that random vibration theory (RVT), in conjunction with a reasonable source model, geometric spreading, and anelastic attenuation, may provide a more reliable attenuation relation for Delhi (e.g., Singh et al., 2002, 2003). Indeed, as shown in Figures 8 and 9, the predictions based on a  $\omega^2$ -source model with the stress drop  $\Delta\sigma$  of 10 MPa along with the cutoff frequency of 35 Hz and  $Q = 508f^{0.48}$  provide a good fit for the observed data.

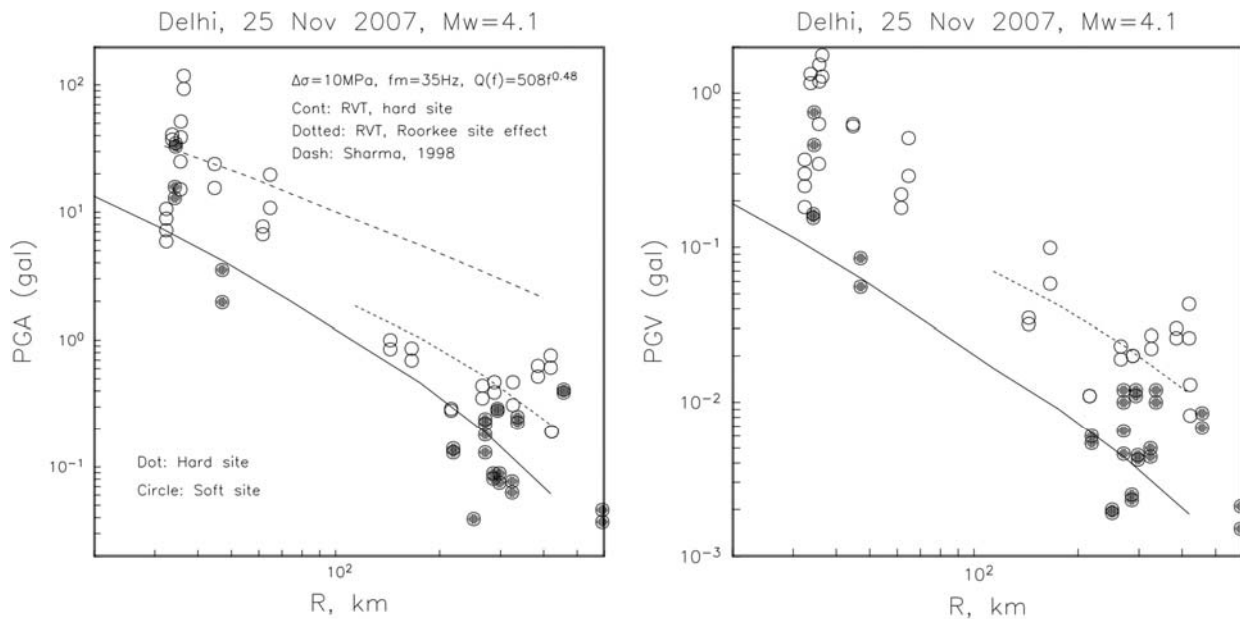


Fig. 8 PGA and PGV as functions of hypocentral distance  $R$  for the 2007 Delhi earthquake ( $M_w = 4.1$ ) (dots and open circles indicate the hard and soft sites, respectively; the figure also shows the predicted PGA for a  $M_w$  4.1 earthquake (dashed curve, left frame) from the attenuation relation given by Sharma (1998); continuous curves show the predicted PGAs and PGVs using RVT,  $\omega^2$ -source model, stress drop of 10 MPa, and cutoff frequency of 35 Hz)

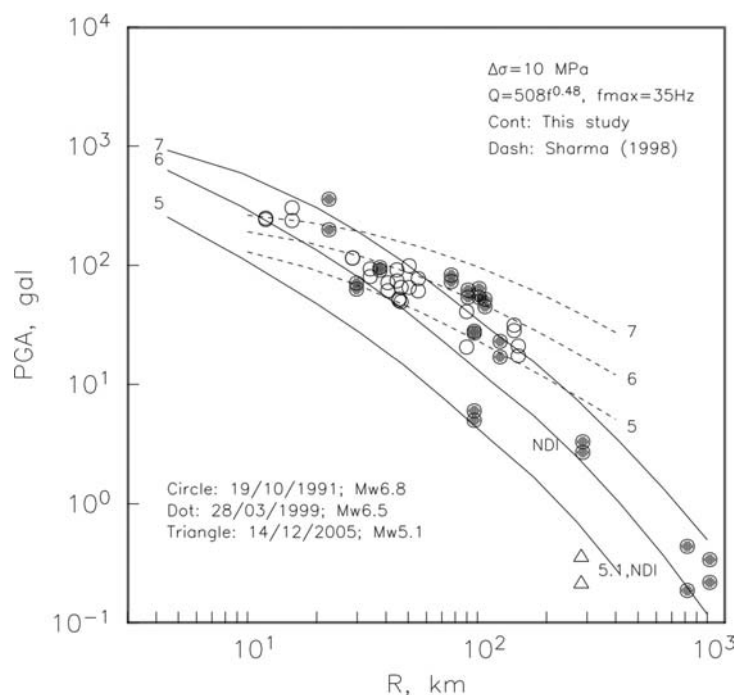


Fig. 9 PGA values during the Uttarkashi ( $M_w = 6.8$ ) and Chamoli ( $M_w = 6.5$ ) earthquakes (also shown is the PGA at NDI for an earthquake near Chamoli ( $M_w = 5.1$ )); predicted PGA curves are for the earthquakes with  $M_w = 5.0, 6.0$ , and  $7.0$  based on the attenuation relation of Sharma (1998) (dashed) and RVT assuming  $\omega^2$ -source model, stress drop of 10 MPa, and cutoff frequency of 35 Hz (continuous); the data, especially for the earthquakes of Chamoli, is inconsistent with the relation of Sharma (1998))

#### 4. Site Effects in the Indo-Gangetic Plain

Although large amplification of seismic waves in the Indo-Gangetic Plain during a large/great earthquake in the Himalayan arc is both expected and has been documented during the historical events (e.g., Hough and Bilham, 2008), no quantitative estimation of the modification of seismic waves undergone in the plain is, as yet, available. The importance of the knowledge of site effects in the plain can, therefore, be hardly overemphasized.

The data from the 2007 earthquake permits a glimpse, albeit in the linear range, of the site effects in the Indo-Gangetic Plain. The earthquake was recorded at two sites in the plain, i.e., at Deoband (DBN) and Roorkee (RKE). As mentioned earlier, it was also recorded at the hard sites of ABI, TPN, CKA, KHI and KSI in the Himalayas (see Figure 10).

We estimated site effect by comparing the spectrum at the soft site with the reference spectrum at a hard site. Since the distances to the soft and hard sites are not same, we reduced the hard-site spectra to the same distance as that of the soft site. This was accomplished by assuming that geometrical spreading is given by  $1/R$  for  $R < 100$  km for body waves and by  $1/\sqrt{R}$  for  $R \geq 100$  km for surface waves and that  $Q = 508 f^{0.48}$ . The soft-site spectra, represented by the continuous lines corresponding to the two horizontal components, and the hard-site median spectrum, represented by the dashed line, are shown in Figure 11 (see the bottom frames). The ratio of the soft-site and hard-site spectra gives the site effect. The figure shows an amplification of  $\sim 10$  at RKE in a broad frequency band of 0.1 to 5 Hz. The amplification is about 5 at DBN.

As wave paths from the Delhi earthquake to the hard sites in the Himalayas pass through the sediments of the Indo-Gangetic Plain, the spectra in the bottom frames of Figure 11 may not provide the true site effects. To correctly assess these effects, we studied the recordings of July 22, 2007 Khursali earthquake which was located near the Chamoli earthquake of 1999 (see Figure 10). The sites of ABI and TPN were taken as the reference hard sites. It may be noted that for Khursali earthquake these stations are at about the same distance as the soft-site stations of RKE and DBN. The spectra for these stations are shown in the top frames of Figure 11. As expected, the site effects in the Indo-Gangetic Plain estimated from the Khursali earthquake differ from those from the Delhi earthquake. At RKE the amplification appears to be as high as 50 in the frequency band of 0.1 to 1 Hz.

It follows clearly from the above that ground motions in the plain undergo great amplification, especially at periods greater than about 1 s. It is crucial to estimate the amplification at many sites, even if these estimates will be valid only at small strains (the linear response would, nevertheless, provide the basic element from which the nonlinear behaviour during large strains may be obtained). Scientists from National Geophysical Research Institute, Hyderabad are currently embarked on an ambitious experiment to map the site effects along a NS profile crossing the Indo-Gangetic Plain in Uttar Pradesh.

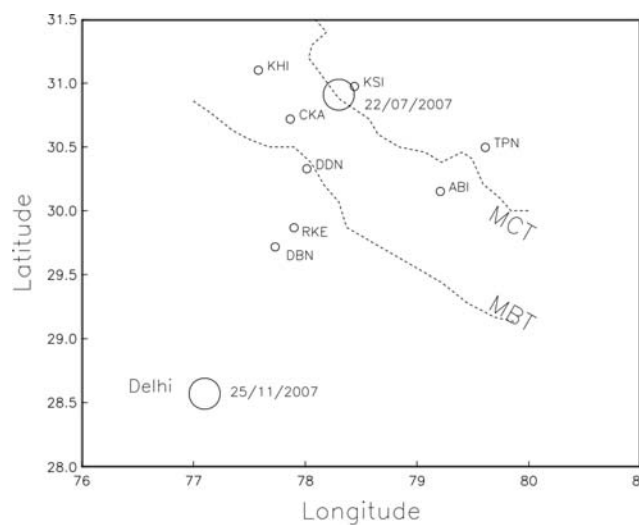


Fig. 10 Epicentres of the 2007 Delhi and 2007 Khursali earthquakes (stations in the Indo-Gangetic Plain, i.e., Deoband (DBN) and Roorkee (RKE), and hard sites in the Himalayas that recorded the two earthquakes are shown)

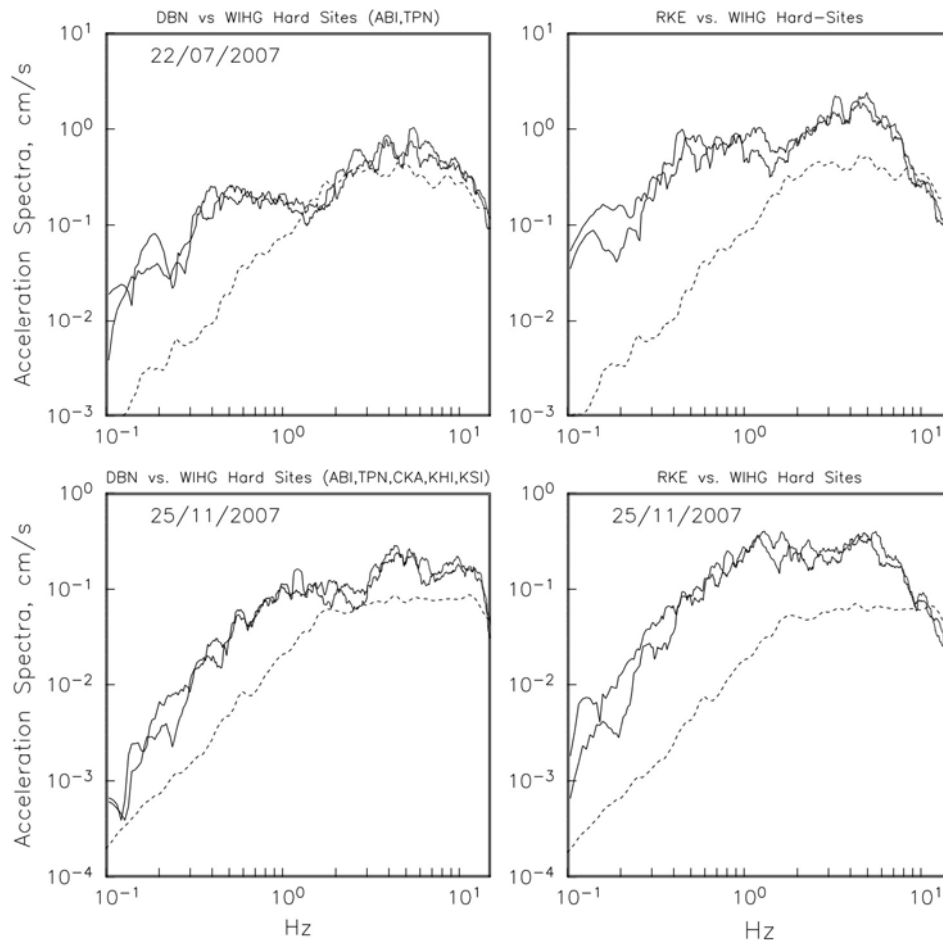


Fig. 11 Spectra at DBN and RKE (continuous lines corresponding to the two horizontal components) and normalized hard-site median spectra (dashed lines) (see the text; the ratio of soft- to hard-site spectra gives the site effects at DBN and RKE; bottom frames are for the Delhi earthquake of 2007 and top frames are for the Khursali earthquake of 2007)

## CONCLUSIONS

1. Earthquakes in the Delhi region seem associated with the strike-slip faulting with some normal component, not with the thrust faulting with a minor strike-slip component as previously reported. The NE azimuth of one of the fault planes coincides with the mapped orientation of the lineaments.
2. Attenuation relations that have been used in the seismic hazard estimation of the region are not consistent with the PGAs observed during the reasonably well-recorded 2007 Delhi event. These relations also appear to be inconsistent with the data in Delhi and the broadband data at longer distances from earthquakes in the Himalayan region. For example, predicted PGAs in Delhi from  $M_w$  5 and  $M_w$  6.5 earthquakes in the Chamoli region are about 10 times greater than the observed ones.
3. Estimation of the site effects in Delhi using the spectral-ratio technique and earthquake recordings is available only at a few points. These site effects significantly differ from those obtained from the shear-wave profiles inferred from bore-hole penetration tests. Further, the available results from various microtremor studies and theoretical works need rigorous validation before they are used in practical applications.
4. Seismicity in and around Delhi for the period 2001–2004 appears diffused (Shukla et al., 2007). It is not clear whether the scatter is real or is a consequence of the errors in the locations. Most probably both factors are involved. In the absence of precise locations, it is difficult to associate events to the

mapped faults. The percentage of events which should be considered random is therefore not known. These uncertainties lead to unreliable seismic hazard estimation.

5. A matter of serious concern is the difference in the seismicity rates of Delhi and the surrounding region (excluding the Himalayan arc) as reported by Iyengar and Ghosh (2004) and Shukla et al. (2007). The area covered in the former study is about  $2 \times 10^5$  km<sup>2</sup>, while it is  $4 \times 10^4$  km<sup>2</sup> in the latter work. The normalized seismicity rate (per year per unit area) in Iyengar and Ghosh (2004) is 10 times smaller than that in Shukla et al. (2007). What is the reason for such a large difference? One possibility is that seismicity is actually higher in a smaller area than that in a larger area. It is also possible that the earthquake catalogue used in Iyengar and Ghosh (2004) is incomplete. In any case, it is critically important to resolve this issue.
6. Results at a couple of sites in the Indo-Gangetic Plain have shown large amplification over a broad frequency range. It is of urgent need to carry out an extensive site effect study in the plain, preferably based on earthquake recordings.

In summary, our present knowledge of seismicity, seismotectonics, attenuation relation and site effects in Delhi is very poor. As a consequence, estimation of seismic hazard in the city is fraught with uncertainties. As shown above, analysis of a single, reasonably well-recorded earthquake can lead to significant improvement in our knowledge. Clearly, there is an urgent need for an improved and enlarged seismic instrumentation in and around Delhi. The recent installation of 20 accelerographs in Delhi by IIT-Roorkee should prove useful. However, only a denser network of seismographs will properly resolve the issues of seismicity, seismotectonics, and site effects.

## ACKNOWLEDGMENTS

Strong-motion and seismographic network in Mexico are funded by several institutions in Mexico including UNAM, Mexico City Government, Interior Ministry of Mexico, CONACyT, and by NSF of USA. The data from India used in this study were obtained under the projects funded by Ministry of Earth Sciences and Department of Science and Technology (DST), Government of India to IMD, WIHG, IIT-Roorkee, CBRI and NGRI. The research reported here was partly funded by CONACyT and DST under the Indo-Mexican Cooperation Programme in Science and Technology. Some results reported here are preliminary. Also, the list of authors in the final manuscript on the analysis of the 2007 Delhi earthquake will include all participants in this research.

## REFERENCES

1. Bansal, B.K., Singh, S.K., Dharmaraju, R., Pacheco, J.F., Ordaz, M., Dattatrayam, R.S. and Suresh, G. (2009). "Source Study of Two Small Earthquakes of Delhi, India, and Estimation of Ground Motion from Future Moderate, Local Events", *Journal of Seismology*, Vol. 13, No. 1, pp. 89–105.
2. Hough, S.E. and Bilham, R. (2008). "Site Response of the Ganges Basin Inferred from Re-evaluated Macroseismic Observations from the 1897 Shillong, 1905 Kangra and 1934 Nepal Earthquakes", *Journal of Earth System Science*, Vol. 117, No. S2, pp. 773–782.
3. Iyengar, R.N. and Ghosh, S. (2004). "Microzonation of Earthquake Hazard in Greater Delhi Area", *Current Science*, Vol. 87, No. 9, pp. 1193–1202.
4. Mukhopadhyay, S., Pandey, Y., Dharmaraju, R., Chauhan, P.K.S., Singh, P. and Dev, A. (2002). "Seismic Microzonation of Delhi for Ground-Shaking Site Effects", *Current Science*, Vol. 82, No. 7, pp. 877–880.
5. Nath, S.K., Sengupta, P., Srivastav, S.K., Bhattacharya, S.N., Dattatrayam, R.S., Prakash, R. and Gupta, H.V. (2003). "Estimation of S-Wave Site Response in and around Delhi Region from Weak Motion Data", *Earth and Planetary Sciences, Proceedings of the Indian Academy of Sciences*, Vol. 112, No. 3, pp. 441–462.
6. Parvez, I.A., Vaccari, F. and Panza, G.F. (2004). "Site-Specific Microzonation Study in Delhi Metropolitan City by 2-D Modeling of SH and P-SV Waves", *Pure and Applied Geophysics*, Vol. 161, No. 5-6, pp. 1165–1184.

7. Sharma, M.L. (1998). "Attenuation Relationship for Estimation of Peak Ground Horizontal Acceleration Using Data from Strong-Motion Arrays in India", *Bulletin of the Seismological Society of America*, Vol. 88, No. 4, pp. 1063–1069.
8. Sharma, M.L., Wason, H.R. and Dimri, R. (2003). "Seismic Zonation of the Delhi Region for Bedrock Ground Motion", *Pure and Applied Geophysics*, Vol. 160, No. 12, pp. 2381–2398.
9. Shukla, A.K., Prakash, R., Singh, R.K., Mishra, P.S. and Bhatnagar, A.K. (2007). "Seismotectonics Implications of Delhi Region through Fault Plane Solutions of Some Recent Earthquakes", *Current Science*, Vol. 93, No. 12, pp. 1848–1853.
10. Singh, S.K., Mohanty, W.K., Bansal, B.K. and Roonwal, G.S. (2002). "Ground Motion in Delhi from Future Large/Great Earthquakes in the Central Seismic Gap of the Himalayan Arc", *Bulletin of the Seismological Society of America*, Vol. 92, No. 2, pp. 555–569.
11. Singh, S.K., Bansal, B.K., Bhattacharya, S.N., Pacheco, J.F., Dattatrayam, R.S., Ordaz, M., Suresh, G., Kamal and Hough, S.E. (2003), "Estimation of Ground Motion for Bhuj (26 January 2001;  $M_w$  7.6) and for Future Earthquakes in India", *Bulletin of the Seismological Society of America*, Vol. 93, No. 1, pp. 353–370.

## **SEISMIC RETROFIT OF COLUMNS IN BUILDINGS FOR FLEXURE USING CONCRETE JACKET**

Gnanasekaran Kaliyaperumal\* and Amlan Kumar Sengupta\*\*

\*Division of Civil, Chemical and Environmental Engineering  
University of Surrey, Surrey GU2 7XH, U.K.

\*\*Department of Civil Engineering  
Indian Institute of Technology Madras, Chennai-600036

### **ABSTRACT**

To prevent disaster in future earthquakes, the existing deficient buildings need to be retrofitted. One way of retrofitting the columns in reinforced concrete multistoreyed buildings is concrete jacketing. The present study has investigated the effect of jacketing on the flexural strength and performance of columns. First, slant shear tests were conducted to study the interface between the old and new concrete. Second, column specimens were tested to study the strength. Third, beam-column-joint sub-assembly specimens were tested to study the ductility (or energy absorption) and energy dissipation. Analytical investigations were carried out to predict the experimental results. A lamellar approach and a simplified method of analysis were used for the prediction of the axial load versus moment interaction curves and moment versus curvature curves for the retrofitted columns. An incremental nonlinear analysis was adopted to predict the lateral load versus displacement behaviour for a retrofitted sub-assembly specimen. Guidelines for the retrofitting of columns by concrete jacketing are provided.

**KEYWORDS:** Beam-Column-Joint Sub-assembly, Column, Concrete Jacketing, Lamellar Analysis, Retrofit

### **INTRODUCTION**

Recent earthquakes have exposed the vulnerability of reinforced concrete (RC) buildings. The earthquake at Bhuj, Gujarat, in 2001 has been a watershed event in the earthquake engineering practice in India. The Indian code of practice for seismic analysis has been revised to reflect the increased seismic demand in many parts of the country. Many existing buildings lack the seismic strength and detailing requirements of the current codes of practice, because they were built prior to the implementation of these codes. Failure of columns can lead to the failure of a storey and the building. The columns in a typical multistoreyed RC building in India, especially with an open-ground storey (i.e., a ground storey without any infill walls for vehicle parking), are found to be deficient with respect to their flexural and shear strengths as compared to the corresponding demands. Under moderate to severe earthquakes, an undesirable column side-sway can lead to a soft-storey collapse mechanism.

The Department of Civil Engineering at Indian Institute of Technology Madras and the Structural Engineering Research Centre, Chennai undertook a project to study the vulnerability of typical multistoreyed RC buildings in India. The project was funded by Department of Science and Technology, Government of India. From the analysis of 18 residential buildings, it was found that on average 22% and 39% of the lower storey columns are deficient in flexure for the Zone III and Zone V buildings, respectively (Kamat and Sengupta, 2006). For the two zones, the horizontal components of peak ground acceleration are 0.16g and 0.36g, respectively, where  $g$  is the acceleration due to gravity. For deficiency in shear, the corresponding values are 84% and 54%, respectively. It was observed that for some buildings, all columns in the lowest storeys are deficient in shear. Since shear failure in columns in a storey can lead to the pancake type collapse of a building, many multistoreyed buildings in India are highly vulnerable.

The deficiencies in the buildings, which were damaged or collapsed during the Bhuj earthquake, were reported by Murty et al. (2002). A few other observations were made in the project mentioned earlier (IITM-SERC, 2005).

Apart from an inadequate number of continuous frames in both directions, improper layout and orientation of columns, common deficiencies specific to the columns in RC buildings include

- Inadequate and disproportionate dimensions of the column section, leading to inadequate flexural and shear capacities in the columns of open ground storey. The practice of providing 230 mm wide columns in the lower storeys may result in significant inadequacy in strength.
- Inadequate spacing of ties at the potential plastic hinge regions, leading to lack of ductility.
- Inadequate flexural capacity due to weak construction joints, and poor detailing of ties, such as warped ties (i.e., the ties which are not in a single plane after bending the bar manually), and lack of adequate end hooks.
- Location of splice for the longitudinal bars just above the floor level, and inadequate splice length as compared to the requirement based on tension in the bars.
- Short captive columns created in the presence of partial-height infill walls and openings in the walls.
- Lower concrete strength than the design strength, and concrete of poor quality with inadequate compaction at the top of the columns.

To prevent disaster in future earthquakes, the existing deficient buildings need to be retrofitted. Selection of an appropriate retrofit scheme is based on the seismic evaluation of a building and the available resources. For a building, a combination of retrofit strategies may be selected under a retrofit scheme. Retrofit strategies may be broadly classified as local and global strategies (see Figure 1). The global retrofit strategies are applied to improve the overall behaviour of the building. In addition to a global retrofit strategy, it may be necessary to retrofit some columns. The latter can be considered as a local retrofit strategy.

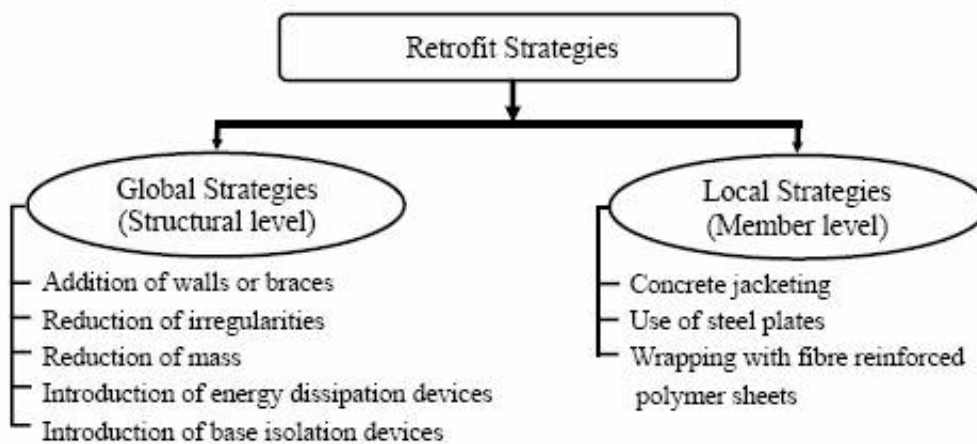


Fig. 1 Types of retrofit strategies

One way of retrofitting the columns is by concrete jacketing. Concrete jacketing involves placing an additional layer of concrete covering the existing column, together with additional longitudinal bars and ties to enhance the flexural and/or shear capacities. The retrofitting of columns by concrete jacketing is not sufficiently documented. In a conventional analysis of a jacketed column, strength is determined based on an interaction diagram for the composite section or for some equivalent section. The present paper reports an investigation of the strength of jacketed columns and the performance of jacketed columns in beam-column-joint sub-assemblages. Only the flexural deficiency of such columns is addressed in this study.

In the conventional method, a column is analysed or designed by using the interaction charts of axial load and bending moment. This is a strength-based approach. However, for analyzing and designing for the seismic forces, a performance-based approach is preferred. In this approach, not only the strength of a structural component is evaluated, but also the load versus deformation behaviour is quantified. Next, testing a beam or column specimen under a static monotonically increasing load does not demonstrate the behaviour of members near the beam-to-column joints under seismic loads, which are dynamic and cyclic in nature. The degradation of strength and stiffness of the members and deterioration of bond between the steel reinforcing bars (or rebars) and concrete, especially near the joints, cannot be simulated by the monotonic loading of individual specimens. Hence, it is necessary to test the beam-column-joint sub-assemblages under at least a quasi-static or pseudo-dynamic loading in order to study the effect of retrofit.

## LITERATURE REVIEW

The advantages of concrete jacketing in the context of construction in India are as follows (Chakrabarti et al., 2008):

- Jacketing by concrete can increase both flexural and shear capacities of a column.
- The compatibility of deformation between old and new concrete, and the durability are better as compared to a new material on a different substrate.
- Availability of personnel skilled in concrete construction.
- Analysis of retrofitted sections follows the principles of analysis of RC sections.

Of course, there are certain disadvantages of concrete jacketing depending upon the structure and its use:

- increase in the size of the column and reduction in floor space,
- anchoring of bars for flexural strength involves drilling of holes in the slabs and footings,
- manufacturing of sufficiently workable concrete for the jacket, and
- possibility of disruption to the users of the building.

Despite the disadvantages, concrete jacketing is a practical option for the buildings where columns are highly deficient in flexure or shear as compared to the required performance.

Aguilar et al. (1989) studied 114 buildings which were retrofitted after the Mexico earthquake in 1985. It was concluded that the most commonly used retrofit strategy in the buildings less than 12 storeys was that of concrete jacketing of columns.

Bett et al. (1988) have shown that columns strengthened by jacketing, both with and without supplementary cross-ties, were much stiffer and stronger than the original, unstrengthened columns. Saatcioglu and Ozcebe (1989) pointed out that a cross-tie with 90° hook at one corner and with extension of 10 times the bar diameter performs as satisfactorily as that with 135° hook at both ends and with similar extension. Bousias and Fardis (2003) proved that concrete jacketing is very effective in removing the adverse effect of lap splicing on flexural capacity, even for very short lap lengths.

Alcocer (1993) (also Alcocer and Jirsa, 1993) tested beam-column-slab specimens under bidirectional cyclic loading to study the effect of jacketing on the shear strength of joints. Different layouts of the additional longitudinal bars of the columns were studied. It was concluded that although distributed bars are preferred for good bond behaviour, bundling of bars near the corners of the column were effective in increasing the strength, stiffness and energy dissipation characteristics of the specimens. Ersoy et al. (1993) concluded that a retrofitted column behaved better when the jacket was constructed after unloading the column.

Valluvan et al. (1993) tested column specimens with lap splicing of the longitudinal bars. From the tests it was concluded that removing the concrete cover for adding the new ties is not an effective method for strengthening the splice location because it results in micro-cracking of the concrete core. External reinforcement (i.e., steel element or tie) around the splice region significantly improves the confinement of the concrete and the strength of the splice. Steel dowels were inserted at the face of the original columns for better transfer of shear at the interface of the old concrete and the jacket.

Rodriguez and Park (1994) tested jacketed columns with stub beams. The additional longitudinal bars in a specimen were placed in bundles near the corners of the column and passed through drilled holes in the slab. Additional ties at the joint were inserted by drilling the stub beams. Significant improvements of the lateral stiffness, strength and ductility of the specimens were observed.

Vandoros and Dritsos (2006) designed and tested a typical ground storey column of a framed building under displacement-controlled cyclic loading. Self-compacting concrete was used in the jacket. The longitudinal bars of the original column were connected to the additional longitudinal bars in the jacket with steel inserts. It was found that an almost monolithic behaviour could be achieved, when the jacket was constructed with dowels but without any treatment of the old surface. Significant increases in strength and stiffness were observed.

Regarding the bonding between old and new concrete, Stoppenhagen et al. (1995) roughened the column surface with an electric concrete hammer to achieve a monolithic behaviour of the entire concrete. Abu-Tair et al. (1996) adopted the slant shear test and modified modulus of rupture test to study the effect of surface treatment on the bond strength at the interface, under monotonic and cyclic loadings. It was concluded that both tests are effective for studying the bond strength.

Austin et al. (1999) compared the bond strength through tensile pull-out tests. The effect of surface preparation and the mismatch of the moduli of the repair material and substrate were studied. A failure envelope was presented based on the Mohr-Coulomb theory and Griffith fracture criterion.

Tests for bond and the effects of bond coats, surface preparation and ageing of the base concrete were conducted by Climaco and Regan (2001). The test results were analyzed by using the Coulomb criterion. When the base surface is dry, good bond can be achieved by casting the repair material against the old concrete without any bonding agent. Julio et al. (2003) investigated the effects of surface preparation, bonding agents and steel connectors. It was concluded that the monolithic behaviour of a jacketed member can be achieved by using bonding agents or steel connectors, without increasing the surface roughness.

Beushausen and Alexander (2008) tested the following types of surface preparation:

- sand blasted,
- plain, without any intentional roughening, and
- notched surface.

From the tests it was found that the notched surface showed higher bond strength than the sand blasted and the plain interfaces, even at 26 months after casting of the new concrete.

## SLANT SHEAR TESTS

For an effective concrete jacket, the use of dowels involves closely spaced drilling of the existing concrete. If the latter is of low strength or poor quality, the drilling may worsen the existing member. Also, the drilling may intercept the existing bars. Hence, to minimize drilling, the use of dowels is precluded and only preparation of the surface of the existing member is investigated in the present study of retrofit for flexure. Slant shear tests were carried out in the present investigation to check the interface bond between old and new concrete.

### 1. Test Setup

The tests were conducted with the square prisms made of new concrete cast against the sloping faces of the old concrete, as shown in Figure 2. The procedure as per BS 6319 (BSI, 1984) was followed. The specimen size was 150×75×75 mm. The old concrete was cured for 28 days before casting of the new concrete. For different specimens, the faces of old concrete were either plain without any intentional roughening, or roughened by motorized wire brush, or were hacked by chisel. For each of these types of surfaces there were two varieties: one without any application of the bonding agent, and another with the smearing of bonding agent.

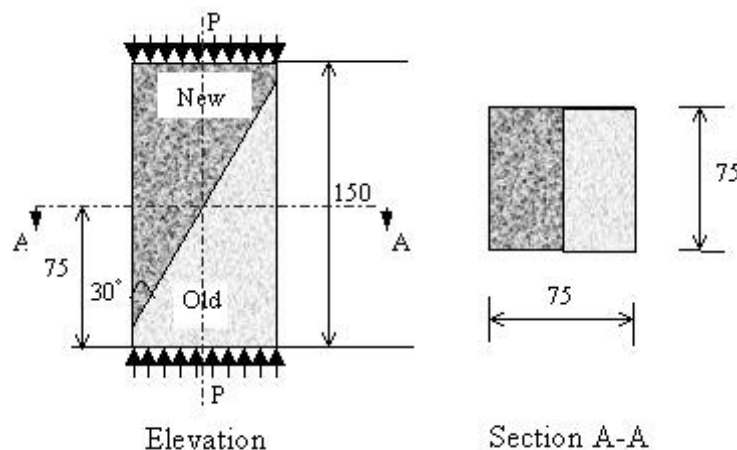


Fig. 2 Schematic diagram for the slant shear test (all dimensions are in mm)

The prisms were tested under compression after an additional 28 days of curing. The average values of the individual cube strengths of the old and new concrete were 32 and 44 N/mm<sup>2</sup>, respectively.

**2. Test Results**

The typical failure pattern of a specimen with roughened surface is shown in Figure 3. The failure loads are given in Table 1. Figure 4 shows the corresponding values of average failure stress. From the results, it was found that the specimens with roughened surface of the old concrete and without any bonding agent failed at higher loads compared to the other specimens. Thus, it was decided that for the retrofitted column and sub-assembly specimens, the faces of the old concrete would be roughened and bonding agent would not be used.



Fig. 3 Failure pattern of a specimen with roughened surface

**Table 1: Failure Loads (in kN) for Different Specimens of Slant Shear Tests**

Surface Preparation	A1	A2	A3	B1	B2	B3	C1	C2	C3
	Without Chemical			With Chemical 1			With Chemical 2		
Plain	No test was performed			25	35	30	10	05	–
Roughened	110	135	170	15	55	50	10	05	10
Hacked	140	90	90	35	35	20	05	10	–
Specimens C3 with the plain and hacked surface preparations were defective.									

**TESTS OF COLUMNS**

It is necessary to predict the strength of a retrofitted column in order to estimate the effect of retrofit. In this study, first the columns were tested to investigate the increase in axial load capacity and flexural strength due to the concrete jacketing. To develop interaction curves for the reference (with suffix O) and retrofitted (with suffix R) specimens, nine specimens were tested for each case. For each case, three specimens were tested under each of pure compression (PC), eccentric compression (EC), and pure uniaxial bending (PB).

**1. Test Setup**

Column specimens were tested under pure compression and eccentric compression by using a column testing machine. The specimens under pure bending were tested using a frame which is described later. The elevations of the test setups are shown in Figure 5. For a test under eccentric compression, the compressive load  $P$  was applied at an eccentricity  $e$  about one axis. The values of eccentricity were

selected corresponding to the theoretical balanced failure points of the interaction curves and were rounded off to suitable integral values. Rocker bearings were placed at the top and bottom of the specimens to develop the pinned end conditions.

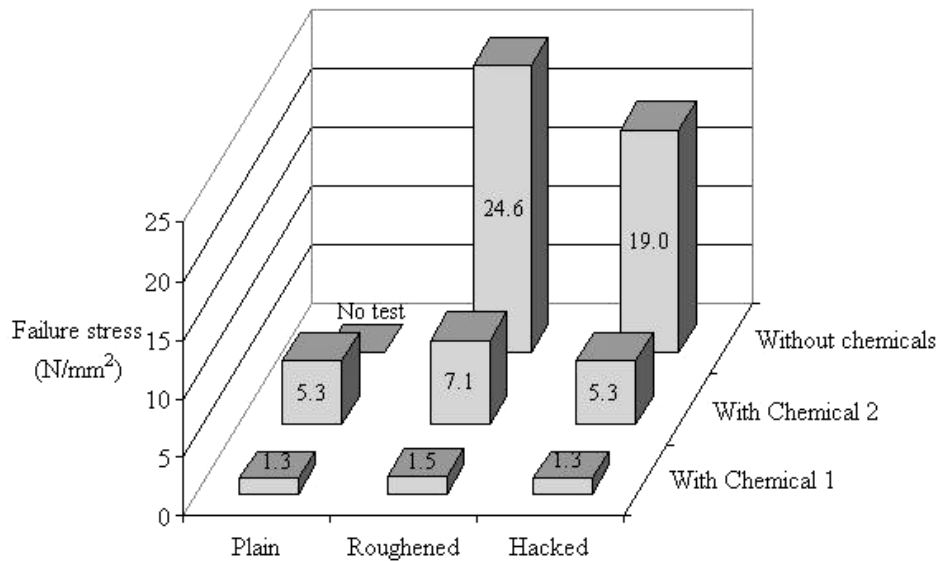


Fig. 4 Average failure stress for the specimens of slant shear tests

A load cell was used to record the applied load. Linear variable differential transducers (LVDTs) were used to measure the deformations over certain gage lengths. The average strains and curvatures were calculated from the deformation readings. A data acquisition system was used to record the load cell and LVDT readings.

## 2. Specimen Details

### 2.1 Reference Specimens

A reference specimen simulates the as-built column. The reinforcement details of the specimens are shown in Figure 6. To simulate the conventional practice, the end hooks of the ties of the reference specimens were provided with 90° bends instead of the 135° bends. For the specimens tested under pure compression, the ends were flared symmetrically to a cross-section of 200×200 mm to avoid stress concentration and subsequently local failure. For the specimens tested under eccentric compression, the ends were flared asymmetrically to a cross-section of 300×200 mm. For the reference specimens, a concrete mix of 1:2.35:4.7 (cement: fine aggregate: coarse aggregate) with water-to-cement ratio of 0.5 was used. Table 2 provides the material properties for the column specimens.

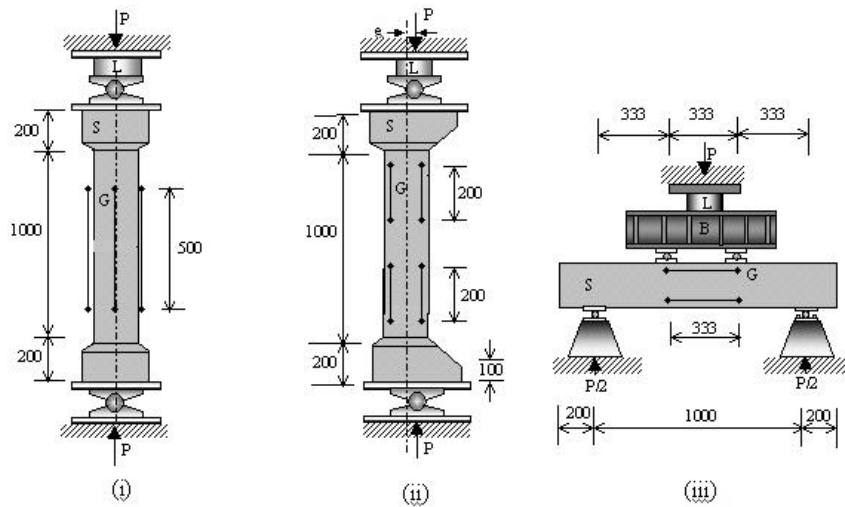
### 2.2 Retrofitted Specimens

For a retrofitted specimen, the cross-section, reinforcement detailing and concrete mix of the inner portion were similar to those of the corresponding reference specimen. The reinforcement details for the jackets are shown in Figure 7. For the specimens tested under pure compression, the cross-section of the flared ends was 300×300 mm. For the specimens tested under eccentric compression, the cross-section of the flared ends was 500×300 mm.

The jackets of the retrofitted specimens were made of self-compacting concrete (SCC). After several trials, a design mix of the SCC was formulated and flowability was tested by the slump flow test. Segregation of the concrete was not observed in the test. Photographs of the fabricated reinforcement for the retrofitted specimens are shown in Figure 8.

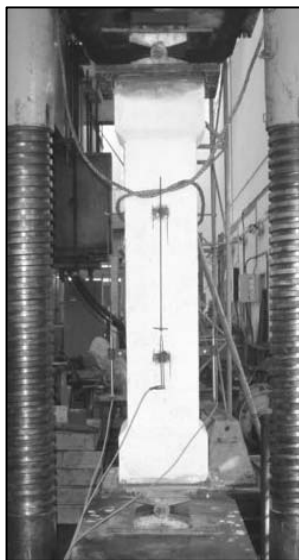
Spacing of the ties in the jacket was kept close (but limited to the minimum spacing) in order to increase the confinement of the concrete of the inner portion. The reference specimens and the inner portion of the retrofitted specimens were cast horizontally. Since the height of the specimens was 1400 mm (including the flares), segregation of the concrete was not expected even if cast vertically. The jackets of the specimens tested under pure compression and eccentric compression were cast vertically to

simulate the actual method of construction. The jackets of the specimens tested under pure bending were cast horizontally in order to use an adjustable formwork.



B = Spreader beam, e = eccentricity, L = Load cell, G = LVDT gage, P = Applied load, S = Specimen  
 $g = 50$  mm for reference specimens and 100 mm for retrofitted specimens.

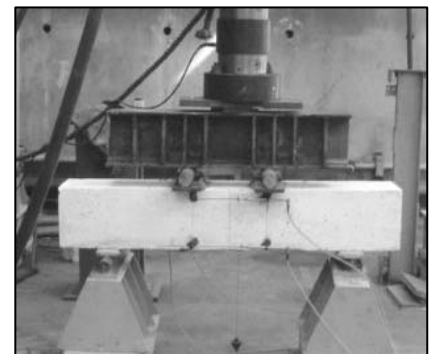
(a)



(i) Pure Compression



(ii) Eccentric Compression



(iii) Pure Bending

(b)

Fig. 5 Setups for testing column specimens (all dimensions are in mm): (a) schematic diagrams, (b) photographs of the retrofitted specimens

### 3. Test Results

#### 3.1 Reference Specimens

The specimens tested under pure compression failed due to lateral buckling of the longitudinal bars between the ties followed by the crushing of concrete (see Figure 9). This was expected as the tie spacing was large compared to the size of the longitudinal bars. The specimens tested under eccentric compression showed substantial cracking on the tension side and subsequently lateral buckling of the longitudinal bars between the ties and crushing of the concrete on the compression side. The lateral ties did not open under the static load. For the specimens tested under pure bending, the initiation of yielding of the longitudinal bars on the tension side was followed by the crushing of concrete on the compression

side. The failure loads for the column specimens are given in Table 3. The loads were subsequently normalized to have non-dimensional ratios for plotting in a common graph.

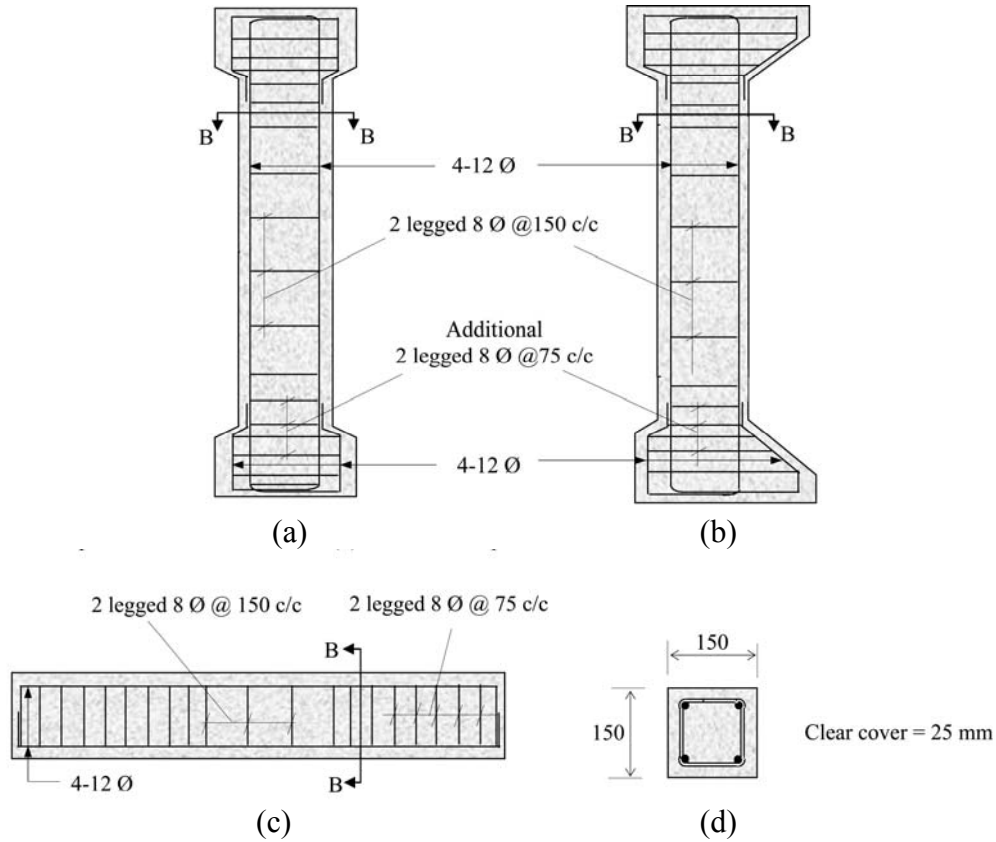


Fig. 6 Reinforcement details of the reference specimens for column tests (all dimensions are in mm): (a) pure compression, (b) eccentric compression, (c) pure bending, (d) Section B-B

Table 2: Material Properties for Column Specimens

Series	Reference		Retrofitted*			Reference and Retrofitted	
	Specimen Designation	$f_{cm}$	Specimen Designation	$f_{cmE}$	$f_{cmJ}$	$f_{yl}$	$f_{yt}$
Pure Compression (PC)	PCO 1	23	PCR 1	24	31	413	480
	PCO 2	31	PCR 2	24	43		
	PCO 3	22	PCR 3	24	24		
Eccentric Compression (EC)	ECO 1	23	ECR 1	33	20		
	ECO 2	31	ECR 2	45	21		
	ECO 3	22	ECR 3	38	19		
Pure Bending (PB)	PBO 1	22	PBR 1	24	31		
	PBO 2	23	PBR 2	24	43		
	PBO 3	40	PBR 3	24	24		

$f_{cm}$  = mean cube strength of concrete (in MPa),  $f_{cmE}$  = mean cube strength of existing concrete (in MPa),  $f_{cmJ}$  = mean cube strength of jacket concrete (in MPa),  $f_{yl}$  = yield strength of longitudinal bars (in MPa),  $f_{yt}$  = yield strength of transverse bars (in MPa), modulus of elasticity for steel =  $2.02 \times 10^5 \text{ N/mm}^2$

\*In a few specimens, the compressive strength of concrete in the jacket came out to be lower than that for the existing concrete because of the different periods of curing and trial mixes of the self-compacting concrete.

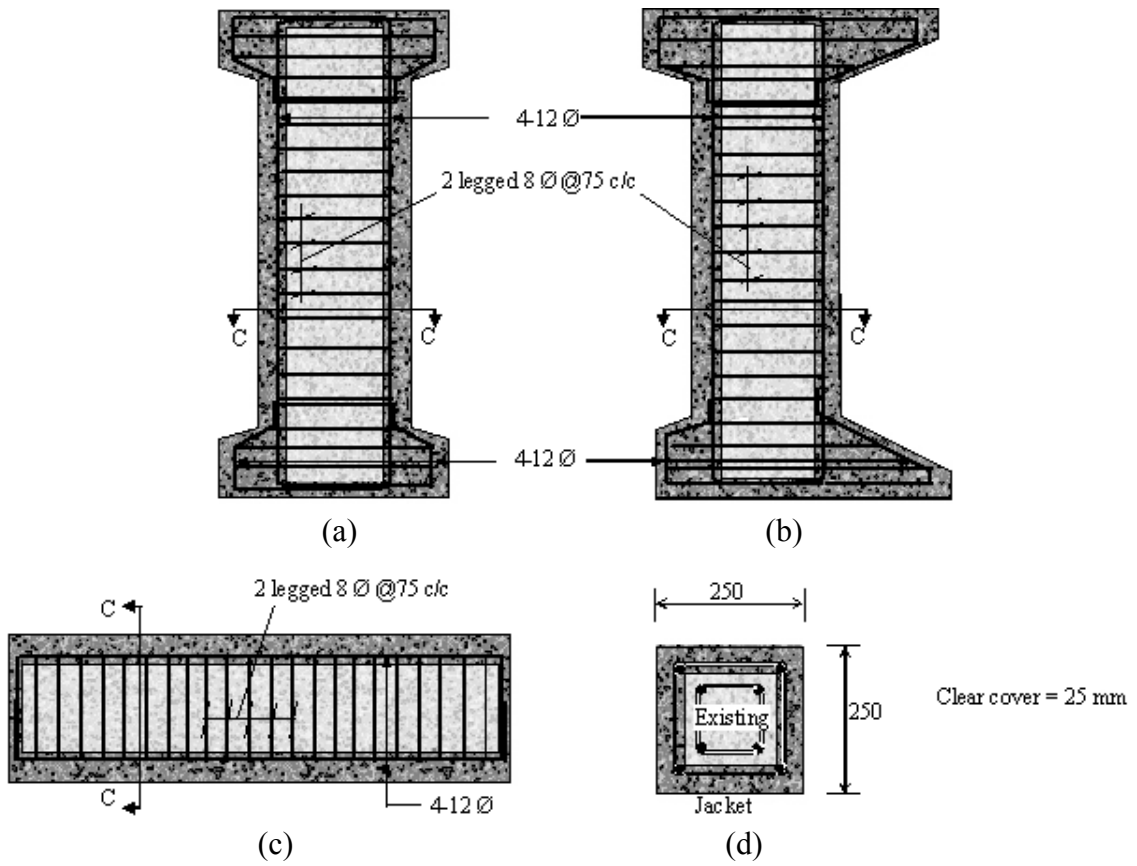


Fig. 7 Reinforcement details of the retrofitted specimens for column tests (all dimensions are in mm): (a) pure compression, (b) eccentric compression, (c) pure bending, (d) Section C-C (these bars are in addition to those in the original cross-sections, which are same as in the reference specimens; see Figure 6)

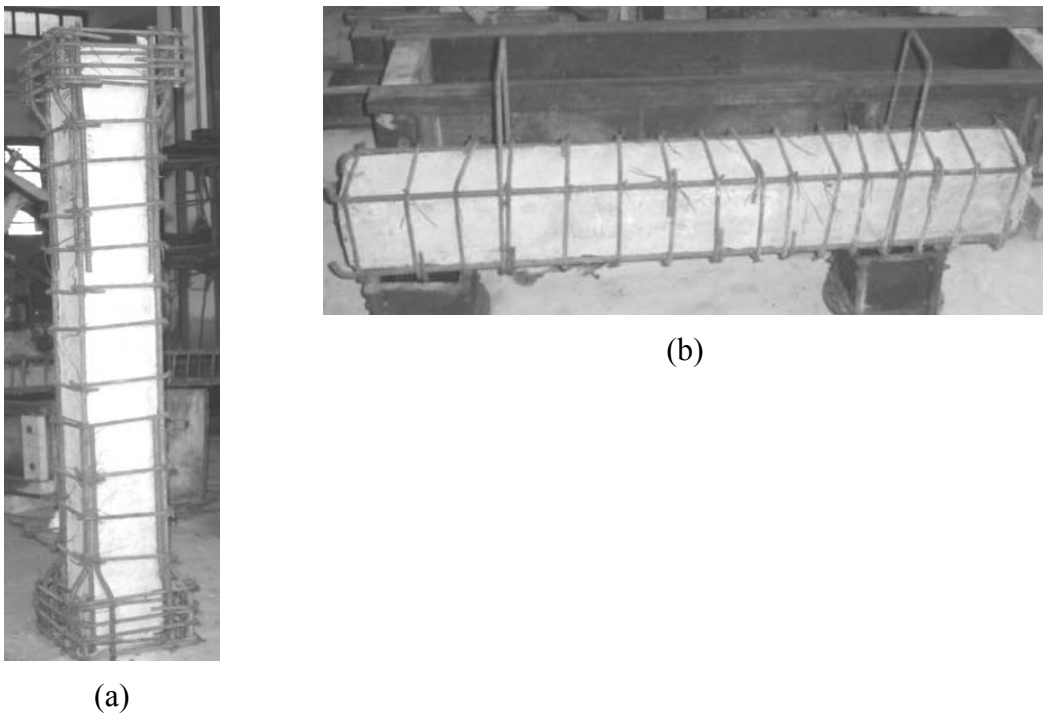


Fig. 8 Photographs of fabricated reinforcements of the retrofitted specimens for column tests: (a) pure compression, (b) pure bending

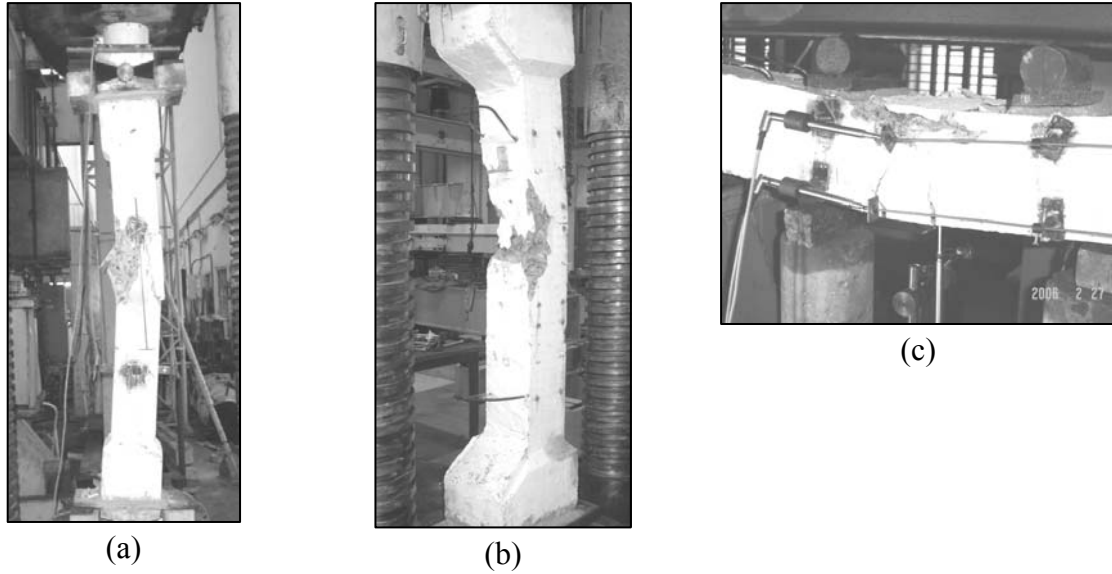


Fig. 9 Photographs of reference specimens after (typical) testing: (a) pure compression, (b) eccentric compression, (c) pure bending

Table 3: Failure Loads for Column Specimens

Type of Specimen	Specimen Designation	Axial Load $P_{UR}$ (kN)	Moment $M_{UR}$ (kN-m)	$\frac{P_{UR}}{f_{cm} BD}$	$\frac{M_{UR}}{f_{cm} BD^2}$
Reference	PCO 1	646	0	1.25	0
	PCO 2	720	0	1.03	0
	PCO 3	560	0	1.13	0
	ECO 1	250	12.5	0.48	0.16
	ECO 2	260	13.0	0.37	0.12
	ECO 3	250	12.5	0.51	0.17
	PBO 1	0	7.0	0	0.10
	PBO 2	0	13.3	0	0.17
	PBO 3	0	8.6	0	0.07
Retrofitted	PCR 1	1350*	0	0.90	0
	PCR 2	2150	0	1.43	0
	PCR 3	1565	0	1.04	0
	ECR 1	547	54.7	0.27	0.11
	ECR 2	506*	50.6	0.18	0.07
	ECR 3	573	57.3	0.24	0.10
	PBR 1	0	37.5	0	0.10
	PBR 2	0	36.5	0	0.10
	PBR 3	0	38.2	0	0.10

$f_{cm}$  = mean cube strength of the concrete for a reference specimen,  $f_{cm} = f_{cmE}$  = mean cube strength of the existing concrete for a retrofitted specimen,  $B$  = width of the column,  $D$  = depth of the column

\*The specimen had local failure.

### 3.2 Retrofitted Specimens

The specimens tested under pure compression failed by crushing of the concrete of both jacket and core (see Figure 10). There was no visible delamination of the jacket. Also, light tapping by a hammer did not reveal any air gap or cause the jacket concrete to chip off. For the specimens tested under eccentric compression, there was no visible difference in the crushing of the old and new concrete. Specimens PCR 1 and ECR 2 showed premature local crushing of the concrete near the flares. For the specimens

tested under pure bending, along with yielding of the bars and crushing of concrete under compression, portions of the jacket between the ties delaminated on the tension side.

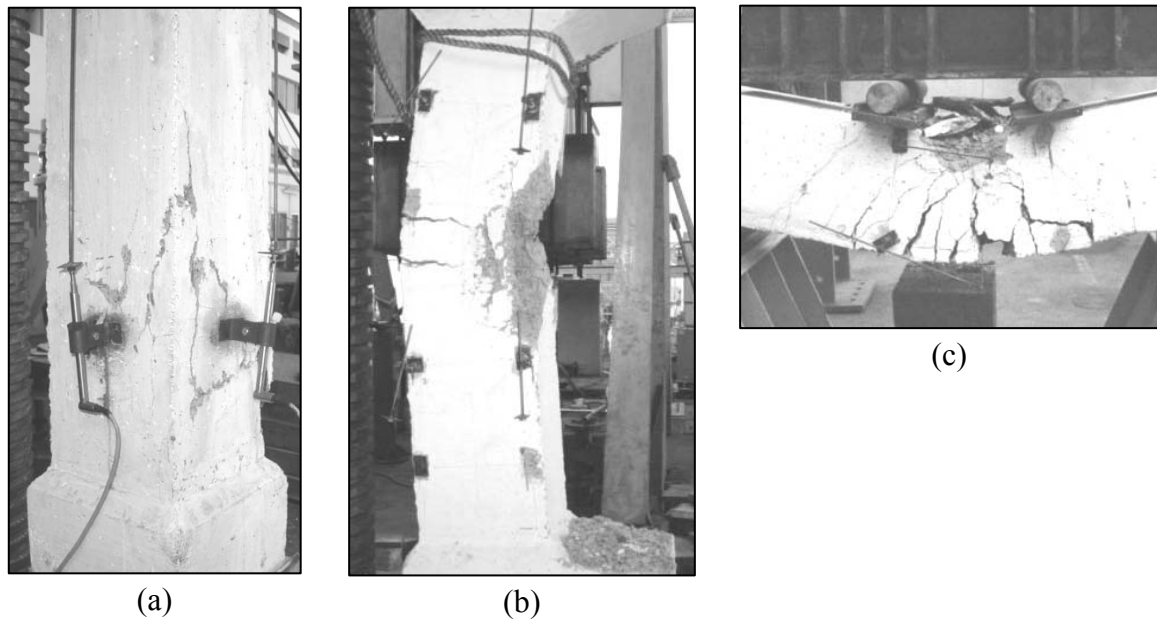


Fig. 10 Photographs of retrofitted specimens after (typical) testing: (a) pure compression, (b) eccentric compression, (c) pure bending

The axial load versus strain curves for typical reference and retrofitted specimens under pure compression and eccentric compression are compared in Figure 11. The increase in axial load capacities of the retrofitted specimens can be observed in this figure. The moment versus curvature curves for typical reference and retrofitted specimens under eccentric compression and pure bending are compared in Figure 12. These plots show an increase in the moment capacities of the retrofitted specimens with respect to the reference specimens.

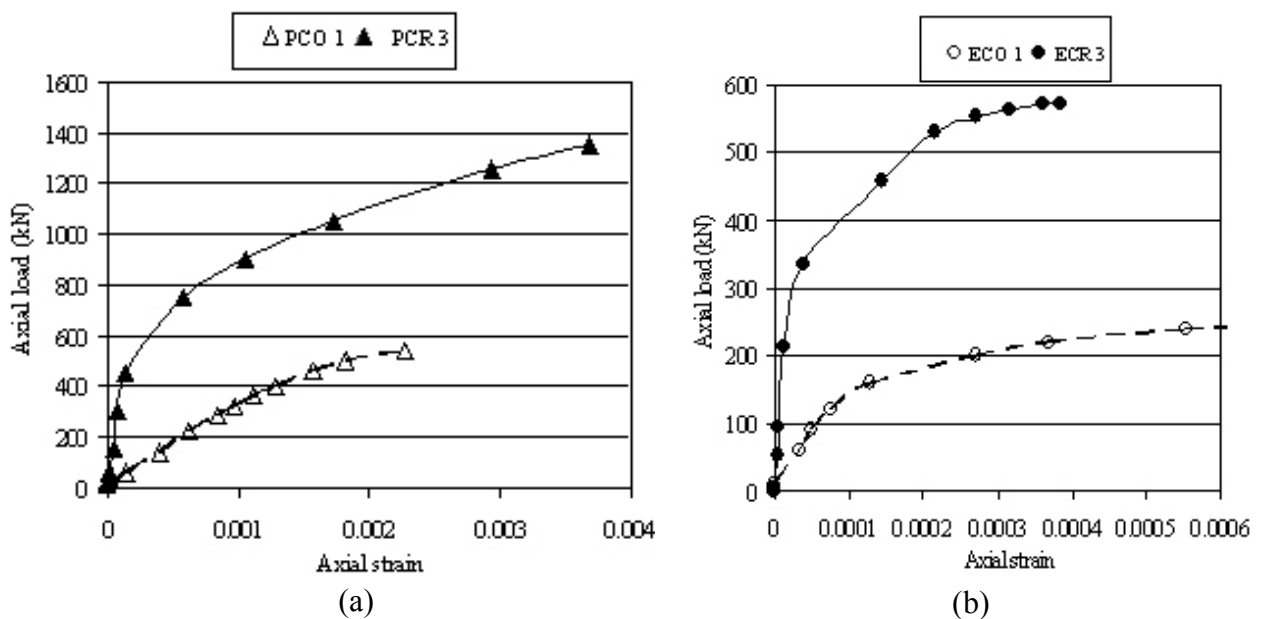


Fig. 11 Axial load versus strain curves for reference (PCO 1 and ECO 1) and retrofitted (PCR 3 and ECR 3) specimens under (a) pure compression and (b) eccentric compression

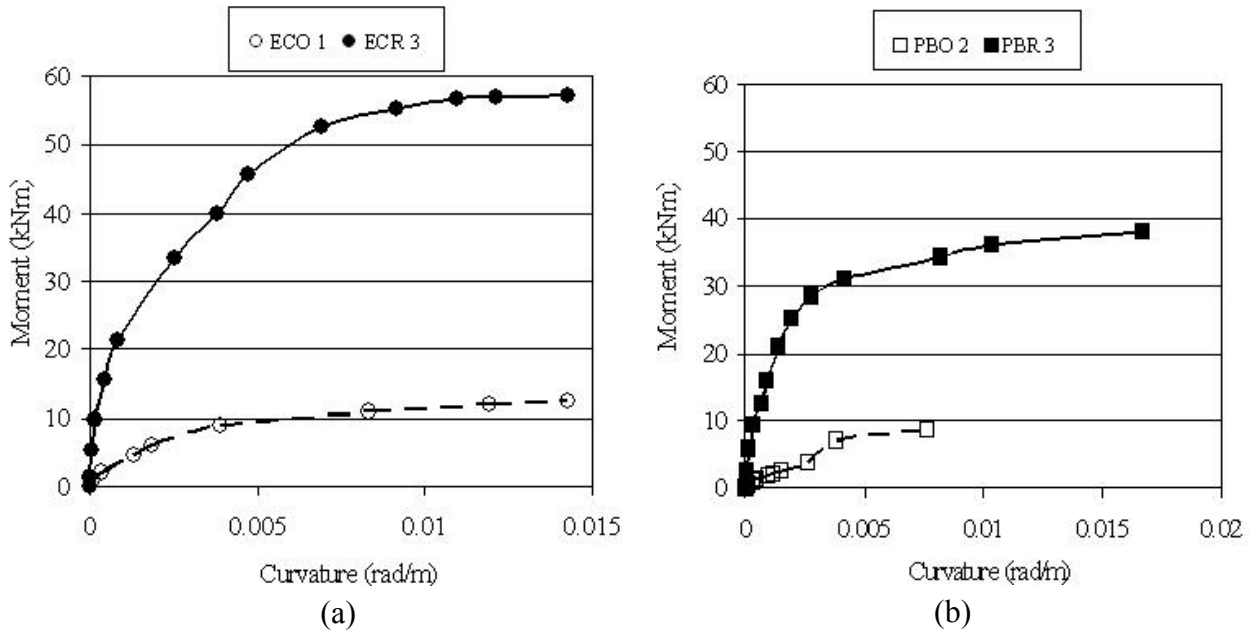


Fig. 12 Moment versus curvature curves for reference (ECO 1 and PBO 2) and retrofitted (ECR 3 and PBR 3) specimens under (a) eccentric compression and (b) pure bending

### 3.3 Interaction Plots

The failure load for each specimen is plotted in Figure 13. In the interaction plot, the vertical and horizontal axes represent the axial load and moment capacities, respectively. It may be observed that there was a substantial increase in the strength after the retrofitting of the sections.

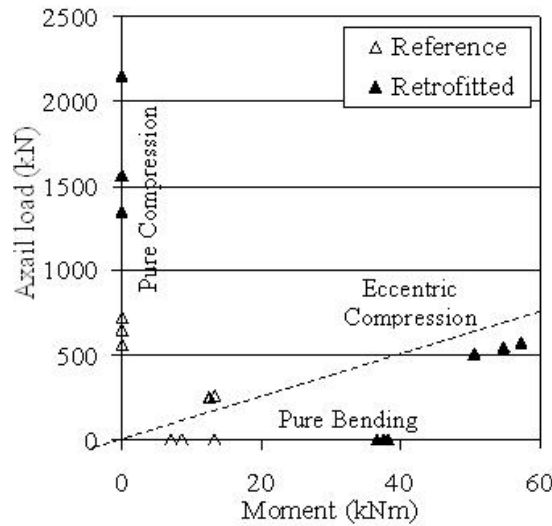


Fig. 13 Interaction plot of failure loads

### TESTS OF BEAM-COLUMN-JOINT SUB-ASSEMBLAGES

To have an appropriate specimen for studying the effect of retrofitting, it is necessary to understand the actions of external loads on the components of a building. In a multistoreyed frame under lateral loading, the points of contraflexure lie approximately at the centres of the beams and columns (see Figure 14). The simulation of this condition for an interior component can be done by testing a beam-column-joint sub-assembly under a lateral (i.e., horizontal) load  $P_H$  as shown in Figure 14(c). To consider the gravity load in the column, a simultaneous vertical load  $P_V$  needs to be applied. The bending

moment diagram for the sub-assembly is shown in Figure 14(d). The additional moments due to the lateral displacement of the applied vertical load (i.e., due to the P-Δ effect) are not shown. The total length and the total height of the sub-assembly are represented as  $L$  and  $H$ , respectively.

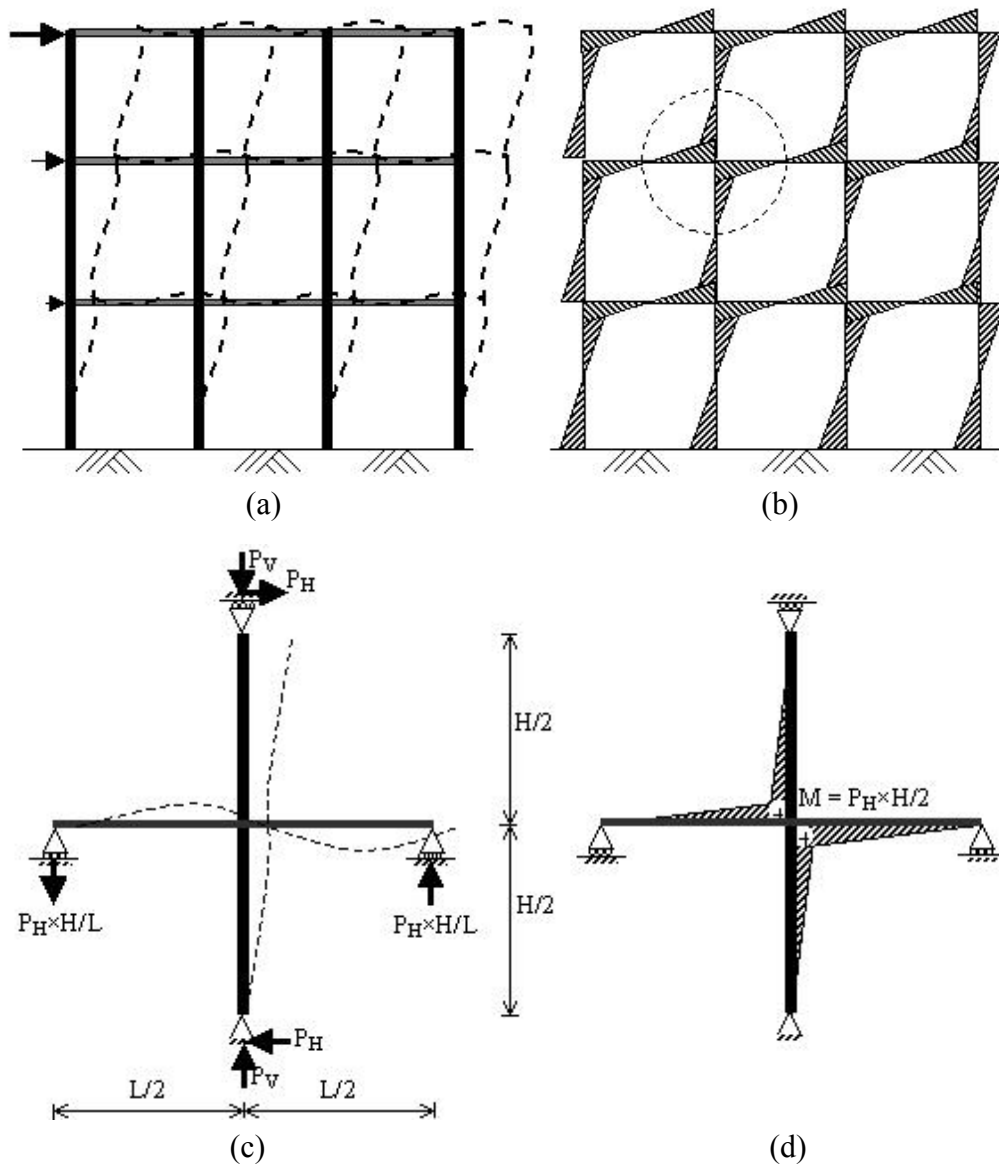


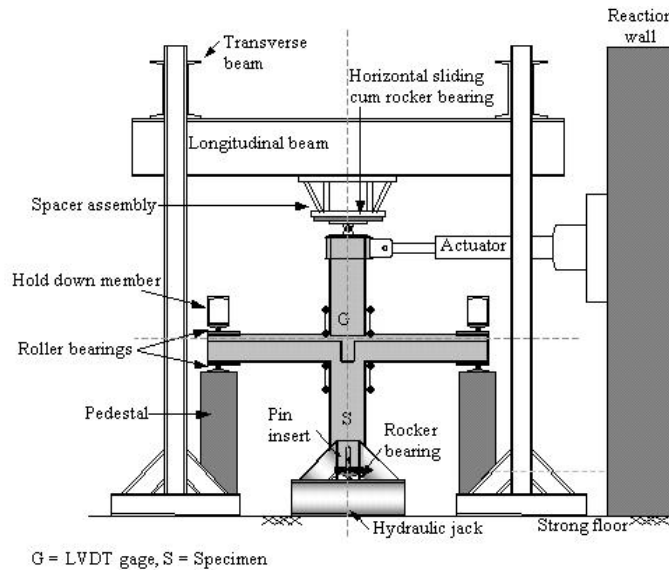
Fig. 14 Loading and bending moment diagrams for a frame and a beam-column-joint sub-assembly: (a) moment-resisting frame under lateral load, (b) bending moment diagram for frame, (c) sub-assembly, (d) bending moment diagram for sub-assembly

### 1. Test Facility

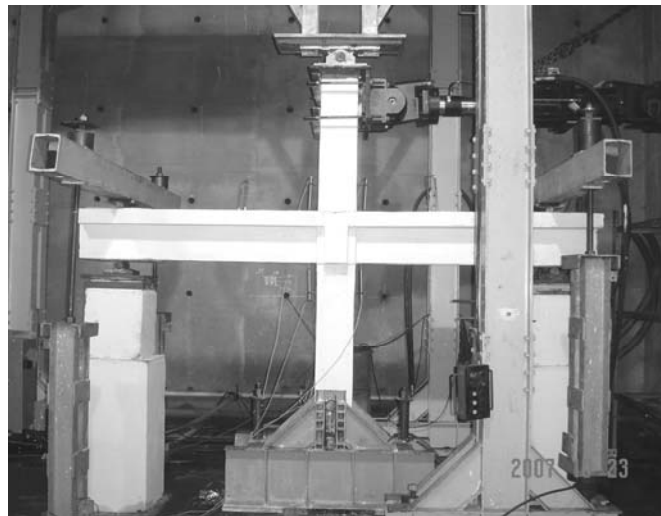
The sub-assembly specimens were tested by using a recently developed test facility. The facility consisted of a reaction wall, a strong floor, and a test frame. The frame was designed and fabricated under the present study. The frame was also used to test the column specimens under pure bending as mentioned in the previous section. The details of the setup for testing the sub-assembly specimens are shown in Figure 15. The top end of the upper column was attached to the frame through a spacer assembly and a horizontal sliding-cum-rocker bearing. This allowed the top end to rotate and translate horizontally. The lateral load was applied at this end by a servo-controlled actuator fitted to the reaction wall.

A rocker bearing was kept at the bottom end of the column. A vertical load of 130 kN was applied on the column, which approximates the axial load corresponding to the balanced failure of the reference column section. The vertical load was applied at the bottom end by a hydraulic jack. An assembly was provided at the bottom end to place the jack. It had a vertical slot through which the pin insert at the

bottom end of the column could slide. This allowed the bottom end to rotate and to translate vertically. The ends of the beams were supported on pedestals. By providing roller-cum-rocker bearings, these ends were allowed to translate horizontally and to rotate. The hold-down steel members prevented any uplift of the ends of the beams. The details of the test facility are provided in Gnanasekaran (2009).



(a)



(b)

Fig. 15 Setup for testing beam-column-joint sub-assemblages: (a) schematic diagram, (b) photograph of retrofitted specimen

To study the lateral load versus displacement behaviour, two reference and two retrofitted specimens were tested. For each type, one specimen was tested under monotonic lateral load and the other under cyclic lateral load. The displacement-controlled cyclic load history is shown in Figure 16. At each displacement level, three cycles of loading were applied. The increment  $\Delta_y$  in the displacement levels was taken same as the theoretical displacement corresponding to the yielding of the outer column bars.

## 2. Specimen Details

The objective of the present study is to investigate the effect of jacketing on the flexural strength of columns in an interior frame. Hence, failures of the beams, and shear failures of the columns or the joints were deliberately avoided. The total length and total height of each specimen were 2.5 and 3.0 m, respectively. Stub beams in the transverse direction and slab over the beams were provided to create

obstructions in placing the additional longitudinal bars in the column jacket, like in an interior frame of an existing building. Of course, the slab has a stiffening effect on the main beams.

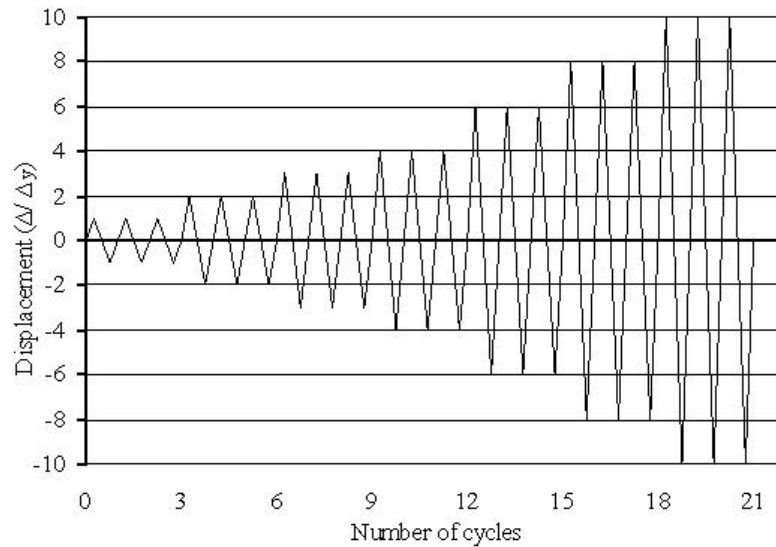


Fig. 16 Cyclic loading history

### 2.1 Reference Specimens

The details of the specimens are shown in Figure 17. Table 4 provides the material properties for the specimens. A concrete mix of 1:3.4:3.8 (cement: fine aggregate: coarse aggregate) with water-to-cement ratio of 0.75 was used. To avoid failure of the beams prior to that of the columns, both positive and negative yield moments of the beams were kept at least 10 percent higher than the target flexural capacity of the retrofitted columns. The members had adequate shear reinforcement to avoid any shear failure. Further, ties were provided in the joints to avoid any failure of the joints.

### 2.2 Retrofitted Specimens

The details of the specimens are shown in Figure 18. The fabrication of the reinforcement for the jacket is illustrated in Figure 19. The additional longitudinal bars were placed at the corners of the existing column. To continue the added bars, holes were drilled in the slab. Additional ties were not placed at the joint to avoid drilling of the beams. To stiffen the bars against buckling and to confine the joint region, angles were welded to the additional longitudinal bars at the joint. To minimize any reduction of ductility due to welding, bars from a reputed producer were used. To check the integrity of the welds, coupon specimens of bars with welded angles were tested under tension, and the necking and subsequent failure of the bars were found to be away from the welded segments. To enhance the integrity of the angles, those were tied together above the floor level and beneath the soffits of the beams with 10-mm diameter threaded bolts (see Figure 19(b)).

Each transverse bar for the jacket was made of two lapped U-bars. One of the U-bars was provided with 90° bends for additional lapping. The specimens were cast vertically to simulate the actual method of construction. The jackets of the retrofitted specimens were made of self-compacting concrete, as was done for the retrofitted column specimens.

## 3. Test Results

### 3.1 Reference Specimens

For the specimen tested under monotonic lateral loading, a plastic hinge was formed at the bottom column near the joint, followed by the buckling of longitudinal bars. For the specimen tested under cyclic lateral loading, plastic hinges were formed at both top and bottom columns near the joint, followed by the buckling of the longitudinal bars of the bottom column. The close-up views of the plastic hinges are shown in Figure 20. There was no distress in the beams or in the joints. The specimen showed stable hysteresis loops with the ultimate strength being reached at the 21st cycle.

3.2 Retrofitted Specimens

The columns in the retrofitted specimens were found to behave satisfactorily with regard to strength and ductility, without any premature failure, such as buckling of the additional longitudinal bars at the joint. There was no distress in the beams or in the joints. There was no shear crack in the columns. From this it can be inferred that the added ties made of U-bars were adequate in the present study. The close-up views of the plastic hinges in the columns for the specimen tested under cyclic lateral loading are shown in Figure 21.

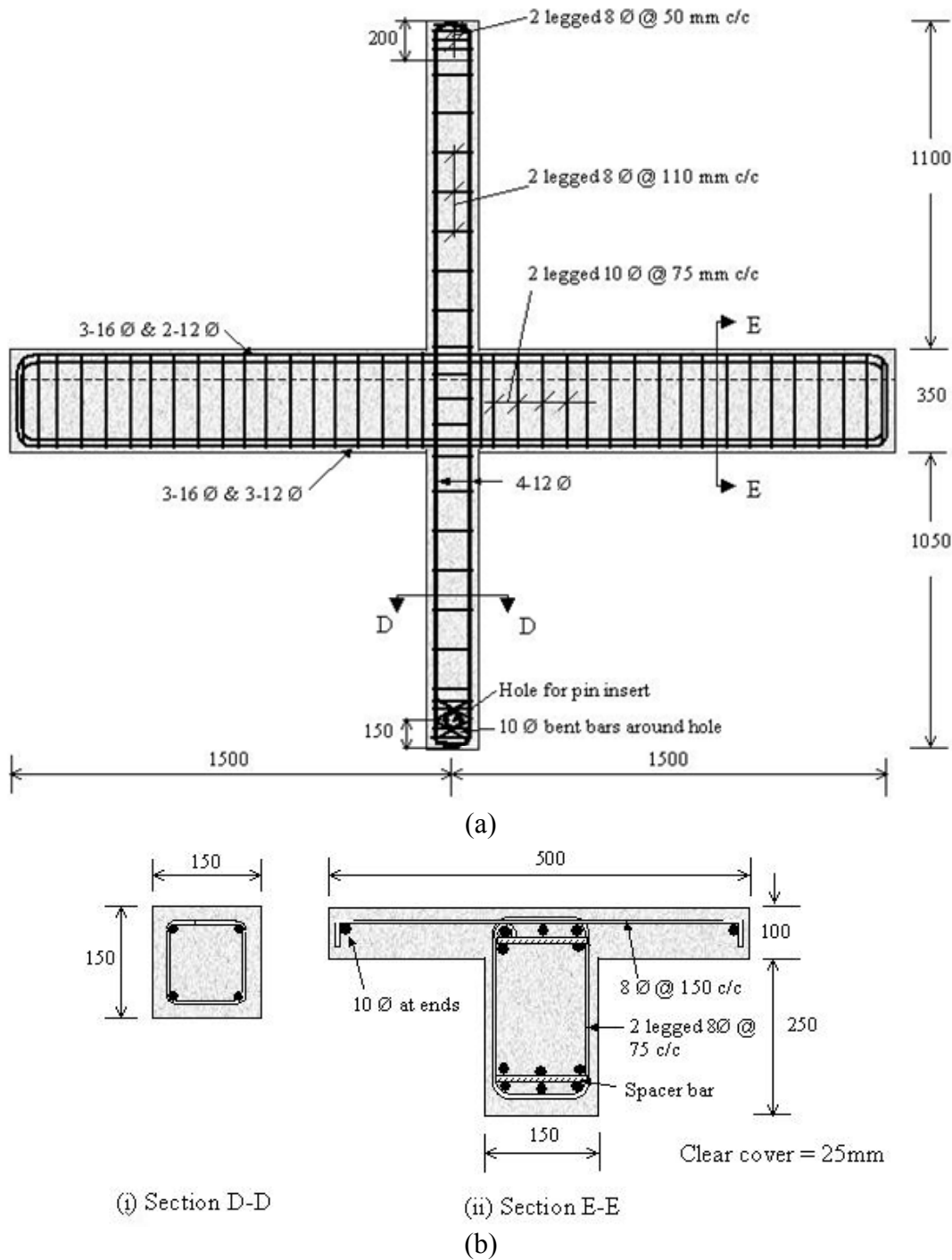


Fig. 17 Details of the reference specimen for beam-column-joint sub-assembly tests (all dimensions are in mm): (a) reinforcement details for reference members, (b) cross-sections of members (not to scale)

**Table 4: Material Properties for Sub-assembly Specimens**

Type of Lateral Loading	Reference			Retrofitted			
	$f_{cm}$	$f_{yl}$	$f_{yt}$	$f_{cmE}$	$f_{cmJ}$	$f_{yl}$	$f_{yt}$
Monotonic	24	435	468	22	31	483	504
Cyclic				24	32		

$f_{cm}$  = mean cube strength of concrete (in MPa),  $f_{cmE}$  = mean cube strength of existing concrete (in MPa),  $f_{cmJ}$  = mean cube strength of jacket concrete (in MPa),  $f_{yl}$  = yield strength of longitudinal bars in the columns (in MPa),  $f_{yt}$  = yield strength of transverse bars in the columns (in MPa), modulus of elasticity for steel =  $2.02 \times 10^5$  N/mm<sup>2</sup>

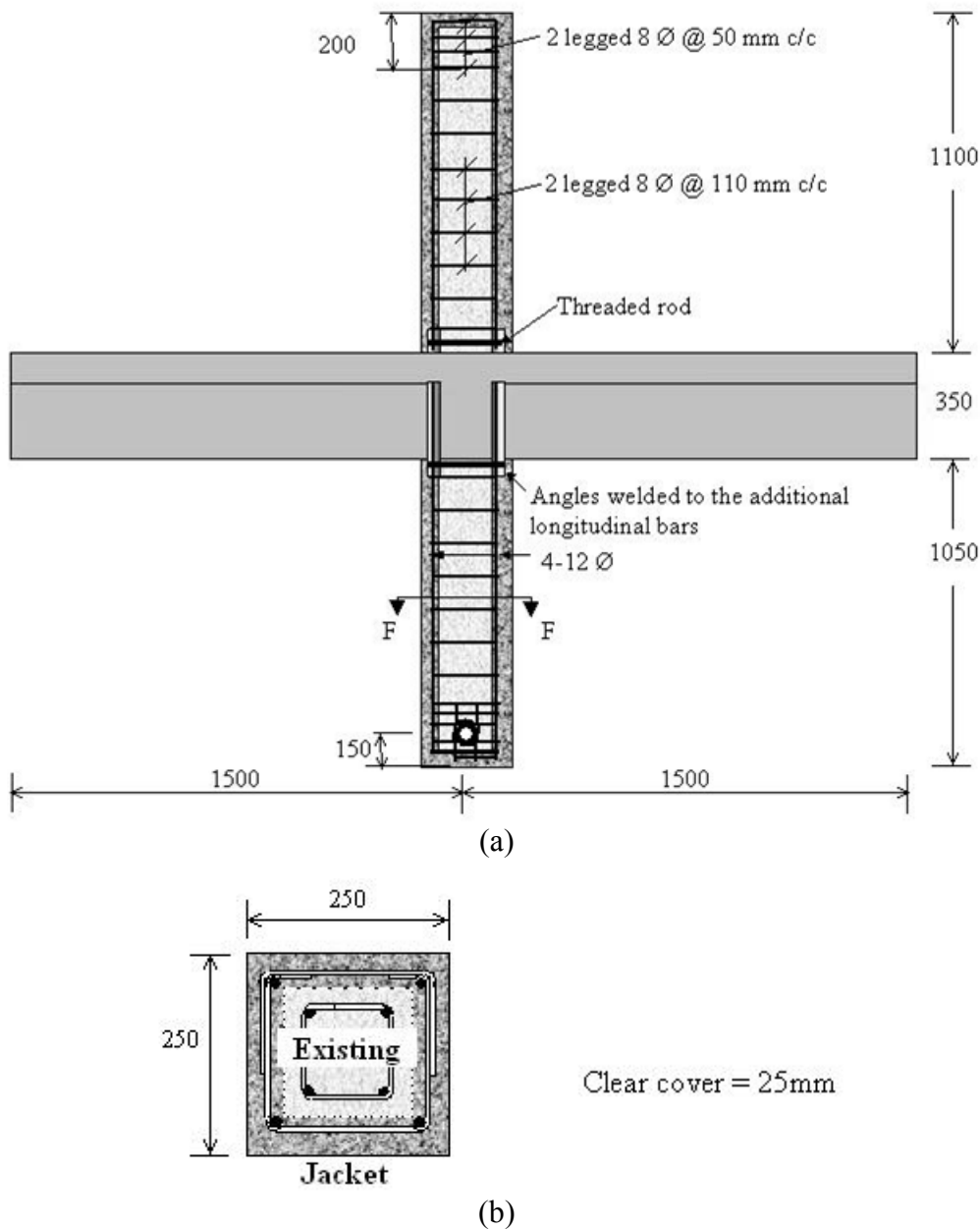


Fig. 18 Details of the retrofitted specimen for beam-column-joint sub-assembly tests (all dimensions are in mm): (a) reinforcement details for retrofitted column, (b) Section F-F (not to scale) (these bars are in addition to those in the original cross-sections, which are same as in the reference specimen; see Figure 17)

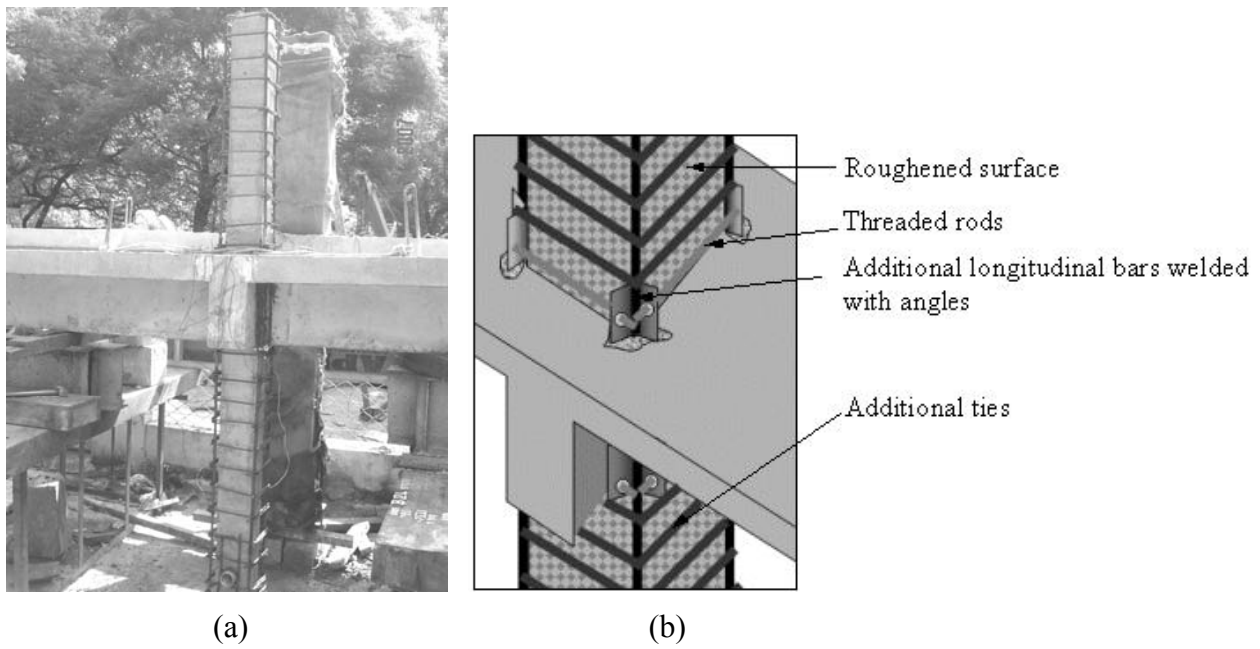


Fig. 19 Fabrication of reinforcement for retrofitted specimens: (a) photograph of fabricated reinforcement, (b) details at the beam-to-column joint

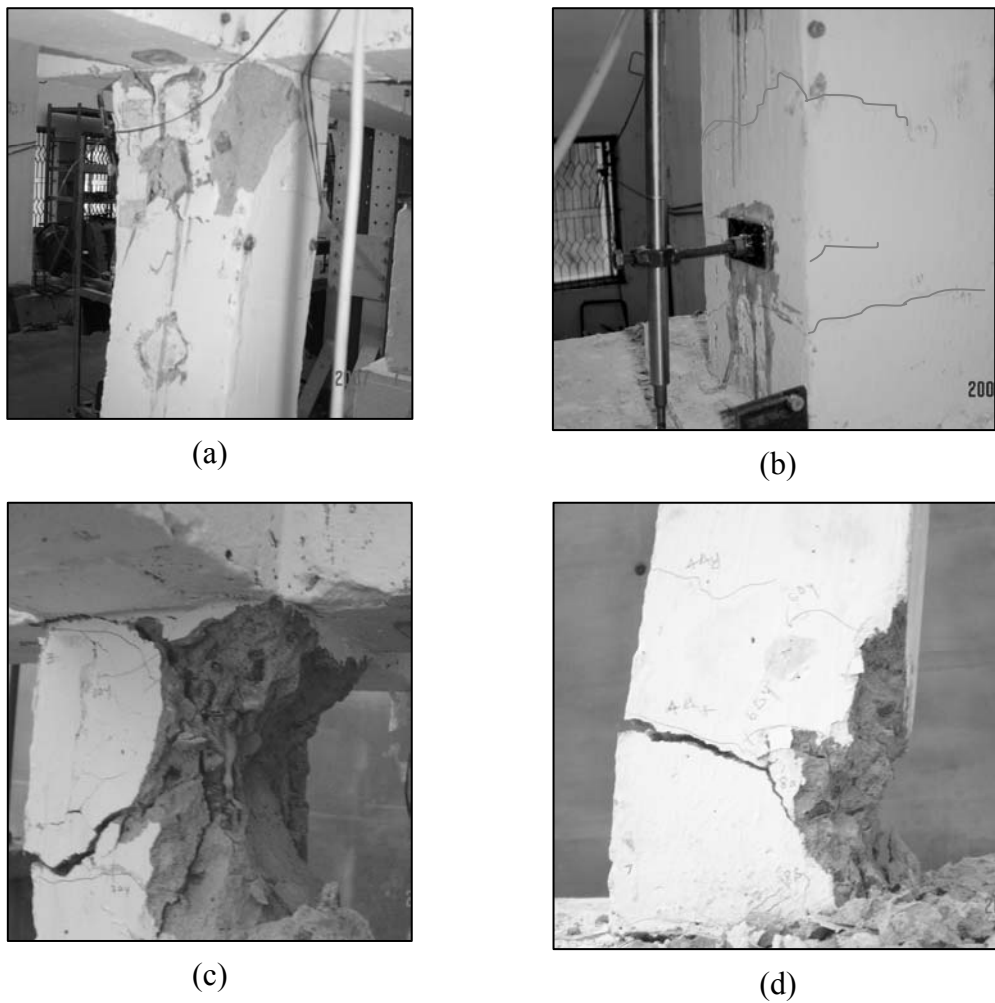


Fig. 20 Reference specimens after testing: (a) bottom column under monotonic loading, (b) top column under monotonic loading, (c) bottom column under cyclic loading, (d) top column under cyclic loading

The measured lateral load versus displacement curves for the reference and retrofitted specimens tested under the monotonic lateral loading are compared in Figure 22. It may be observed that the lateral strength (equal to the maximum lateral load sustained) and the displacement ductility of the retrofitted specimen have improved substantially as compared to the reference specimen. The corresponding measured moment versus curvature curves for the hinges are shown in Figure 23.

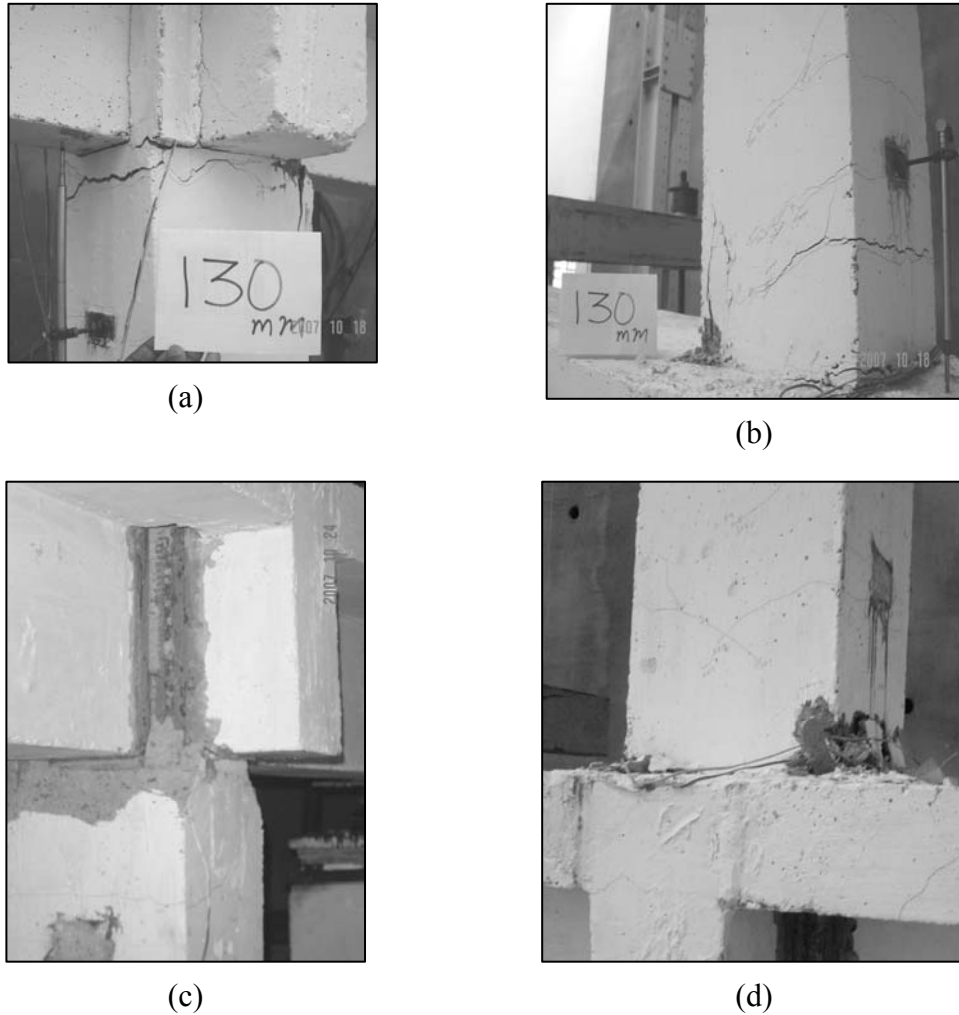


Fig. 21 Retrofitted specimens after testing: (a) bottom column under monotonic loading, (b) top column under monotonic loading, (c) bottom column under cyclic loading, (d) top column under cyclic loading

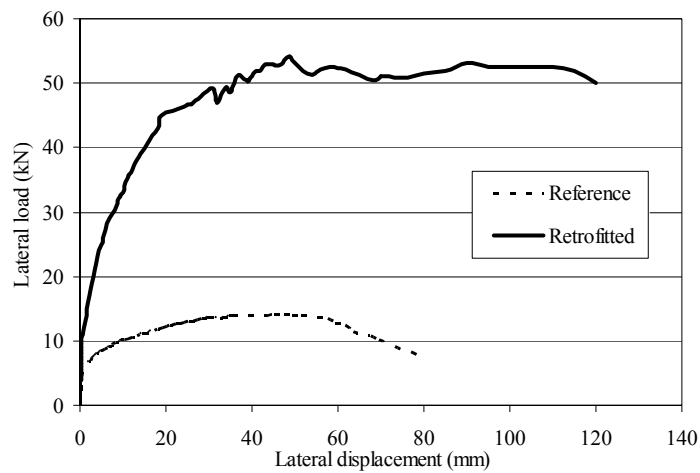


Fig. 22 Comparison of the lateral load versus displacement curves under monotonic loading

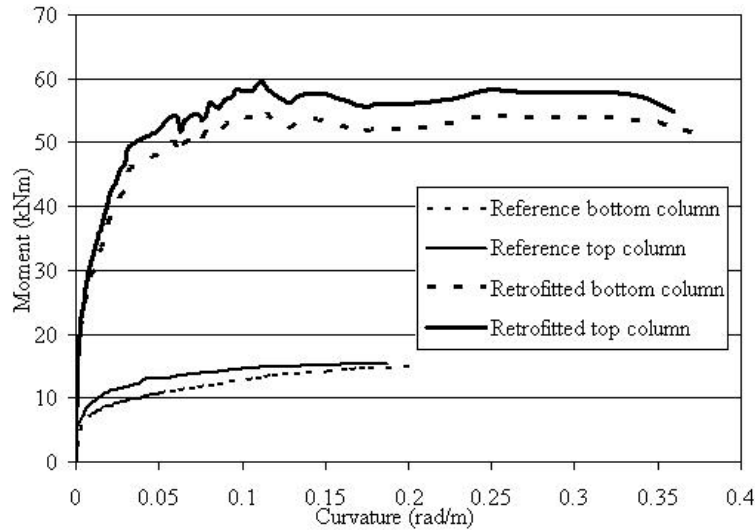


Fig. 23 Comparison of the moment versus curvature curves under monotonic loading

The lateral load versus displacement curves for the reference and retrofitted specimens tested under cyclic lateral loading are compared in Figure 24. The cumulative energy dissipated (based on the areas within the hysteresis loops) in the loading cycles by each of the reference and retrofitted specimens is shown in Figure 25. It may be observed that the energy dissipation has improved substantially due to jacketing.

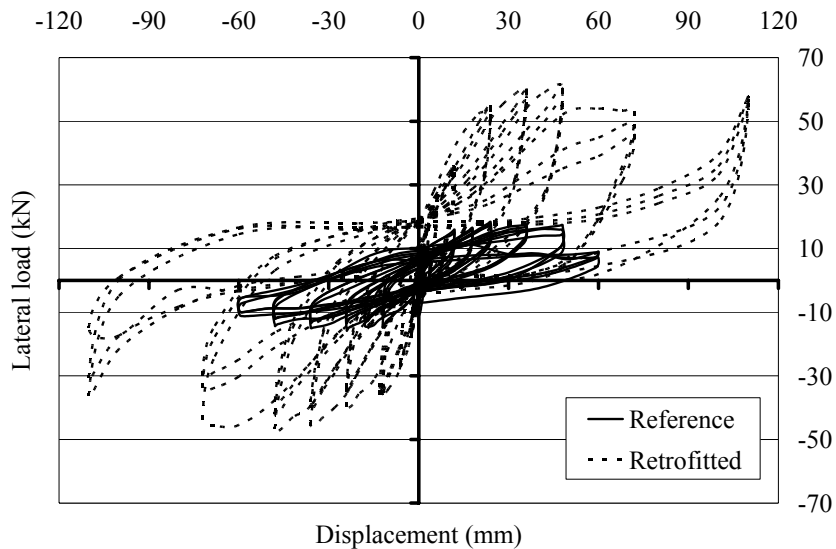


Fig. 24 Comparison of the lateral load versus displacement curves under cyclic loading

**3.3 Comparison of Monotonic and Cyclic Tests**

The lateral load versus displacement curves for the monotonic and cyclic loadings of the reference specimen are shown in Figure 26. The corresponding curves for the retrofitted specimen are shown in Figure 27. For both reference and retrofitted specimens, the monotonic tests provide sufficiently good estimates of the envelope of the lateral load versus displacement curves obtained under the cyclic loading. Hence, the values of ductility calculated from the lateral load versus displacement curves for monotonic loading are rational estimates.

**3.4 Observations**

The values of lateral strength and displacement ductility for the sub-assembly specimens are given in Table 5. The values of lateral strength and lateral displacement for all specimens are compared in Figures 28 and 29, respectively.

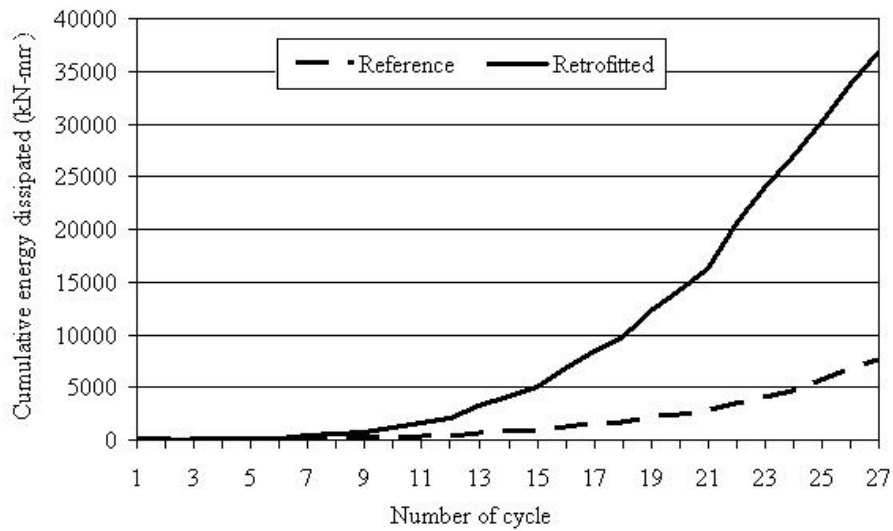


Fig. 25 Comparison of the curves for energy dissipated under cyclic loading

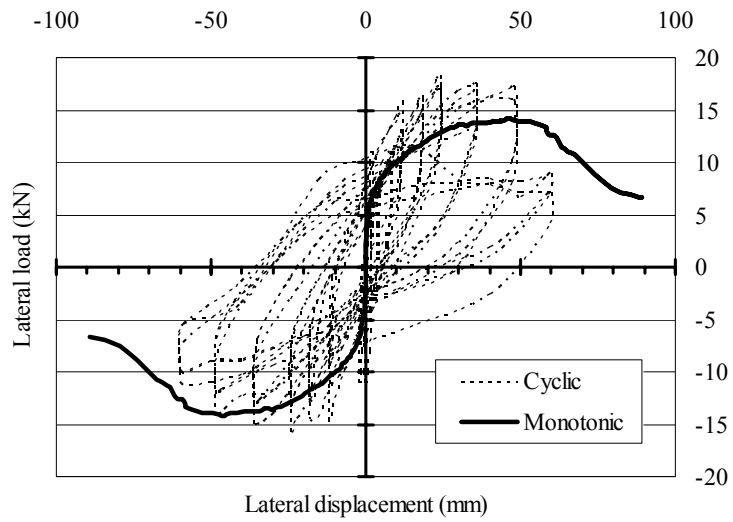


Fig. 26 Comparison of the lateral load versus displacement curves under monotonic and cyclic loadings for reference specimens

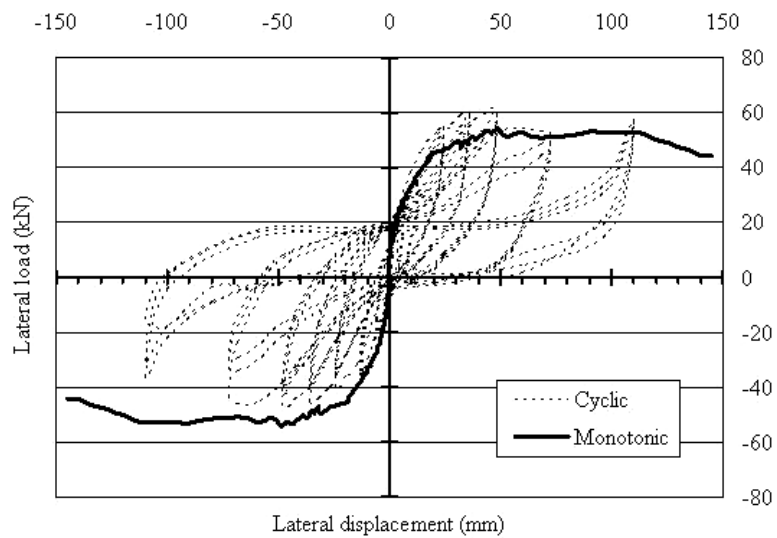


Fig. 27 Comparison of the lateral load versus displacement curves under monotonic and cyclic loadings for retrofitted specimens

**Table 5: Values of Lateral Strength and Ductility for Sub-assembly Specimens**

Type of Lateral Loading	Type of Specimen	Lateral Strength (kN)	Lateral Displacement (mm)		Displacement Ductility $\Delta_u/\Delta_y$	Cumulative Energy Dissipated till 27th Cycle (kN-mm)	
			Yield*	Ultimate†			
			$\Delta_y$	$\Delta_u$			
Monotonic	Reference	14	18	45	2.5	Not applicable	
	Retrofitted	53	24	110	4.6		
Cyclic	Reference	-	14	30	48	1.6	7617
		+	17	24	48	2.0	
	Retrofitted	-	47	22	110	5.0	36944
		+	58	20	110	5.5	

\*Displacement corresponding to a strain of  $f_{yl}/E_{sl} + 0.002$  in the extreme longitudinal bars

†Displacement corresponding to the onset of drop in the applied lateral load

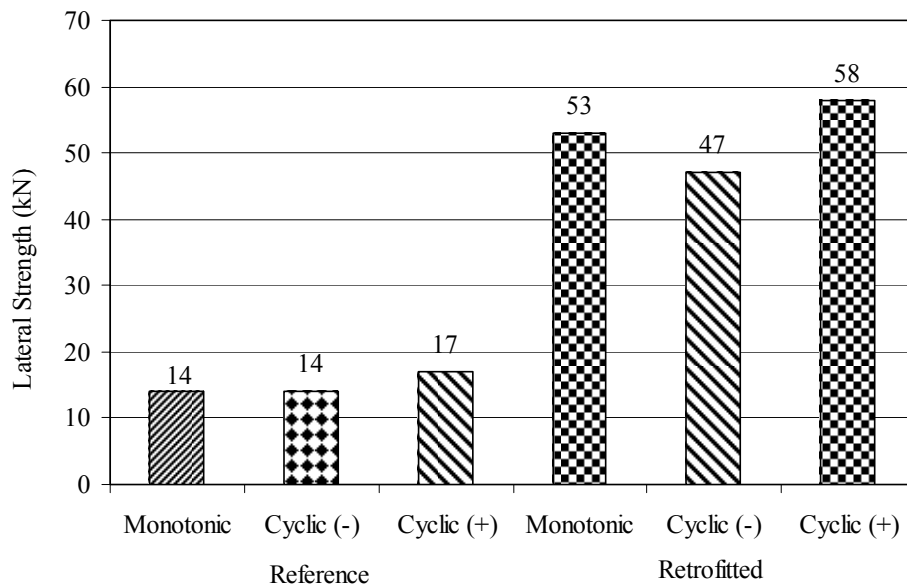


Fig. 28 Comparison of lateral strengths for reference and retrofitted specimens

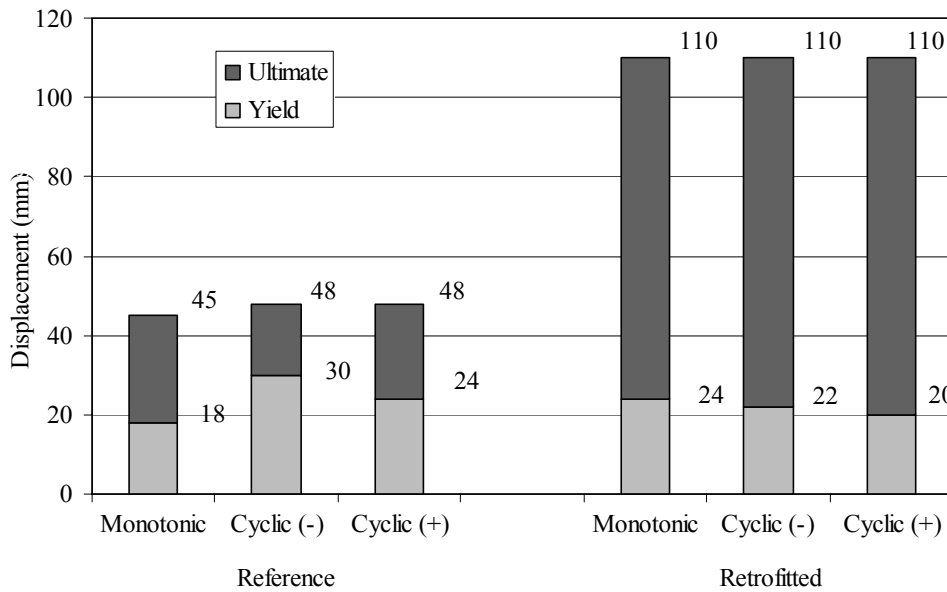


Fig. 29 Comparison of lateral displacements for reference and retrofitted specimens

The observations from the sub-assembly tests are summarized below:

1. The retrofitted specimens did not show any visible delamination of the concrete in the jacket. The delamination was inspected by light tapping of a hammer. The sound due to any gap generated between the concrete layers and any chipping off the jacket concrete would have revealed delamination.
2. (a) The lateral strength of the retrofitted specimen tested under monotonic loading was 3.8 times higher than that of the reference specimen.  
(b) The lateral strengths (for both positive and negative cycles) of the retrofitted specimen tested under cyclic loading were about 3.3 times higher than those of the reference specimen.
3. (a) The displacement ductility of the retrofitted specimen tested under monotonic loading was 1.8 times higher than that of the reference specimen.  
(b) The values of displacement ductility of the retrofitted specimen tested under cyclic loading were 2.8 and 3.1 times higher than those of the reference specimen for the positive and negative cycles, respectively.
4. Under the cyclic loading, the cumulative energy dissipated till attaining the strength for the retrofitted specimen was 4.85 times higher than that for the reference specimen.

## ANALYSIS OF RETROFITTED SECTIONS

The axial load versus moment interaction curves and moment versus curvature curves for the retrofitted sections are predicted by a lamellar (or layered) analysis and a simplified analysis.

### 1. Lamellar Analysis

A retrofitted section is a heterogeneous section with two grades of concrete and several layers of reinforcement bars. To account for the heterogeneity, a lamellar method of analysis was used, wherein the section was divided into layers through the depth. A perfect bond was assumed for strain compatibility between the existing concrete and the jacket. The existing concrete was considered to be confined by the closely spaced added ties in the jacket. Among the available stress versus strain models for confined concrete, the model proposed by Mander et al. (1988) for confined concrete was selected. A parabolic and plastic stress versus strain model was used for the unconfined concrete of the jacket. The possible tension stiffening by the concrete in between the cracks prior to the yielding of the longitudinal bars was not considered in the sectional analysis.

### 2. Simplified Analysis

This analysis is preferred in the professional practice. This was conducted based on a uniform compressive strength (equal to that of the existing concrete) throughout the section. The stress versus strain curve as given in IS 456 (BIS, 2000) was used for the homogeneous concrete.

### 3. Results for Axial Load versus Flexural Strength Curves

The axial load versus moment interaction curves for the column specimens were developed by both of the above methods of analysis while satisfying the equilibrium conditions of axial force and moment at a section. The depth of neutral axis was varied to get a set of axial load and moment values. The material safety factors for steel and concrete were not considered.

Figure 30 shows comparison of the axial load versus moment interaction plots of the retrofitted columns as obtained from the tests and the predictions. The lamellar analysis shows good predictions of the strengths, except for Specimens PCR 1 and ECR 2. As mentioned earlier, these specimens had premature failures outside the test regions.

The simplified analysis provides lower strengths as compared to the tests, except for Specimens ECR 1, ECR 2, and ECR 3. Since a lower grade of concrete was used in determining the strength of a section, the predicted strength is expected to be lower than the experimental value. For Specimens ECR 1, ECR 2 and ECR 3, the compressive strength  $f_{cmE}$  of the existing concrete turned out to be more than the compressive strength  $f_{cmJ}$  of the concrete in the jackets because of the different periods of curing and trial mixes of the self-compacting concrete. The use of the compressive strength  $f_{cmE}$  of the existing concrete throughout the sections led to an overestimation of the strengths.

**4. Results for Moment versus Curvature Behaviour**

The moment versus curvature curves for the columns in the sub-assembly specimens were developed by both lamellar and simplified analyses. The compressive strain in the extreme fibre of a section was varied to get a set of moment and curvature values. For the lamellar analysis, the failure strain for the concrete in the jacket was taken equal to the value measured from the test. For the simplified analysis, the corresponding failure strain was taken as 0.0035, as per IS 456 (BIS, 2000). The curves for the column section of the retrofitted sub-assembly tested under the monotonic loading are shown in Figure 31. It may be observed that the lamellar analysis provides good prediction of the behaviour. The simplified analysis underestimates the strength, as the grade of the inner concrete was considered to be applicable throughout the section and the effect of confinement was neglected. Also, the analysis cannot predict the deformation beyond a certain value due to the limiting strain of 0.0035.

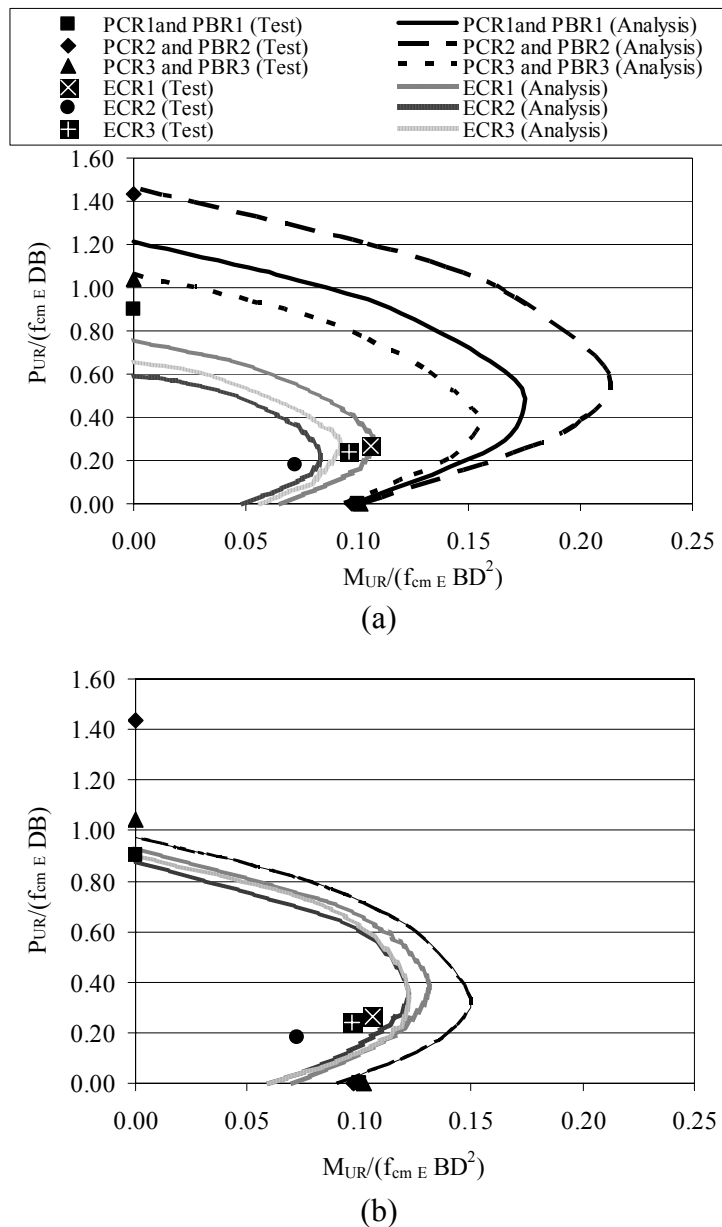


Fig. 30 Axial load versus moment interaction plots for retrofitted columns based on (a) lamellar analysis and (b) simplified analysis

**5. Results for Lateral Load versus Displacement Behaviour**

The lateral load versus displacement curve for the retrofitted specimen tested under monotonic lateral loading is predicted by a computational model of the sub-assembly. Initially, a pushover analysis as per

the software SAP 2000 NL was conducted. However, it was observed that the nonlinearity in the behaviour could not be predicted with sufficient accuracy by assigning the limited bilinear form (up to the peak) to the moment versus rotation hinge property. Next, an incremental nonlinear analysis was conducted with varying rotational stiffness for the plastic hinge regions of the columns. Only the latter analysis is presented here for brevity.

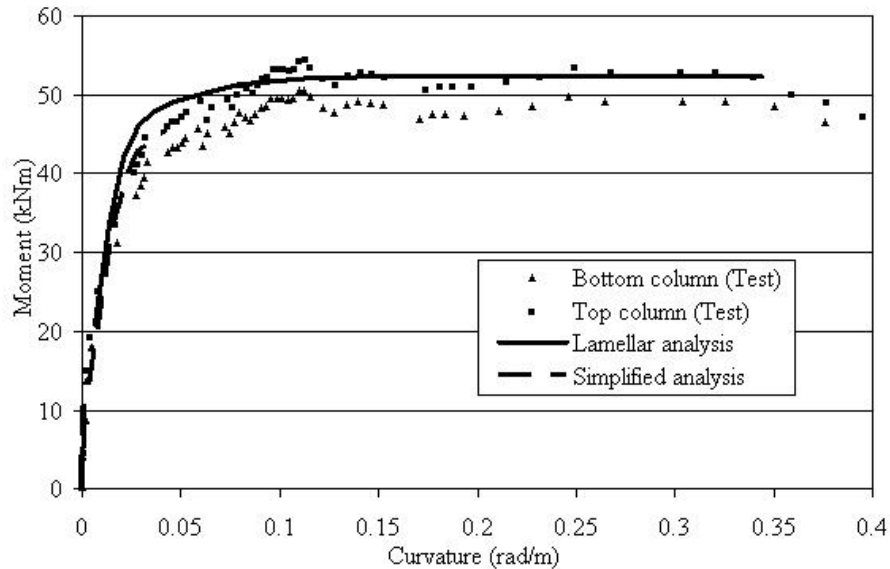


Fig. 31 Moment versus curvature curves for the retrofitted column section tested under monotonic loading

The computational model for the sub-assembly developed using frame elements and appropriate boundary conditions is shown in Figure 32. To consider the spread plasticity, the top and bottom column members were sub-divided for isolating the plastic hinge regions of height  $0.5D$  (where  $D$  is the overall depth of the column) from the faces of the joint. At each step  $P_{Hi}$  of the lateral load, the flexural stiffness, based on the predicted moment versus curvature values from a lamellar analysis of the column section, was assigned to each plastic hinge member. From the bending moment  $M_i$  (corresponding to  $P_{Hi}$ ) in the column at the face of the joint, the moment of inertia  $I_i$  for a plastic hinge member was calculated based on the secant flexural stiffness  $E_c I_i$  of the predicted moment versus curvature curve (see Figure 33), where  $E_c$  is the modulus of concrete. Thus,  $I_i = M_i / \phi_i E_c$ , where  $\phi_i$  is the curvature corresponding to  $M_i$ . Next, a linear analysis was performed to get the lateral displacement  $\Delta_i$  at the top of the upper column due to  $P_{Hi}$ . The P- $\Delta$  effect due to the displacement of the vertical load  $P_V$  at the top of the upper column was included. The analysis was conducted for incremental values of  $P_{Hi}$ .

In the experiments, horizontal frictional forces were induced at the bearings at the ends of the beams and at the top of the upper column due to reactions from the axial load. These frictional forces increased the stiffness of the experimental lateral load versus displacement curve. For a precise prediction of the behaviour, it was decided to include the frictional forces in the computational model. First, the bearings were tested to determine their coefficients of friction. From the tests, it was found that the roller-cum-rocker bearings at the beam ends had a coefficient of friction,  $\mu_r$ , equal to 0.11. The coefficient of friction,  $\mu_s$ , for the sliding-cum-rocker bearing at the top of the column was 0.035. Next, frictional force at a bearing was calculated by multiplying the vertical reaction at the bearing, corresponding to a load step, with the coefficient of friction. The value of each vertical reaction was calculated from statics due to  $P_V$  or  $P_H$  or both.

In Figure 32, the horizontal frictional forces at the beam ends and at the top of the column are denoted as  $R_{F,A}$ ,  $R_{F,B}$ , and  $R_{F,C}$ , respectively. The corresponding vertical reactions are denoted as  $R_A$ ,  $R_B$ , and

$R_C$ , respectively. Additional forces corresponding to  $R_{F,A}$  and  $R_{F,B}$  were applied in the computational model to incorporate the effect of friction in the bearings at the beam ends. The value of  $R_{F,C}$  was deducted from the applied  $P_H$  to incorporate the effect of friction in the bearing at the top of the upper column.

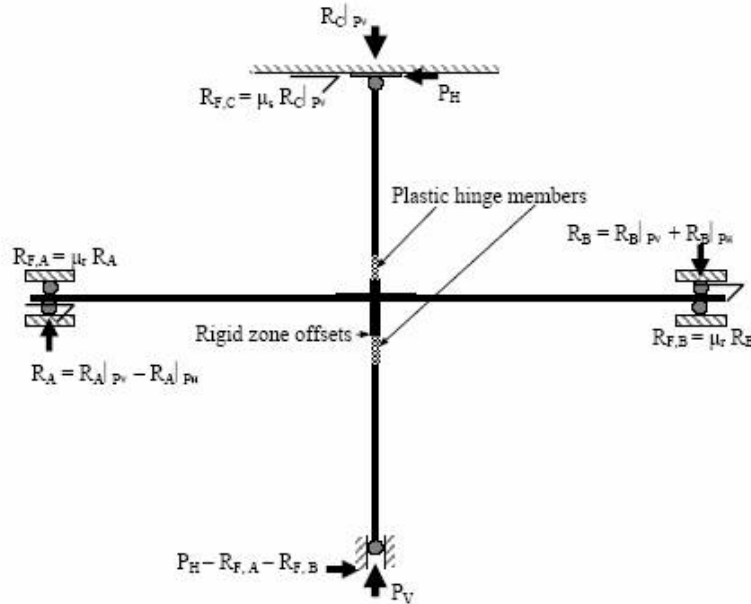


Fig. 32 Computational model for beam-column-joint sub-assembly

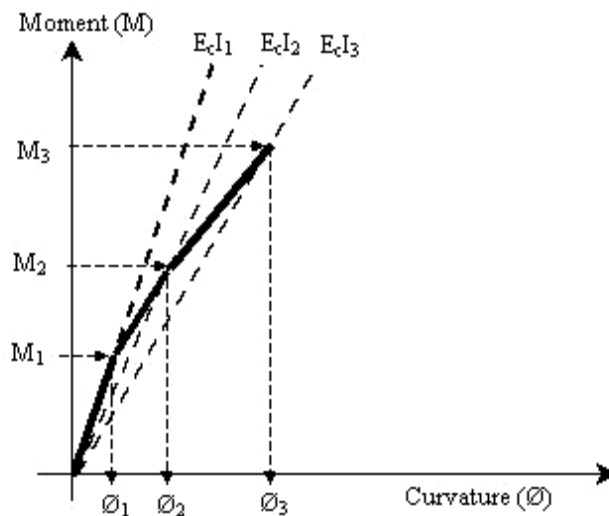


Fig. 33 Secant flexural stiffness from moment versus curvature curve

From the incremental nonlinear analysis, the predicted lateral load versus displacement curve for the retrofitted specimen tested under the monotonic lateral loading is plotted in Figure 34. It may be observed that the predicted curve is close to the experimental results.

**GUIDELINES FOR PROFESSIONAL PRACTICE**

**1. Analysis of Retrofitted Sections**

A lamellar analysis can be adopted for a retrofitted section considering different strengths and behaviour of the existing concrete and the concrete in the jacket. A preloaded section can be analyzed by considering initial strain in the existing section. On neglecting slippage, the strain difference at the

interface of the two concretes should be maintained to satisfy the strain compatibility. A simplified analysis considering a uniform compressive strength (equal to that of the lower grade concrete) throughout the section can be adopted for quick calculations.

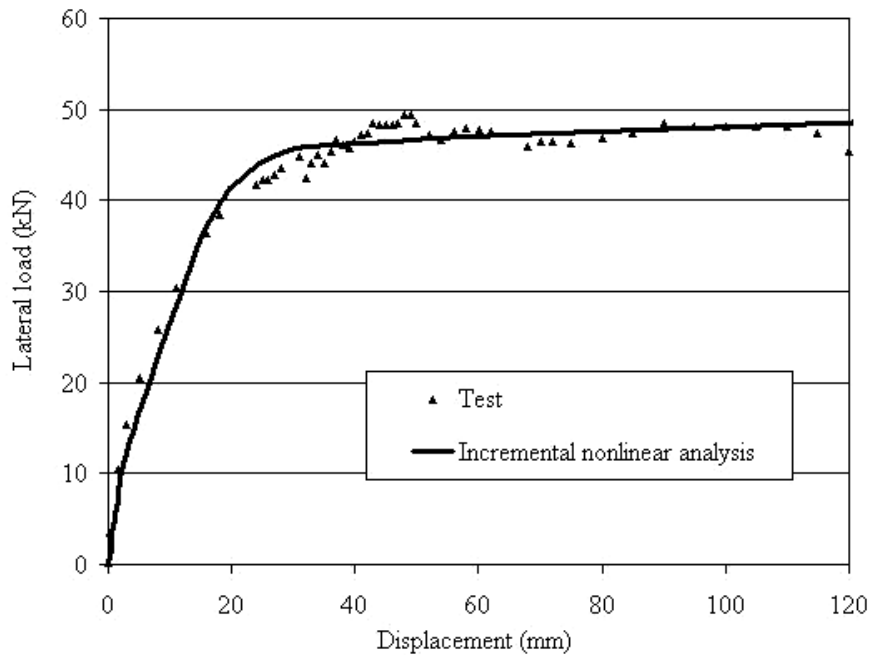


Fig. 34 Lateral load versus displacement curves for the retrofitted sub-assembly tested under monotonic loading

## 2. Design of Additional Bars

The required additional longitudinal bars for a column are to be calculated based on the moment demand from the worst combination of gravity and seismic loads.

The additional ties are to be calculated based on the shear demand from the capacity-based design and the requirement of confinement (BIS, 1993).

## 3. Detailing

To avoid any damage to the primary frame members of poor concrete, drilling of holes should be minimized in selecting a scheme of reinforcement for the concrete jacket. The additional longitudinal bars can be placed near the corners of a joint. This will avoid drilling holes through the beams. The bars should continue through the holes drilled in the intermediate floor slabs and be anchored into the footing. A minimum cover should be provided as per IS 456 (BIS, 2000) to satisfy the fire safety and durability requirements.

Additional ties for the jacket should be closely spaced in the plastic hinge regions, as per the ductile detailing requirements of IS 13920 (BIS, 1993). The ties should be provided preferably with 135° end-hooks, if the thickness of the jacket is large. Else, the ties can be made of U-bars with adequate lap length or welded lap. Of course, additional tests are required with the shear-dominated behaviour of the columns in order to study the performance of the U-bars.

When a joint in the existing building does not have any ties, additional ties may be provided to increase the shear capacity of the joint. However, this involves drilling of the supported beams. Alternatively, to enhance the confinement of concrete at a joint, angles or cruciform sections can be provided at the corners of the joint and properly tied with threaded rods at the top and bottom of the joint. Following are some recommendations for this scheme:

- The surfaces of the angles or the cruciform sections should be roughened by using scribers, for better bond with the concrete surface.
- The additional longitudinal bars should be welded or clamped to the angles/cruciform sections by using steel loops at frequent intervals. For welding, weldable bars with adequate ductility should be

used. Also, the quality control specifications regarding selection of electrodes and workmanship should be adhered to.

Two typical interior joints are shown in Figure 35. The cross-sectional details near the joints are illustrated in Figure 36.

For a column wider than 300 mm, distributed longitudinal bars along the surfaces should be provided. These bars are not continuous at the joint. However, they should be tied to the added ties and provided with end hooks. This tying of bars will also reduce the unsupported lengths of the added ties.

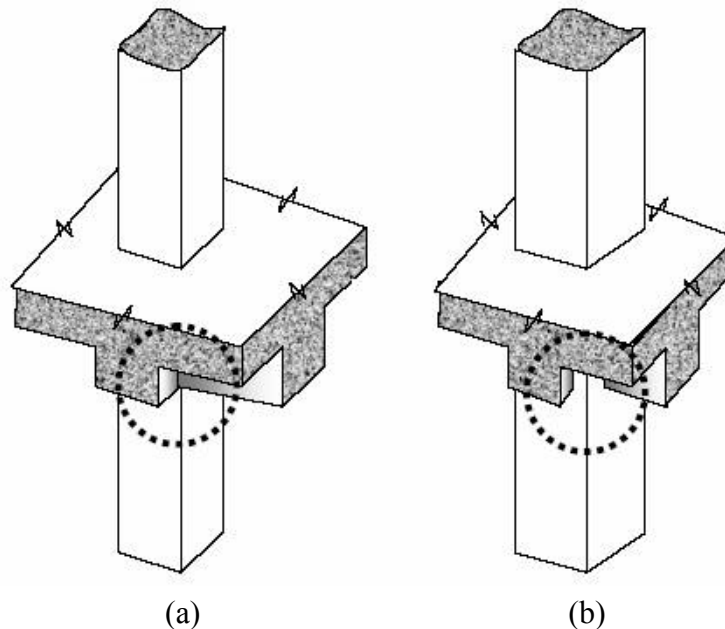


Fig. 35 Typical interior beam-to-column joints (the reinforcement bars are not shown): (a) width of column same as that of beams, (b) width of column larger than that of beams

#### 4. Construction

If possible, the existing load in a column can be reduced by providing adjacent temporary supports and adequate shoring before constructing the jacket.

After chipping any plaster, the surface of the existing concrete should be roughened without damaging the concrete, especially due to poor quality of the existing concrete. Hence, roughening by a motorized wire brush is preferred to hacking. Sand blasting the surface can provide more roughness by exposing the aggregates.

Self-compacting concrete can be used for the jacket. The flowability of concrete is important with regard to the filling up of the annular space between the existing column and the formwork. A shrinkage-compensating admixture needs to be added to the new concrete.

The concrete jacket should be adequately cured before the column is reloaded.

#### SUMMARY AND CONCLUSIONS

The present study has investigated the effect of jacketing on the flexural strength and performance of columns. First, the specimen details and results of the slant shear tests for studying the interface between old and new concrete have been presented. Second, the testing of reference and retrofitted columns under pure compression, eccentric compression and pure bending has been documented. Third, the setup and testing of beam-column-joint sub-assembly specimens have been explained. Next, the prediction of the strength and behaviour of retrofitted column specimens has been illustrated. A lamellar analysis and a simplified analysis were used for the prediction. The incremental nonlinear analysis for predicting the lateral load versus displacement behaviour of a sub-assembly has been highlighted. Finally, guidelines for the retrofitting of columns by concrete jacketing have been provided.

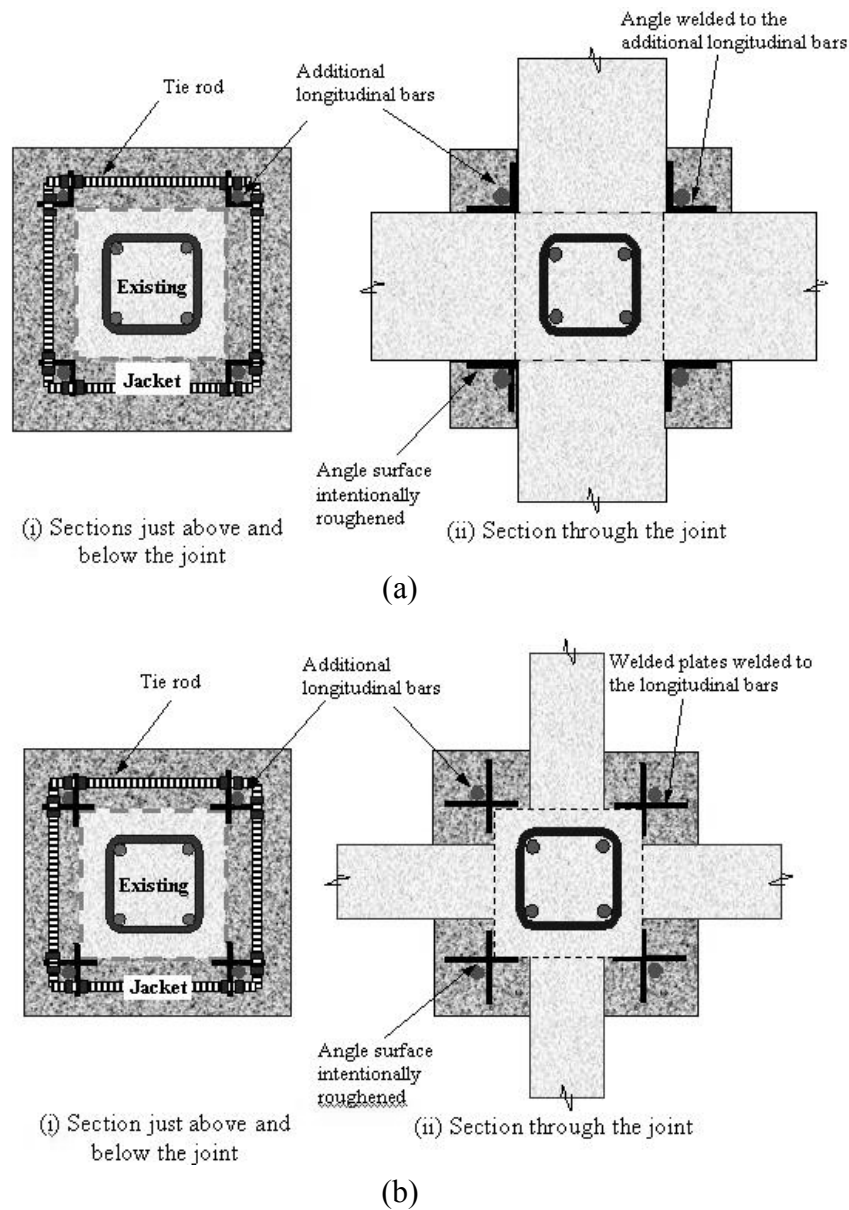


Fig. 36 Details of enhancing confinement of beam-to-column joints: (a) width of column same as that of beams, (b) width of column larger than that of beams

Following are the conclusions from the present study:

- The self-compacting concrete was found to be suitable for use in the concrete jacket.
- The retrofitted specimens did not show any visible delamination between the existing concrete and the concrete in the jacket. The roughening of the surface of the existing concrete by motorized wire brush was found to be satisfactory for the type of tests conducted.
- The moment capacities of the retrofitted column specimens were substantially more than those of the existing columns. This increase in capacities could be predicted by analysis.
- The retrofitted beam-column-joint sub-assembly specimens showed substantial increase in lateral strength, ductility (i.e., energy absorption) and energy dissipation.
- The degradations in strength and stiffness of the retrofitted sub-assembly specimen tested under cyclic loading were limited.
- A lamellar analysis considering the two grades of concrete in a retrofitted section, and the effect of confinement on the stress versus strain curve for concrete under compression, provides a good prediction of the strength and the moment versus curvature behaviour of the section. However, a simplified analysis considering the lower grade of concrete for the whole section and using the code-specified stress versus strain curve for the concrete under compression can give a conservative value

of the strength alone. It cannot correctly predict ductility in the moment versus curvature behaviour of the section.

- The prediction of the lateral load versus displacement behaviour of a sub-assembly in a building by the pushover analysis using bilinear (up to the peak) moment versus rotation curve for a plastic hinge is approximate, especially in the pre-yield region.
- The incremental nonlinear analysis, with varying flexural stiffness for the hinge members (included to model the spread plasticity) and incorporating friction of the bearings, showed substantially better prediction of the lateral load versus displacement behaviour of the retrofitted sub-assembly specimen as compared to the pushover analysis. The tension stiffening effect of cracked concrete may be considered for improved predictions in the pre-yield region.

Regarding the retrofitting of columns for flexure, tests can be conducted on larger-scale specimens with reduced increase in area after jacketing to study the improvements in strength and performance. The scheme of concrete jacketing selected in the present study needs to be qualified under a fast cyclic loading. This study can be extended to the exterior or corner columns by testing the corresponding sub-assembly specimens. Three-dimensional frames with jacketed columns can also be tested under the monotonic or cyclic lateral loads, or under a base excitation by using a shake table.

## REFERENCES

1. Abu-Tair, A.I., Rigden, S.R. and Burley, E. (1996). "Testing the Bond between Repair Materials and Concrete Substrate", *ACI Materials Journal*, Vol. 93, No. 6, pp. 553–558.
2. Aguilar, J., Juarez, H. and Iglesias, J. (1989). "The Mexico Earthquake of September 19, 1985—Statistics of Damage and of Retrofitting Techniques in Reinforced Concrete Buildings Affected by the 1985 Earthquake", *Earthquake Spectra*, Vol. 5, No. 1, pp. 145–151.
3. Alcocer, S.M. (1993). "RC Frames Connections Rehabilitated by Jacketing", *Journal of Structural Engineering*, ASCE, Vol. 119, No. 5, pp. 1413–1431.
4. Alcocer, S.M. and Jirsa, J.O. (1993). "Strength of Reinforced Concrete Frame Connections Rehabilitated by Jacketing", *ACI Structural Journal*, Vol. 90, No. 3, pp. 249–261.
5. Austin, S., Robins, P. and Pan, Y. (1999). "Shear Bond Testing of Concrete Repairs", *Cement and Concrete Research*, Vol. 29, No. 7, pp. 1067–1076.
6. Bett, B.J., Klingner, R.E. and Jirsa, J.O. (1988). "Lateral Load Response of Strengthened and Repaired Reinforced Concrete Column", *ACI Structural Journal*, Vol. 85, No. 5, pp. 499–508.
7. Beushausen, H. and Alexander, M.G. (2008). "Bond Strength Development between Concretes of Different Ages", *Magazine of Concrete Research*, Vol. 60, No. 1, pp. 65–74.
8. BIS (1993). "IS 13920: 1993—Indian Standard Ductile Detailing of Reinforced Concrete Structures Subjected to Seismic Forces—Code of Practice", Bureau of Indian Standards, New Delhi.
9. BIS (2000). "IS 456: 2000—Indian Standard Plain and Reinforced Concrete—Code of Practice (Fourth Revision)", Bureau of Indian Standards, New Delhi.
10. Bousias, S.N. and Fardis, M.N. (2003). "Experimental Research on Vulnerability and Retrofitting of Old-Type RC Columns under Cyclic Loading" in "Seismic Assessment and Rehabilitation of Existing Buildings (edited by S.T. Wasti and G. Özcebe)", Kluwer Academic Publishers, Dordrecht, The Netherlands.
11. BSI (1984). "BS 6319: 1984 (Part 4)—British Standard Criteria for Testing of Resin Compositions for Use in Construction", British Standards Institution, London, U.K.
12. Chakrabarti, A., Menon, D. and Sengupta, A.K. (2008). "Handbook on Seismic Retrofit of Buildings", Narosa Publishing House, New Delhi.
13. Climaco, J.C.T.S. and Regan, P.E. (2001). "Evaluation of Bond Strength between Old and New Concrete in Structural Repairs", *Magazine of Concrete Research*, Vol. 53, No. 6, pp. 377–390.
14. Ersoy, U.A., Tankut, T. and Suleiman, R. (1993). "Behaviour of Jacketed Columns", *ACI Structural Journal*, Vol. 90, No. 3, pp. 288–293.
15. Gnanasekaran, K. (2009). "Seismic Retrofit of Reinforced Concrete Columns in Buildings Using Concrete Jacket", Ph.D. Thesis, Department of Civil Engineering, Indian Institute of Technology Madras, Chennai.

16. IITM-SERC (2005). "Manual for Seismic Evaluation and Retrofit of Multi-storeyed RC Buildings", Technical Report, Indian Institute of Technology Madras and Structural Engineering Research Centre, Chennai.
17. Julio, E.S., Branco, F. and Silva, V.D. (2003). "Structural Rehabilitation of Columns with Reinforced Concrete Jacketing", *Progress in Structural Engineering and Materials*, Vol. 5, No. 1, pp. 29–37.
18. Kamat, D.R. and Sengupta, A.K. (2006). "Assessment of Seismic Vulnerability of Mid Rise Multi-Storeyed Reinforced Concrete Buildings in India", *ICI Journal*, Vol. 7, No. 2, pp. 23–25.
19. Mander, J.B., Priestley, M.J.N. and Park, R. (1988). "Theoretical Stress-Strain Model for Confined Concrete", *Journal of Structural Engineering, ASCE*, Vol. 114, No. 8, pp. 1804–1826.
20. Murty, C.V.R., Goel, R.K., Goyal, A., Jain, S.K., Sinha, R., Rai, D.C., Arlekar, J.N. and Metzger, R. (2002). "Reinforced Concrete Structures", *Earthquake Spectra*, Vol. 18, No. S1, pp. 149–185.
21. Rodriguez, M. and Park, R. (1994). "Seismic Load Tests on Reinforced Concrete Columns Strengthened by Jacketing", *ACI Structural Journal*, Vol. 91, No. 2, pp. 150–159.
22. Saatcioglu, M. and Ozcebe, G. (1989). "Response of Reinforced Concrete Columns to Simulated Seismic Loading", *ACI Structural Journal*, Vol. 86, No. 1, pp. 3–12.
23. Stoppenhagen, D.R., Jirsa, J.O. and Wyllie, Jr., L.A. (1995). "Seismic Repair and Strengthening of a Severely Damaged Concrete Frame", *ACI Structural Journal*, Vol. 92, No. 2, pp. 177–187.
24. Valluvan, R., Kreger, M.E. and Jirsa, J.O. (1993). "Strengthening of Column Splices for Seismic Retrofit of Nonductile Reinforced Concrete Frames", *ACI Structural Journal*, Vol. 90, No. 4, pp. 432–440.
25. Vandoros, K.G. and Dritsos, S.E. (2006). "Concrete Jacket Construction Detail Effectiveness When Strengthening RC Columns", *Construction and Building Materials*, Vol. 22, No. 3, pp. 264–276.

## **TWO-DIMENSIONAL STATIC DEFORMATION OF AN ORTHOTROPIC ELASTIC LAYERED HALF-SPACE DUE TO BLIND STRIKE-SLIP FAULT**

Shamta Chugh\*, Kuldip Singh\* and Dinesh Kumar Madan\*\*

\*Department of Mathematics

Guru Jambheshwar University of Science and Technology, Hisar-125001

\*\*Department of Mathematics

The Technological Institute of Textile and Sciences, Bhiwani-127021

### **ABSTRACT**

Closed-form analytical expressions for the deformation at any point of a horizontal orthotropic elastic layer of infinite lateral extent (coupling in different ways such as ‘welded’, ‘smooth-rigid’, or ‘rough-rigid’ to a base) due to a long blind strike-slip fault are obtained. The results obtained are generalization of the results for an isotropic medium. For different types of coupling, the effects of variations in depth on surface displacement are presented graphically. Also, at different depth levels, the variations of surface displacements with the horizontal distance from the inclined fault are compared to study the effects of different types of coupling. The results for the present model are compared with the corresponding results for a uniform orthotropic elastic half-space. It is observed that the displacement field varies more significantly in an orthotropic elastic layered half-space in comparison with a uniform orthotropic half-space. Numerically, the effect of anisotropy is also examined. It is found that anisotropy of the source half-space has a significant effect on the displacement at different depth levels.

**KEYWORDS:** Static Deformation, Surrounding Faults, Orthotropic Medium, Blind Fault, Strike-Slip

### **INTRODUCTION**

Many major faults reach and intersect with the surface of the earth. This intersection produces a linear feature called fault trace. Some faults do not reach the surface, however, and scientists refer to those as blind-faults. The devastating earthquake at Bam, Iran in 2003 is a well-documented case of blind strike-slip fault. It is common for earthquakes to occur on blind faults, which usually produce long-term surface effects by which their existence may be recognized (Talebian et al., 2004).

The upper part of the earth is anisotropic (Dziewonski and Anderson, 1981). Most anisotropic media of interest in seismology have at least one horizontal plane of symmetry. A plane of symmetry is a plane in which the elastic properties have reflection symmetry, and a medium with three mutually orthogonal planes of symmetry is known as orthorhombic. A large part of the earth is considered as having orthotropic symmetry (Crampin, 1994). The orthotropic symmetry of the upper mantle is believed to be caused by the orthorhombic crystals of olivine relative to the spreading centers (Hess, 1964). Orthorhombic symmetry is also expected to occur in sedimentary basins as a result of the combination of vertical cracks with a horizontal axis of symmetry and periodic thin-layer anisotropy with a vertical axis of symmetry (Bush and Crampin, 1987). In the case of one plane of symmetry, if the orthorhombic is horizontal, the symmetry is termed as orthotropic symmetry (Crampin, 1989). Since the orientation of stress in the crust is usually orthotropic, most symmetry systems in the earth’s crust also have orthotropic orientations. The orthotropy symmetry is also exhibited by olivine and orthopyroxenes which are the principal rock-forming minerals of the deep crust and the upper mantle.

The static deformation of a semi-infinite elastic isotropic medium due to a very long strike-slip fault has been studied by many researchers, e.g., Kasahara (1964), and Rybicki (1971, 1978). The results of these studies have been successfully applied to several earthquakes, e.g., 1906 San Andreas, 1927 Tango, 1948 Fukui, and 1966 Parkfield-Cholame. Analytical expressions for the surface deformation and internal deformation due to inclined shear and tensile faults in a homogeneous isotropic half-space are given by Okada (1985, 1992).

Using the body force equivalent of dislocation source as discussed by Burridge and Knopoff (1964) and Aki and Richards (1980), Pan (1989) obtained the response of a transversely isotropic layered medium to general dislocation sources. Using the results of Ben-Menahem and Singh (1968) and the method developed by Singh (1970), Rundle (1980) obtained the surface displacements due to a point source in a multilayered self-gravitating half-space.

Garg et al. (1996) obtained the representation of seismic sources causing antiplane-strain deformation of an orthotropic medium. Madan and Garg (1997) obtained analytical expressions for the displacements and stresses at any point of an orthotropic horizontal elastic layer, coupling in different ways such as ‘welded’, ‘smooth-rigid’, or ‘rough-rigid’ to a base, due to a very long inclined strike-slip fault.

Wang et al. (2003) introduced the techniques (i.e., orthonormalized Haskell propagator, analytical asymptotes, filter techniques, etc.) used to solve the stability and convergence problems when computing the Green functions. These techniques lead to small, fast and very accurate programs. Fernández and Rundle (2004) considered the problem of surface deformation arising from a fault in a semi-infinite, elastic-gravitational, and/or viscoelastic-gravitational, plane-layered medium which is subjected to an externally imposed gravitational acceleration. Fukahata and Matsu’ura (2006) used the correspondence principle of linear viscoelasticity to obtain the quasi-static deformation due to dislocation source in a multilayered elastic/viscoelastic half-space under gravity and also gave the equivalence theorem. Wang et al. (2006) presented a method and software to determine the surface and sub-surface deformations, as well as changes in the geoid and gravity, due to the common geophysical sources in a multilayered viscoelastic-gravitational half-space.

Recently, Rani and Singh (2005) obtained the static deformation of an isotropic semi-infinite elastic medium, consisting of a horizontal elastic layer in welded contact with an isotropic elastic half-space, due to a long blind strike-slip fault located in an elastic layer.

The present paper aims to study the static deformation of a horizontal orthotropic elastic layer of an infinite lateral extent, which is coupling in different ways to a base due to a long blind strike-slip fault situated in the elastic layer. The coupling of the layer with the base need not necessarily be ‘welded’; it may also be of the ‘smooth-rigid’ or ‘rough-rigid’ type. The different deformations of the horizontal orthotropic elastic layer corresponding to various types of its coupling with the base have been obtained analytically. In the study of Madan and Garg (1997), the depth  $d$  of the upper edge of the fault does not occur explicitly in the solution. Moreover, as the dip angle tends to zero, the fault approaches the surface of the earth. Therefore, their results cannot be used to study the deformation of a two-layer model caused by the deep strike-slip faults of small dip angles.

In the present formulation, depth  $d$  shows up explicitly in the solution. Therefore, the effects of variations in depth for a fixed dip with different types of coupling can be studied directly. The results obtained here are generalization of the results from an isotropic medium in the sense that the medium considered for the present work is orthotropic, which is more realistic than isotropic, and the results for the isotropic case can be derived from our results. Graphs showing the effects of variations in depth  $d$  on surface displacements for different types of coupling at different depth levels are presented. Numerically, the surface displacements for an orthotropic layered half-space are compared with the corresponding displacements for a uniform orthotropic elastic half-space. Also, at different depth levels, the surface displacements for different types of coupling (i.e., ‘welded’, ‘smooth’, and ‘rough’) are compared numerically.

## BASIC EQUATIONS

In the Cartesian coordinate system  $(x, y, z)$  the equations of equilibrium are

$$\tau_{ij,j} + F_i = 0 ; \quad i, j = 1, 2, 3 \tag{1}$$

where  $\tau_{ij}$  denotes the stress components and  $F_i$  represents the body forces per unit volume. The strain-displacement relations are

$$e_{11} = \frac{\partial u}{\partial x}, \quad e_{12} = \frac{1}{2} \left( \frac{\partial u}{\partial y} + \frac{\partial v}{\partial x} \right), \text{ etc.} \tag{2}$$

where  $u, v, w$  denote the displacement components along the  $x-, y-, z$ -axes, respectively.

For an orthotropic elastic medium, with coordinate planes coinciding with the planes of symmetry and with one plane of symmetry being horizontal, the stress-strain relations in matrix form are (Chung, 1996)

$$\begin{bmatrix} \tau_{11} \\ \tau_{22} \\ \tau_{33} \\ \tau_{23} \\ \tau_{13} \\ \tau_{12} \end{bmatrix} = \begin{bmatrix} c_{11} & c_{12} & c_{13} & 0 & 0 & 0 \\ c_{12} & c_{22} & c_{23} & 0 & 0 & 0 \\ c_{13} & c_{23} & c_{33} & 0 & 0 & 0 \\ 0 & 0 & 0 & c_{44} & 0 & 0 \\ 0 & 0 & 0 & 0 & c_{55} & 0 \\ 0 & 0 & 0 & 0 & 0 & c_{66} \end{bmatrix} \begin{bmatrix} e_{11} \\ e_{22} \\ e_{33} \\ 2e_{23} \\ 2e_{13} \\ 2e_{12} \end{bmatrix} \quad (3)$$

where the two-suffix quantity  $c_{ij}$  denotes the elastic constants of the medium. A transversely isotropic elastic medium, with the  $z$ -axis coinciding with the axis of symmetry, is a particular case of an orthotropic medium for which

$$c_{11} = c_{22}, \quad c_{23} = c_{13}, \quad c_{55} = c_{44}, \quad c_{66} = \frac{1}{2}(c_{11} - c_{12}) \quad (4)$$

and the number of independent elastic constants reduces from nine to five. For an elastic isotropic medium, these constants reduce to just two as given below,

$$\begin{aligned} c_{11} &= c_{22} = c_{33} = \lambda + 2\mu \\ c_{12} &= c_{13} = c_{23} = \lambda \\ c_{44} &= c_{55} = c_{66} = \mu \end{aligned} \quad (5)$$

where  $\lambda$  and  $\mu$  are the Lamé's constants.

There are two distinct approaches by which one can represent a source in the seismological boundary value problems. In the first approach, one uses a body force equivalent to the source. Consequently, the equations of motion become inhomogeneous due to the presence of the source term. In the second approach, the source is removed from the equation of motion, which becomes homogeneous, but appears instead as a source condition. This source condition corresponds to the jump in the displacement and stress components across a coordinate surface passing through the source. With reference to the second approach, the equilibrium equations for zero body forces are given by

$$\frac{\partial \tau_{11}}{\partial x} + \frac{\partial \tau_{12}}{\partial y} + \frac{\partial \tau_{13}}{\partial z} = 0 \quad (6)$$

$$\frac{\partial \tau_{21}}{\partial x} + \frac{\partial \tau_{22}}{\partial y} + \frac{\partial \tau_{23}}{\partial z} = 0 \quad (7)$$

$$\frac{\partial \tau_{31}}{\partial x} + \frac{\partial \tau_{32}}{\partial y} + \frac{\partial \tau_{33}}{\partial z} = 0 \quad (8)$$

Let the elastic medium under consideration be under the conditions of antiplane-strain deformation in the  $yz$ -plane due to a very long strike-slip dislocation parallel to the  $x$ -axis. In this case, the displacement vector is parallel to the  $x$ -axis (or the direction of the fault strike) and  $\partial(\cdot)/\partial x \equiv 0$ . Thus, under the state of antiplane-strain deformation,  $v = w = 0$ , and  $u = u(y, z)$ . The non-zero stresses can be written as

$$\tau_{12} = c\alpha^2 \frac{\partial u}{\partial y}, \quad \tau_{13} = c \frac{\partial u}{\partial z} \quad (9)$$

where

$$c = c_{55}, \quad c_{66} = c\alpha^2 \quad (10)$$

and  $\alpha$  and  $c$  are real positive numbers. In the case of an isotropic elastic medium,  $c = \mu$  and  $\alpha = 1$ .

The equilibrium equations (i.e., Equations (7) and (8)) are identically satisfied for the antiplane-strain deformation. In that case, Equation (6) is reduced to

$$\frac{\partial^2 u}{\partial y^2} + \frac{1}{\alpha^2} \frac{\partial^2 u}{\partial z^2} = 0 \tag{11}$$

and the source condition to be satisfied by the resulting tractions becomes (Maruyama, 1966)

$$\oint \tau_{1k} \nu_k d\sigma = F \tag{12}$$

where  $F$  is the magnitude of the force (per unit length) acting at the point  $(\xi_2, \xi_3)$  in an infinite homogeneous orthotropic elastic medium in the positive  $x$ -direction, and  $\nu_k$  denotes the direction cosines of the exterior normal.

The solution of Equation (11) using the source boundary condition of Equation (12) becomes (Garg et al., 1996)

$$u = \frac{-F}{4\pi\alpha c} \log \left[ (y - \xi_2)^2 + \alpha^2 (z - \xi_3)^2 \right] \tag{13}$$

for the displacement parallel to the  $x$ -axis and at any point  $(y, z)$  of an orthotropic elastic infinite medium, due to a line source, which is parallel to the  $x$ -axis and is passing through the point  $(\xi_2, \xi_3)$ .

### 1. Single Couples ( $xy$ ) and ( $xz$ )

At the point  $(\xi_2, \xi_3)$ , there acts a two-dimensional line source—either a single couple ( $xy$ ) or a single couple ( $xz$ ). The displacements  $u^{(xy)}$  and  $u^{(xz)}$  parallel to the  $x$ -axis, due to the single couple ( $xy$ ) of moment  $F_{xy}$  and due to the single couple ( $xz$ ) of moment  $F_{xz}$ , respectively, are found to be

$$u^{(xy)} = \frac{F_{xy}}{2\pi\alpha c} \int_0^\infty e^{-k\alpha|z-\xi_3|} \sin k(y - \xi_2) dk \tag{14}$$

$$u^{(xz)} = \pm \frac{F_{xz}}{2\pi\alpha c} \int_0^\infty e^{-k\alpha|z-\xi_3|} \cos k(y - \xi_2) dk \tag{15}$$

These displacements (parallel to the  $x$ -axis, and due to the line source of a single couple ( $xy$ ) or ( $xz$ )) can be unified into the following integral:

$$u_0 = \int_0^\infty \left[ A_0 \sin k(y - \xi_2) + B_0 \cos k(y - \xi_2) \right] e^{-\alpha k|z-\xi_3|} dk \tag{16}$$

The source coefficients  $A_0$  and  $B_0$  for various two-dimensional buried sources are given in Table 1.

## FORMULATION AND SOLUTION OF THE PROBLEM

We consider a semi-infinite medium consisting of a homogeneous orthotropic elastic horizontal layer of thickness  $H$  lying over a homogeneous orthotropic elastic half-space. The origin of the Cartesian coordinate system  $(x, y, z)$  is placed at the upper boundary of the semi-infinite medium with the  $z$ -axis vertically downwards (see Figure 1). The layer, therefore, occupies the region  $0 \leq z < H$ . It is assumed that an orthotropic elastic horizontal layer is coupling in different ways such as ‘welded’, ‘smooth-rigid’, or ‘rough-rigid’ to a base. We consider an inclined strike-slip fault of finite width  $L$  with an arbitrary dip angle  $\delta$ , which lies completely in the orthotropic horizontal elastic layer and whose upper edge is at depth  $d$  below the earth surface.

The boundary surface  $z = 0$  is a horizontal plane and a plane of elastic symmetry. It is further assumed that this plane is traction free, so that

$$\tau_{13}|_{z=0} = 0 \tag{17}$$

and the boundary conditions at the interface  $z = H$  for different types of coupling are

$$u|_{z=H^+} = u|_{z=H^-}, \quad \tau_{13}|_{z=H^+} = \tau_{13}|_{z=H^-} \tag{18}$$

for the welded contact,

$$\tau_{13}|_{z=H} = 0 \tag{19}$$

for the smooth-rigid contact, and

$$u|_{z=H} = 0 \tag{20}$$

for the rough-rigid contact.

**Table 1: Source Coefficients for Various Seismic Sources**

Source	$A_0$	$B_0$
Single Couple (12)	$\frac{F_{xy}}{2\pi\alpha c}$	0
Single Couple (13)	0	$\pm \frac{F_{xz}}{2\pi c}$
The upper sign is for $z > \xi_3$ and the lower sign for $z < \xi_3$ . $F_{xy}$ and $F_{xz}$ are, respectively, the moments of couples (xy) and (xz).		

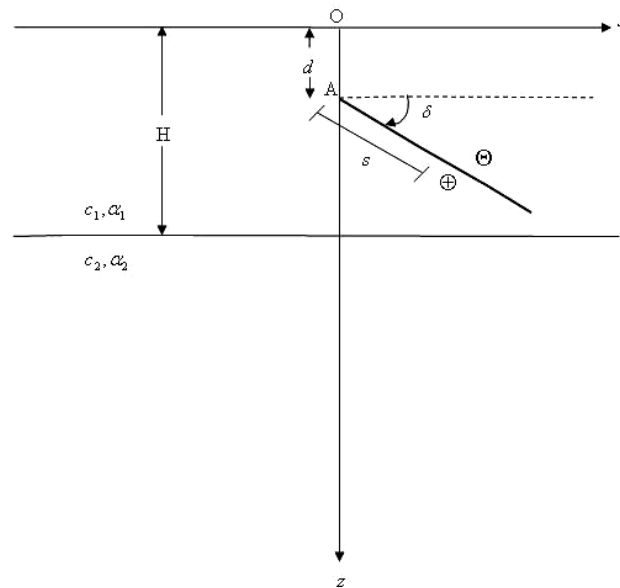


Fig. 1 Geometry of an inclined strike-slip fault of finite width  $L$  situated in an orthotropic layer of uniform thickness  $H$  lying over a half-space (the displacement discontinuity on the inclined fault is parallel to the  $x$ -axis; the symbol  $\oplus$  indicates displacement in the direction of the  $x$ -axis and the symbol  $\ominus$  in the opposite direction;  $d$  is the depth of the upper edge  $A$  of the fault and  $\delta$  is the dip angle;  $s$  is the distance from the upper edge of the fault measured in the dip direction)

For a line source acting at the point  $(\xi_2, \xi_3)$  of the layer, suitable expressions for the horizontal displacements parallel to the line source and satisfying Equation (11), in the layer and in the half-space, are

$$u^{(1)} = u_0 + \int_0^\infty [A_1 \sin k(y - \xi_2) + B_1 \cos k(y - \xi_2)] e^{-\alpha_1 k z} dk + \int_0^\infty [C_1 \sin k(y - \xi_2) + C_1 \cos k(y - \xi_2)] e^{\alpha_1 k z} dk \quad (21)$$

for  $0 \leq z < H$ , and

$$u^{(2)} = \int_0^\infty [A_2 \sin k(y - \xi_2) + B_2 \cos k(y - \xi_2)] e^{-\alpha_2 k z} dk \quad (22)$$

for  $z > H$ . Here, the superscript (1) is for the layer and superscript (2) for the half-space. The coefficients  $A_1, B_1$ , etc. for each type of coupling can be determined by using the boundary conditions of Equations (17)–(20).

### 1. Inclined Strike-Slip Fault

The displacement field due to a very long strike-slip line fault of arbitrary dip  $\delta$  can be expressed in terms of two fields, one due to a horizontal strike-slip fault and the other due to a vertical strike-slip fault, in the form (Singh and Garg, 1985)

$$u = u^{(HS)} \cos \delta + u^{(VS)} \sin \delta \quad (23)$$

where  $u^{(HS)}$  is the displacement for the horizontal strike-slip fault, and  $u^{(VS)}$  is the displacement for the vertical strike-slip fault.

Using the results for the horizontal and vertical strike-slip faults, as obtained earlier by Garg et al. (1996), we obtain the following expressions for the displacements due to the ‘welded’ contact, which is parallel to the  $x$ -axis, due to a long strike-slip fault of finite width  $L$ :

$$u^{(1)} = \frac{b\alpha_1}{2\pi} \left\{ \sum_{n=0}^\infty T^n \left[ \frac{(2nH + z - \xi_3) \cos \delta - (y - \xi_2) \sin \delta}{(y - \xi_2)^2 + [\alpha_1(2nH + z - \xi_3)]^2} - \frac{(2nH + z + \xi_3) \cos \delta + (y - \xi_2) \sin \delta}{(y - \xi_2)^2 + [\alpha_1(2nH + z + \xi_3)]^2} \right] + \sum_{n=1}^\infty T^n \left[ \frac{(2nH - z - \xi_3) \cos \delta - (y - \xi_2) \sin \delta}{(y - \xi_2)^2 + [\alpha_1(2nH - z - \xi_3)]^2} - \frac{(2nH - z + \xi_3) \cos \delta + (y - \xi_2) \sin \delta}{(y - \xi_2)^2 + [\alpha_1(2nH - z + \xi_3)]^2} \right] \right\} ds \quad (24)$$

for  $0 \leq z < H$ , and

$$u^{(2)} = -\frac{b}{2\pi} \left\{ \sum_{n=0}^\infty (1+T) T^n \left[ \frac{[\alpha_1(2nH + H + \xi_3) + \alpha_2(z - H)] \cos \delta + \alpha_1(y - \xi_2) \sin \delta}{(y - \xi_2)^2 + [\alpha_1(2nH + H + \xi_3) + \alpha_2(z - H)]^2} - \frac{[\alpha_1(2nH + H - \xi_3) + \alpha_2(z - H)] \cos \delta - \alpha_1(y - \xi_2) \sin \delta}{(y - \xi_2)^2 + [\alpha_1(2nH + H - \xi_3) + \alpha_2(z - H)]^2} \right] \right\} ds \quad (25)$$

for  $z > H$ , where  $b$  is the uniform slip;  $ds$  is the infinitesimal width of the line dislocation (parallel to the  $x$ -axis);  $c_1, \alpha_1$  and  $c_2, \alpha_2$  are the elastic constants for the orthotropic elastic layer and the half-space, respectively;

$$T = \frac{1-m}{1+m}, \quad m = \frac{c_2 \alpha_2}{c_1 \alpha_1} \quad (26)$$

and  $s$  is the distance from the upper edge of the fault measured in the down-dip direction.

On substituting  $\xi_2 = s \cos \delta$  and  $\xi_3 = d + s \sin \delta$  into Equations (24) and (25) and then on integrating over  $s$  from 0 to  $L$ , we obtain the following expressions for the displacements and stresses:

$$u^{(1)} = \frac{b}{2\pi} \left[ \sum_{n=0}^{\infty} T^n \left\{ \tan^{-1} \frac{T_2}{T_1} - \tan^{-1} \frac{T_4}{T_3} \right\} + \sum_{n=1}^{\infty} T^n \left\{ \tan^{-1} \frac{T_6}{T_5} - \tan^{-1} \frac{T_8}{T_7} \right\} \right] \Big|_0^L \quad (27)$$

$$\tau_{12}^{(1)} = \frac{bc_1\alpha_1^3 T_0}{2\pi} \left[ \sum_{n=0}^{\infty} T^n \left\{ \frac{2nH + z + d + s \sin \delta}{T_3^2 + T_4^2} - \frac{2nH + z - d - s \sin \delta}{T_1^2 + T_2^2} \right\} + \sum_{n=1}^{\infty} T^n \left\{ \frac{2nH - z + d + s \sin \delta}{T_7^2 + T_8^2} - \frac{2nH - z - d - s \sin \delta}{T_5^2 + T_6^2} \right\} \right] \Big|_0^L \quad (28)$$

$$\tau_{13}^{(1)} = \frac{bc_1\alpha_1 T_0}{2\pi} \left[ \sum_{n=0}^{\infty} T^n \left\{ \frac{y - s \cos \delta}{T_1^2 + T_2^2} - \frac{y - s \cos \delta}{T_3^2 + T_4^2} \right\} - \sum_{n=1}^{\infty} T^n \left\{ \frac{y - s \cos \delta}{T_5^2 + T_6^2} - \frac{y - s \cos \delta}{T_7^2 + T_8^2} \right\} \right] \Big|_0^L \quad (29)$$

for  $0 \leq z < H$ , and

$$u^{(2)} = -\frac{b}{2\pi} \left[ \sum_{n=0}^{\infty} (1+T) T^n \left\{ \tan^{-1} \frac{T_{10}}{T_9} + \tan^{-1} \frac{T_{12}}{T_{11}} \right\} \right] \Big|_0^L \quad (30)$$

$$\tau_{12}^{(2)} = \frac{bc_2\alpha_2^2 T_0}{2\pi} \left[ \sum_{n=0}^{\infty} (1+T) T^n \left\{ \frac{[\alpha_1(2nH + H + d) + \alpha_2(z - H)] + \alpha_1 s \sin \delta}{T_9^2 + T_{10}^2} - \frac{[\alpha_1(2nH + H - d) + \alpha_2(z - H)] - \alpha_1 s \sin \delta}{T_{11}^2 + T_{12}^2} \right\} \right] \Big|_0^L \quad (31)$$

$$\tau_{13}^{(2)} = \frac{bc_2\alpha_1 T_0}{2\pi} \left[ \sum_{n=0}^{\infty} (1+T) T^n \left\{ \frac{y - s \cos \delta}{T_{11}^2 + T_{12}^2} - \frac{y - s \cos \delta}{T_9^2 + T_{10}^2} \right\} \right] \Big|_0^L \quad (32)$$

for  $z > H$ , where

$$\begin{aligned} T_0 &= (\cos^2 \delta + \alpha_1^2 \sin^2 \delta); & T_1 &= \alpha_1 [(2nH + z - d) \cos \delta - y \sin \delta] \\ T_2 &= T_0 s - [y \cos \delta + \alpha_1^2 (2nH + z - d) \sin \delta]; & T_3 &= \alpha_1 [(2nH + z + d) \cos \delta + y \sin \delta] \\ T_4 &= T_0 s - [y \cos \delta - \alpha_1^2 (2nH + z + d) \sin \delta]; & T_5 &= \alpha_1 [(2nH - z - d) \cos \delta - y \sin \delta] \\ T_6 &= T_0 s - [y \cos \delta + \alpha_1^2 (2nH - z - d) \sin \delta]; & T_7 &= \alpha_1 [(2nH - z + d) \cos \delta + y \sin \delta] \\ T_8 &= T_0 s - [y \cos \delta - \alpha_1^2 (2nH - z + d) \sin \delta] \\ T_9 &= \alpha_1 y \sin \delta + [\alpha_1(2nH + H + d) + \alpha_2(z - H)] \cos \delta \\ T_{10} &= T_0 s - [y \cos \delta - \{\alpha_1(2nH + H + d) + \alpha_2(z - H)\} \alpha_1 \sin \delta] \\ T_{11} &= \alpha_1 y \sin \delta - [\alpha_1(2nH + H - d) + \alpha_2(z - H)] \cos \delta \\ T_{12} &= T_0 s - [y \cos \delta + \{\alpha_1(2nH + H - d) + \alpha_2(z - H)\} \alpha_1 \sin \delta] \end{aligned} \quad (33)$$

and

$$f(s) \Big|_0^L = f(L) - f(0) \quad (34)$$

It has been verified that the boundary conditions in Equation (18) are identically satisfied by Equations (27)–(32).

On putting  $\alpha_1 = \alpha_2 = \alpha$ ,  $c_1 = c_2 = c$ , and  $T = 0$  in Equation (27) or (30), we get the displacement field due to a very long blind strike-slip fault of finite width  $L$  in a uniform orthotropic elastic half-space:

$$u = \frac{b}{2\pi} \left[ \tan^{-1} \frac{(\cos^2 \delta + \alpha^2 \sin^2 \delta) s - [y \cos \delta + \alpha^2 (z-d) \sin \delta]}{\alpha [(z-d) \cos \delta - y \sin \delta]} - \tan^{-1} \frac{(\cos^2 \delta + \alpha^2 \sin^2 \delta) s - [y \cos \delta - \alpha^2 (z+d) \sin \delta]}{\alpha [(z+d) \cos \delta + y \sin \delta]} \right] \Bigg|_0^L \quad (35)$$

The corresponding stresses can be obtained on using Equation (35) in Equation (9).

## 2. Particular Cases

### 2.1 Smooth-Rigid Contact

When the interface  $z = H$  between the layer and the half-space is ‘smooth-rigid’, on taking  $m = 0$ , i.e.,  $T = 1$ , in Equations (27) and (30), we obtain the corresponding displacement field as

$$u^{(1)} = \frac{b}{2\pi} \left[ \tan^{-1} \frac{(\cos^2 \delta + \alpha_1^2 \sin^2 \delta) s - [y \cos \delta + \alpha_1^2 (z-d) \sin \delta]}{\alpha_1 [(z-d) \cos \delta - y \sin \delta]} - \tan^{-1} \frac{(\cos^2 \delta + \alpha_1^2 \sin^2 \delta) s - [y \cos \delta - \alpha_1^2 (z+d) \sin \delta]}{\alpha_1 [(z+d) \cos \delta + y \sin \delta]} + \sum_{n=1}^{\infty} \left\{ \tan^{-1} \frac{T_2}{T_1} - \tan^{-1} \frac{T_4}{T_3} + \tan^{-1} \frac{T_6}{T_5} - \tan^{-1} \frac{T_8}{T_7} \right\} \right] \Bigg|_0^L \quad (36)$$

for  $0 \leq z < H$ , and

$$u^{(2)} = -\frac{b}{\pi} \left[ \tan^{-1} \frac{(\cos^2 \delta + \alpha_1^2 \sin^2 \delta) s - [y \cos \delta - \{\alpha_1 (H+d) + \alpha_2 (z-H)\} \alpha_1 \sin \delta]}{\alpha_1 y \sin \delta + [\alpha_1 (H+d) + \alpha_2 (z-H)] \cos \delta} + \tan^{-1} \frac{(\cos^2 \delta + \alpha_1^2 \sin^2 \delta) s - [y \cos \delta + \{\alpha_1 (H-d) + \alpha_2 (z-H)\} \alpha_1 \sin \delta]}{\alpha_1 y \sin \delta - [\alpha_1 (H-d) + \alpha_2 (z-H)] \cos \delta} + \sum_{n=1}^{\infty} \left\{ \tan^{-1} \frac{T_{10}}{T_9} + \tan^{-1} \frac{T_{12}}{T_{11}} \right\} \right] \Bigg|_0^L \quad (37)$$

for  $z > H$ .

### 2.2 Rough-Rigid Contact

When the interface  $z = H$  between the layer and the half-space is ‘rough-rigid’, on letting  $m \rightarrow \infty$ , i.e.,  $T = -1$ , in Equations (27) and (30), we get the displacement field as

$$u^{(1)} = \frac{b}{2\pi} \left[ \tan^{-1} \frac{(\cos^2 \delta + \alpha_1^2 \sin^2 \delta) s - [y \cos \delta + \alpha_1^2 (z-d) \sin \delta]}{\alpha_1 [(z-d) \cos \delta - y \sin \delta]} - \tan^{-1} \frac{(\cos^2 \delta + \alpha_1^2 \sin^2 \delta) s - [y \cos \delta - \alpha_1^2 (z+d) \sin \delta]}{\alpha_1 [(z+d) \cos \delta + y \sin \delta]} \right] \quad (38)$$

$$+ \sum_{n=1}^{\infty} (-1)^n \left\{ \tan^{-1} \frac{T_2}{T_1} - \tan^{-1} \frac{T_4}{T_3} + \tan^{-1} \frac{T_6}{T_5} - \tan^{-1} \frac{T_8}{T_7} \right\} \Bigg|_0^L$$

for  $0 \leq z < H$ , and

$$u^{(2)} = 0 \tag{39}$$

for  $z > H$ .

### 2.3 Isotropic Case

The results for the corresponding problem for an isotropic case can be obtained as a particular case of the results given in Equations (27) and (30) by taking  $\alpha_1 = \alpha_2 = 1$ ,  $c_1 = \mu_1$ ,  $c_2 = \mu_2$ , and  $T = (\mu_1 - \mu_2) / (\mu_1 + \mu_2)$ . The results so obtained coincide with the results obtained by Rani and Singh (2005).

## NUMERICAL RESULTS

In this section, we examine the effect of the variation in the depth  $d$  of the upper edge of the fault on the displacement field caused by a uniform slip along a very long strike-slip fault, for each type of coupling between the orthotropic elastic layer lying over an orthotropic elastic half-space and the base (see Figure 1). Further, we compare the displacement field, due to a very long strike-slip fault of finite width  $L$  with its edge at distance  $d$  from the surface which is located in the orthotropic elastic layer and is in ‘welded’ contact with the orthotropic half-space along the horizontal plane, with the corresponding displacement field for a uniform orthotropic elastic half-space. The effects of different types of coupling between the orthotropic elastic layer and the base upon the displacement  $u^{(1)}$  with the horizontal distance  $y$  from the fault are also examined.

We define the dimensionless displacement and distance as  $U^{(1)} = u^{(1)} / b$  and  $Y = y / H$ , respectively. Further, we assume  $L = H / 2$  and  $\gamma = d / H$ . For the orthotropic layered medium, we use the values of the elastic constants,  $\alpha_1 = 0.9824$ ,  $c_1 = 2.87 \times 10^{11}$  dynes/cm<sup>2</sup> (28.7 GPa) for the material baryte, as given by Love (1944), and  $\alpha_2 = 0.9894$ ,  $c_2 = 8.10 \times 10^{11}$  dynes/cm<sup>2</sup> (81 GPa) for the material olivine, as given by Verma (1960). In the case of a uniform orthotropic elastic half-space, we consider the material to be baryte. The explicit analytical expressions describing the elastic field involve infinite series. The infinite series appearing at the right hand side of Equations (27) and (30) converge very rapidly. In numerical computations, it is found that the first twenty terms of the infinite series, which appear in the closed-form expression for the displacement  $u$ , are adequate and, therefore, the series is truncated after the first twenty terms.

Figures 2(a)–2(c) exhibit the variations of the dimensionless surface displacement  $U^{(1)}$  with the dimensionless horizontal distance  $Y$  from the upper edge of the fault for four different values of  $\gamma$  ( $= 0, 1/4, 2/3, 1$  for the ‘welded’, ‘smooth’, ‘rough’ contacts, respectively) at the dip angle  $\delta = 30^\circ, 15^\circ, \text{ and } 60^\circ$ , respectively. We observe that the displacement for the surface-breaking fault (i.e.,  $\gamma = 0$ ) is discontinuous at  $Y = 0$ , while it is continuous at all values of  $Y$  for  $\gamma = 1/4, 2/3, 1$ , for each type of coupling between the orthotropic elastic layer and the orthotropic elastic half-space. It follows that for the surface-breaking fault (i.e.,  $\gamma = 0$ ), the amount of discontinuity in the horizontal displacement at the point  $Y = 0$  is unity for all possible types of coupling.

Next, in Figures 3(a)–3(f), we compare the surface displacement due to a very long strike-slip fault for an orthotropic layered elastic medium with the corresponding displacement for a uniform orthotropic elastic half-space. In the Figures 3(a)–3(d), the dimensionless horizontal displacements parallel to the fault at  $\delta = 30^\circ$  have been shown for four different depth levels  $\gamma = 1/4, 1/2, 2/3, 1$ , respectively. Figures 3(e) and 3(f) show the variations of  $U^{(1)}$  due to a long vertical strike-slip fault at different depth levels  $\gamma = 1/2$  and  $2/3$ , respectively.

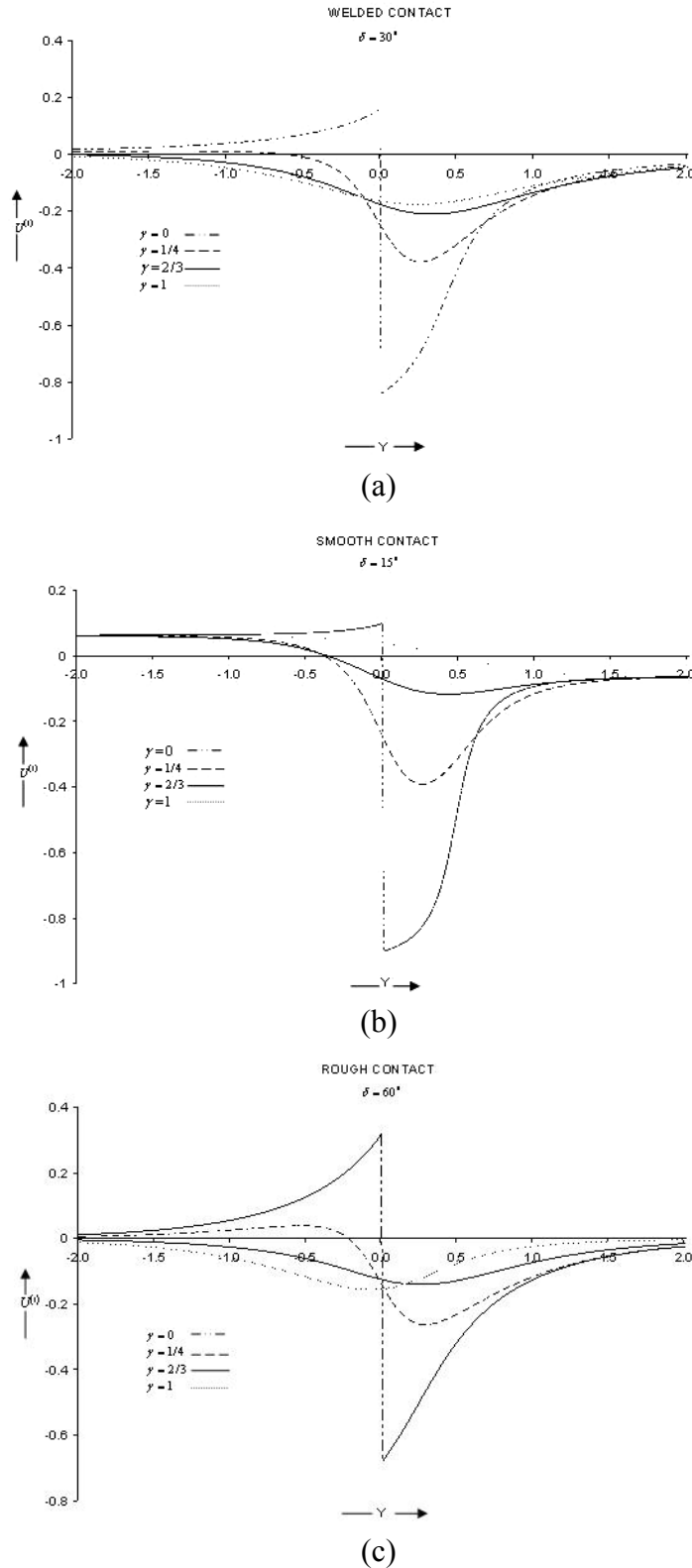


Fig. 2 (a) Variation of dimensionless surface displacement  $U^{(1)}$ , due to 'welded' contact, with the dimensionless horizontal distance  $Y$  from the upper edge of the fault for depth  $\gamma = 0, 1/4, 2/3, 1$  and dip angle  $\delta = 30^\circ$ ; (b) Variation of  $U^{(1)}$ , due to 'smooth' contact, with  $Y$  for  $\gamma = 0, 1/4, 2/3, 1$  and dip angle  $\delta = 15^\circ$ ; (c) Variation of  $U^{(1)}$ , due to 'rough' contact, with  $Y$  for  $\gamma = 0, 1/4, 2/3, 1$  and dip angle  $\delta = 60^\circ$

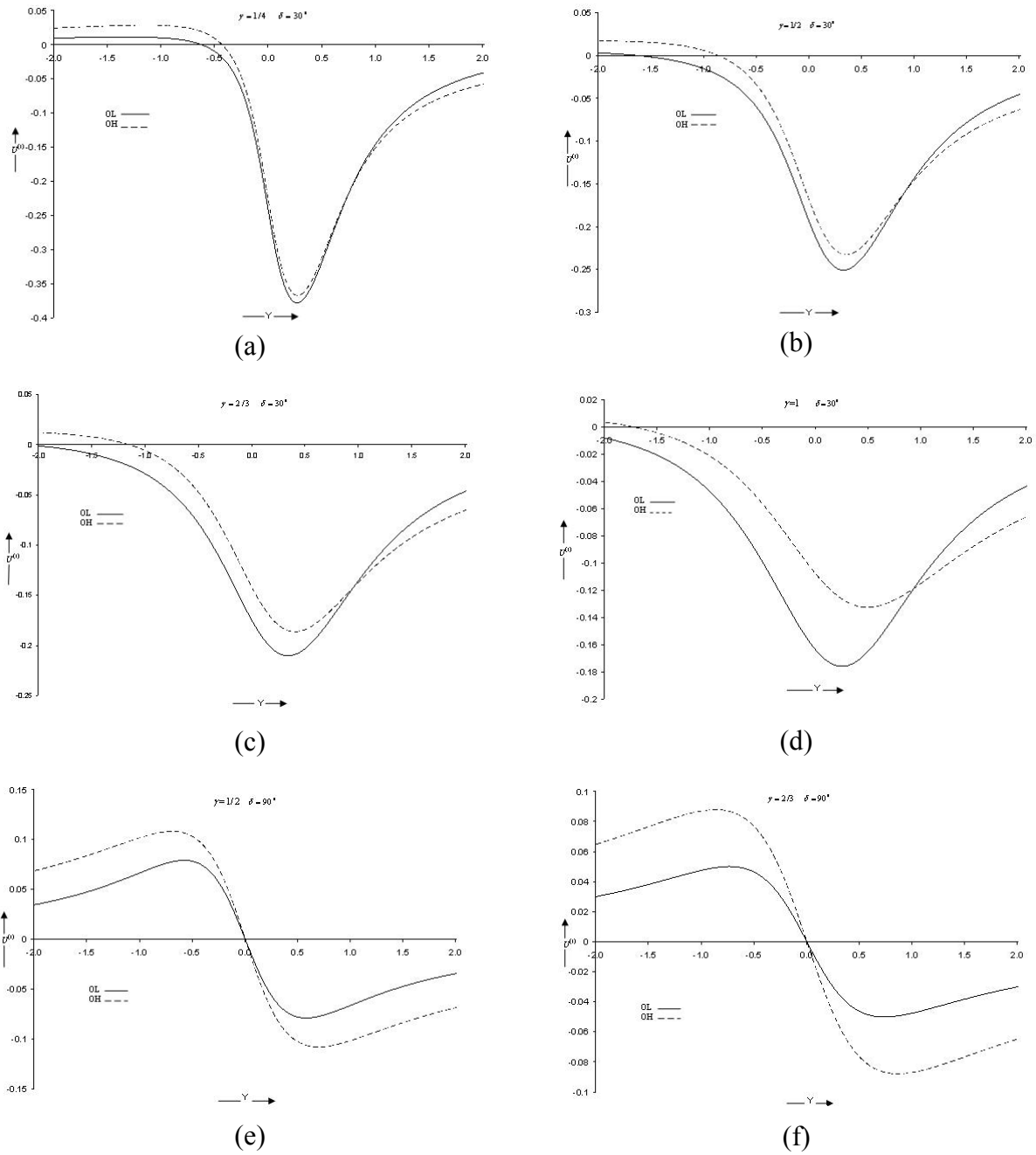


Fig. 3 (a) Variations of dimensionless surface displacement  $U^{(1)}$  due to a very long strike-slip fault for an orthotropic elastic layered half-space (OL) and for a uniform orthotropic elastic half-space (OH) with the dimensionless horizontal distance  $Y$  from the upper edge of the fault for depth  $\gamma = 1/4$  and dip angle  $\delta = 30^\circ$ ; (b) Variations of  $U^{(1)}$  with  $Y$  for an orthotropic elastic layered half-space (OL) and uniform orthotropic elastic half-space (OH) for  $\gamma = 1/2$  and  $\delta = 30^\circ$ ; (c) Variations of  $U^{(1)}$  with  $Y$  for an orthotropic elastic layered half-space (OL) and uniform orthotropic elastic half-space (OH) for  $\gamma = 2/3$  and  $\delta = 30^\circ$ ; (d) Variations of  $U^{(1)}$  with  $Y$  for an orthotropic elastic layered half-space (OL) and uniform orthotropic elastic half-space (OH) for  $\gamma = 1$  and  $\delta = 30^\circ$ ; (e) Variations of  $U^{(1)}$  with  $Y$  for an orthotropic elastic layered half-space (OL) and uniform orthotropic elastic half-space (OH) for  $\gamma = 1/2$  and  $\delta = 90^\circ$ ; (f) Variations of  $U^{(1)}$  with  $Y$  for an orthotropic elastic layered half-space (OL) and uniform orthotropic elastic half-space (OH) for  $\gamma = 2/3$  and  $\delta = 90^\circ$

From all of these figures it is found that as the depth increases, the discrepancy between the displacements due to a very long strike-slip fault for an orthotropic elastic layered half-space model and for a uniform orthotropic elastic half-space model increases. We also note that the horizontal displacement varies quite significantly in the orthotropic elastic layered model as well as in the uniform orthotropic elastic half-space model.

Curves representing the dimensionless horizontal displacement at different points of the orthotropic elastic layer, corresponding to different types of coupling, are shown in Figures 4(a)–4(c) at different combinations of depth levels and dip angles. In each figure, we observe that the displacements due to ‘welded’ coupling lie between the corresponding values due to the ‘smooth-rigid’ and ‘rough-rigid’ couplings.

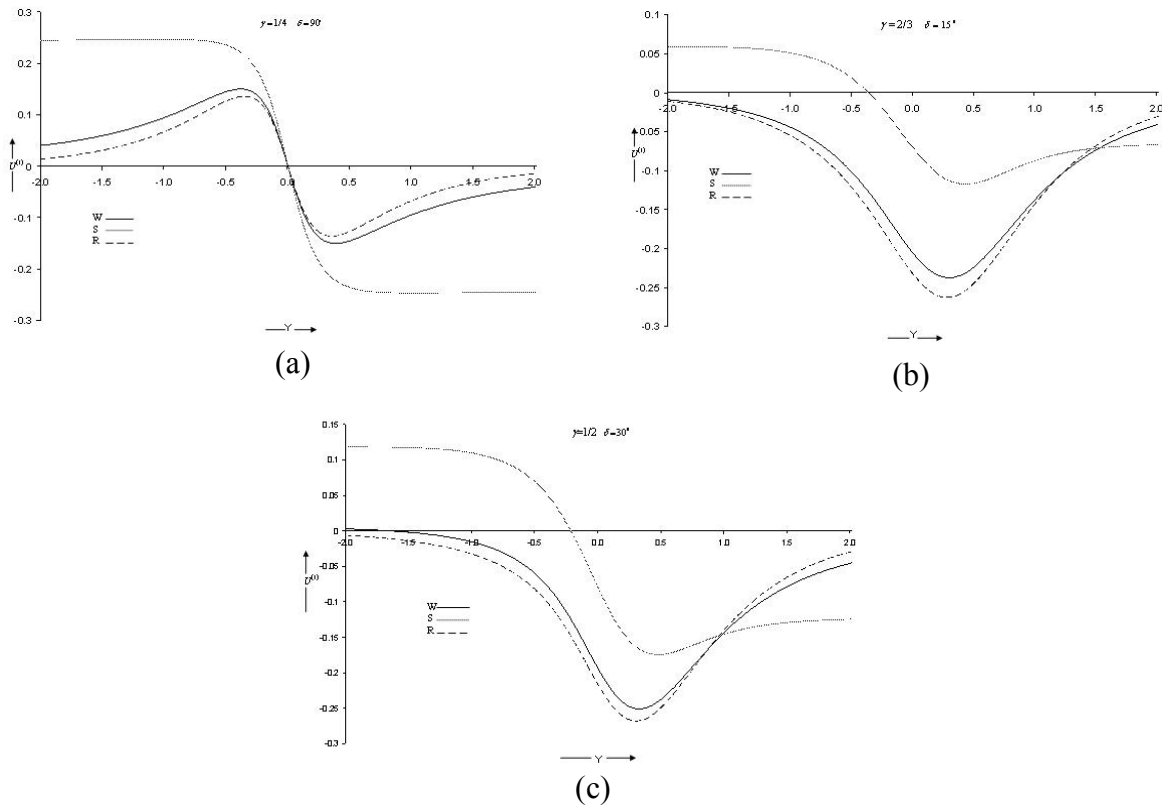


Fig. 4 (a) Variation of  $U^{(1)}$ , due to ‘welded’ contact, with the dimensionless horizontal distance  $Y$  from the upper edge of the fault for depth  $\gamma = 1/4$  and  $\delta = 30^\circ$  (W denotes ‘welded’, S ‘smooth-rigid’, and R ‘rough-rigid’ coupling); (b) Variation of  $U^{(1)}$  with  $Y$  for  $\gamma = 2/3$  and  $\delta = 15^\circ$  (W denotes ‘welded’, S ‘smooth-rigid’, and R ‘rough-rigid’ coupling); (c) Variation of  $U^{(1)}$  with  $Y$  for  $\gamma = 1/2$  and  $\delta = 30^\circ$  (W denotes ‘welded’, S ‘smooth-rigid’, and R ‘rough-rigid’ coupling)

Figures 5(a)–5(d) show the effect of anisotropy upon the variation of displacement parallel to the fault with the horizontal distance from the fault, by varying the anisotropy parameter  $\alpha$  of the elastic medium at different combinations of depth levels and angles. For an isotropic elastic medium of any kind, we have  $\alpha = 1$ . For an anisotropic medium, we consider three possibilities:  $\alpha = 0.25, 0.5, 0.75$ . In Figures 5(a) and 5(b), and in Figures 5(c) and 5(d), four curves corresponding to the anisotropy parameter  $\alpha = 0.25, 0.5, 0.75$ , and 1 (isotropic medium) are drawn at the dip angle  $\delta$  equal to  $15^\circ$  and  $30^\circ$ , respectively, for the depth levels,  $\gamma = 1/4, 1/2, 2/3, 1$ . We note that the anisotropy parameter  $\alpha$  of the source half-space has a significant effect on the displacement field.

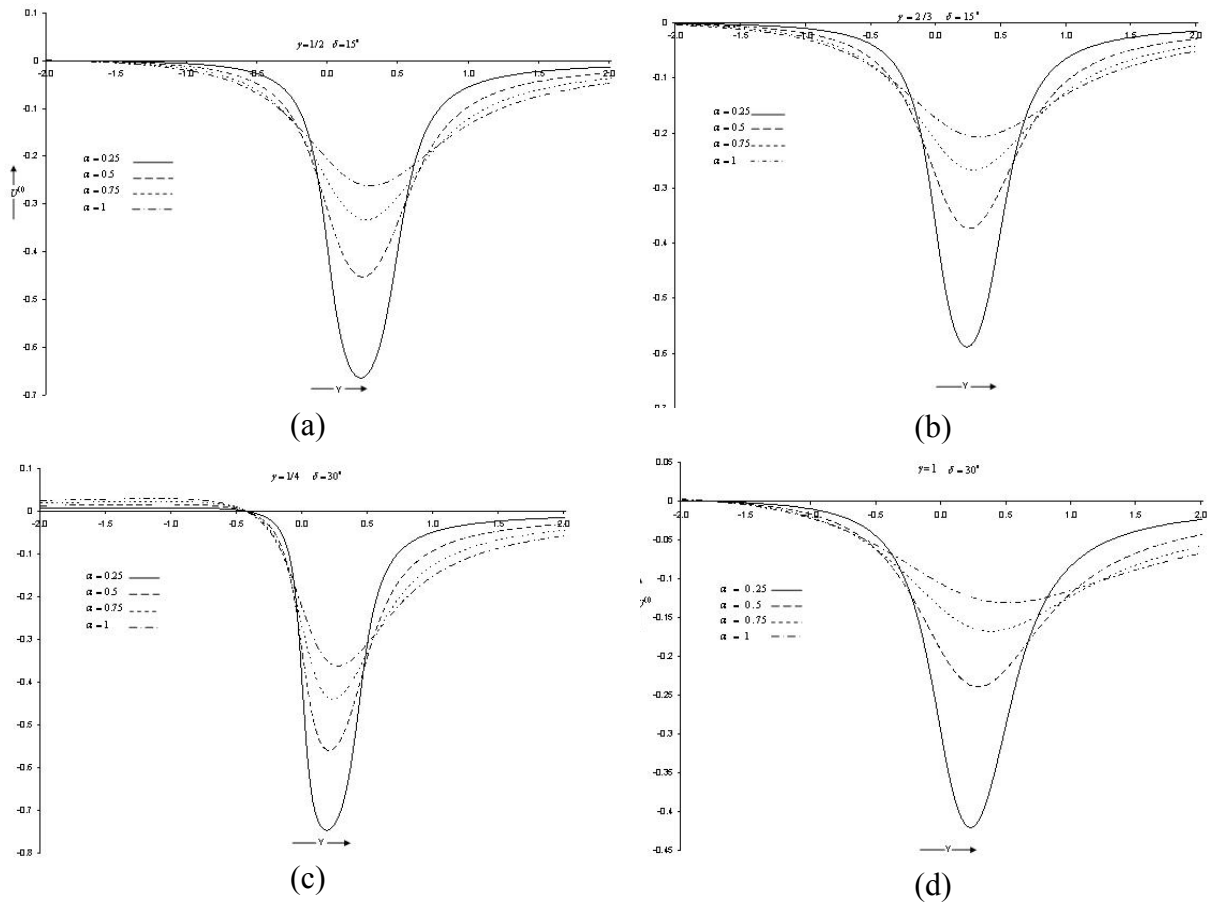


Fig. 5 (a) Variations of  $U^{(1)}$  with  $Y$  for uniform half-space with the anisotropy parameter  $\alpha = 0.25, 0.5, 0.75,$  and  $1$  (isotropic medium), for  $\gamma = 1/2$  and  $\delta = 15^\circ$ ; (b) Variations of  $U^{(1)}$  with  $Y$  for  $\alpha = 0.25, 0.5, 0.75, 1,$  with  $\gamma = 2/3$  and  $\delta = 15^\circ$ ; (c) Variations of  $U^{(1)}$  with  $Y$  for  $\alpha = 0.25, 0.5, 0.75, 1,$  with  $\gamma = 1/4$  and  $\delta = 30^\circ$ ; (d) Variations of  $U^{(1)}$  with  $Y$  for  $\alpha = 0.25, 0.5, 0.75, 1,$  with  $\gamma = 1$  and  $\delta = 30^\circ$

**DISCUSSION AND CONCLUSIONS**

In the present study, we have obtained analytical expressions for the static displacements and stresses at an arbitrary point of an orthotropic elastic layered medium, which are caused by a very long strike-slip fault situated at depth  $d$  in an orthotropic elastic layer. We have considered three cases of the contact between the layer and the half-space: ‘welded’, ‘smooth’, and ‘rough’. The displacement field for an orthotropic elastic layered half-space has also been compared numerically with the displacement field for a uniform orthotropic elastic half-space. It has been found that as the depth level increases, the difference between the two displacements also increases. Further, we have compared the displacement fields for different types of coupling, namely, ‘welded’, ‘smooth’, and ‘rough’, between the layer and the half-space. The effect of variation in depth  $d$  of the upper edge of the fault on the displacement field has also been studied numerically.

The results obtained in this paper are generalizations of our previous results (Rani and Singh, 2005), in the sense that the medium considered in the present work is orthotropic, which is more realistic than the isotropic medium. Although a 2-D model is a simplification of the physical system, such a model is useful in gaining insight into the relationship among various parameters.

Throughout most of California, earthquakes on the San Andreas fault may occur at the shallow depths of approximately 20 km (Brace and Byerlee, 1970). For the shallow earthquakes, the elastic layer of our problem may be identified with the topmost brittle region of the crust, and the welded elastic base with a crustal zone. The intermediate earthquakes of focal depths between 30 and 300 km have occurred in

Europe and elsewhere. The intermediate-depth shocks, ranging from 60 to 150 km in focal depth and with greater concentration, have been located near Granada and Malaga, Spain (Buforn et al., 1991). For the intermediate earthquakes, the model of the earth consisting of a lithosphere lying over an asthenosphere may be used. The ‘welded’ case of our problem together with the correspondence principle of linear viscoelasticity (Biot, 1954) may be used to study the intermediate earthquakes. The occurrence of deep shocks, at a depth of about 650 km below southern Spain, near Granada, is well-known. The earthquakes at great depths are fundamentally explosive in nature, involving sudden changes of volume rather than being the result of fracture involving shear (Richter, 1958).

It is well known that seismic waves radiate from faults. The Love waves may propagate in an elastic layer lying over a rigid base (Savarensky, 1975). The rigid base upon which the elastic layer lies is not absolutely rigid but may possess certain elasticity. It may be approximated to be rigid for some situations, such as for coal seam (taken as elastic layer) lying over the metamorphic rocks (taken as base). Coal seam is a class of sedimentary rocks and occurs in the Dawson County region of Montana. Krey (1963) was the first to use the Love waves to detect faults in coal seams.

Physically, the ‘smooth-rigid’ interface condition is applicable to the engineering problems, in which there is a possibility of a layer (such as a layer of petroleum materials) slipping over a base. This can also be used to study the effect of an internal horizontal boundary which is lubricated and the shear stress components and vertical component of the displacement vector become zero there.

The Palos Verdes fault is a long major strike-slip fault on the southwestern edge of the Los Angeles metropolitan area, with its slip in the sediments (Olsen and Archuleta, 1996). It has been established that an earthquake source lies in the Palaeozoic-type sedimentary rocks in Enola, Arkansas, USA (Crampin, 1994). Such sedimentary rocks may be represented in our model by a layer occupying the region  $0 \leq z < H$ , and the bottom of the layer, i.e.,  $z = H$ , may be taken as ‘rough-rigid’, so that the displacement vector becomes zero there (Small and Booker, 1984).

## ACKNOWLEDGEMENTS

Authors are thankful to the reviewers and to the Editor for their valuable suggestions on the improvement of the paper to its present form.

## REFERENCES

1. Aki, K. and Richards, P.G. (1980). “Quantitative Seismology: Theory and Methods, Volumes I and II”, W.H. Freeman and Company, San Francisco, U.S.A.
2. Ben-Menahem, A. and Singh, S.J. (1968). “Multipolar Elastic Fields in a Layered Half-Space”, *Bulletin of the Seismological Society of America*, Vol. 58, No. 5, pp. 1519–1572.
3. Biot, M.A. (1954). “Theory of Stress-Strain Relations in Anisotropic Viscoelasticity and Relaxation Phenomena”, *Journal of Applied Physics*, Vol. 25, No. 11, pp. 1385–1391.
4. Brace, W.F. and Byerlee, J.D. (1970). “California Earthquakes: Why Only Shallow Focus?”, *Science*, Vol. 168, No. 3939, pp. 1573–1575.
5. Buforn, E., Udias, A. and Madariaga, R. (1991). “Intermediate and Deep Earthquakes in Spain”, *Pure and Applied Geophysics*, Vol. 136, No. 4, pp. 375–393.
6. Burridge, R. and Knopoff, L. (1964). “Body Force Equivalents for Seismic Dislocations”, *Bulletin of the Seismological Society of America*, Vol. 54, No. 6A, pp. 1875–1888.
7. Bush, I. and Crampin, S. (1987). “Observations of EDA and PTL Anisotropy in Shear Wave VSPs”, *SEG Technical Program Expanded Abstracts*, Vol. 6, No. S11, pp. 646–649.
8. Chung, T.J. (1996). “Applied Continuum Mechanics”, Cambridge University Press, New York, U.S.A.
9. Crampin, S. (1989). “Suggestions for a Consistent Terminology for Seismic Anisotropy”, *Geophysical Prospecting*, Vol. 37, No. 7, pp. 753–770.
10. Crampin, S. (1994). “The Fracture Criticality of Crustal Rocks”, *Geophysical Journal International*, Vol. 118, No. 2, pp. 428–438.

11. Dziewonski, A.M. and Anderson, D.L. (1981). "Preliminary Reference Earth Model", *Physics of the Earth and Planetary Interiors*, Vol. 25, No. 4, pp. 297–356.
12. Fernández, J. and Rundle, J.B. (2004). "Postseismic Viscoelastic-Gravitational Half Space Computations: Problems and Solutions", *Geophysical Research Letters*, Vol. 31, No. 7, pp. L07608: 1–4.
13. Fukahata, Y. and Matsu'ura, M. (2006). "Quasi-Static Internal Deformation due to a Dislocation Source in a Multilayered Elastic/Viscoelastic Half-Space and an Equivalence Theorem", *Geophysical Journal International*, Vol. 166, No. 1, pp. 418–434.
14. Garg, N.R., Madan, D.K. and Sharma, R.K. (1996). "Two-Dimensional Deformation of an Orthotropic Elastic Medium due to Seismic Sources", *Physics of the Earth and Planetary Interiors*, Vol. 94, No. 1, pp. 43–62.
15. Hess, H.H. (1964). "Seismic Anisotropy of the Uppermost Mantle under Oceans", *Nature*, Vol. 203, No. 4945, pp. 629–631.
16. Kasahara, K. (1964). "A Strike-Slip Fault Buried in a Layered Medium", *Bulletin of the Earthquake Research Institute, University of Tokyo*, Vol. 42, No. 4, pp. 609–619.
17. Krey, T. (1963). "Channel Waves as a Tool of Applied Geophysics in Coal Mining", *Geophysics*, Vol. 28, No. 5, pp. 701–714.
18. Love, A.E.H. (1944). "A Treatise on the Mathematical Theory of Elasticity", Dover Publications, New York, U.S.A.
19. Madan, D.K. and Garg, N.R. (1997). "Static Deformation of an Orthotropic Horizontal Elastic Layer Coupling in Different Ways to a Base due to a Very Long Inclined Strike-Slip Fault Embedded in the Layer", *Indian Journal of Pure & Applied Mathematics*, Vol. 28, No. 5, pp. 697–712.
20. Maruyama, T. (1966). "On Two-Dimensional Elastic Dislocations in an Infinite and Semi-Infinite Medium", *Bulletin of the Earthquake Research Institute, University of Tokyo*, Vol. 44, No. 3, pp. 811–871.
21. Okada, Y. (1985). "Surface Deformation due to Shear and Tensile Faults in a Half-Space", *Bulletin of the Seismological Society of America*, Vol. 75, No. 4, pp. 1135–1154.
22. Okada, Y. (1992). "Internal Deformation due to Shear and Tensile Faults in a Half-Space", *Bulletin of the Seismological Society of America*, Vol. 82, No. 2, pp. 1018–1040.
23. Olsen, K.B. and Archuleta, R.J. (1996). "Three-Dimensional Simulation of Earthquakes on the Los Angeles Fault System", *Bulletin of the Seismological Society of America*, Vol. 86, No. 3, pp. 575–596.
24. Pan, E. (1989). "Static Response of a Transversely Isotropic and Layered Half-Space to General Dislocation Sources", *Physics of the Earth and Planetary Interiors*, Vol. 58, No. 2-3, pp. 103–117.
25. Rani, S. and Singh, S.J. (2005). "A Note on 2-D Lithospheric Deformation due to a Blind Strike-Slip Fault", *Journal of Earth System Science*, Vol. 114, No. 1, pp. 105–110.
26. Richter, C.F. (1958). "Elementary Seismology", W.H. Freeman and Company, San Francisco, U.S.A.
27. Rundle, J.B. (1980). "Static Elastic-Gravitational Deformation of a Layered Half Space by Point Couple Sources", *Journal of Geophysical Research*, Vol. 85, No. B10, pp. 5355–5363.
28. Rybicki, K. (1971). "The Elastic Residual Field of a Very Long Strike-Slip Fault in the Presence of a Discontinuity", *Bulletin of the Seismological Society of America*, Vol. 61, No. 1, pp. 79–92.
29. Rybicki, K. (1978). "Static Deformation of a Laterally Inhomogeneous Half-Space by a Two-Dimensional Strike-Slip Fault", *Journal of Physics of the Earth*, Vol. 26, No. 4, pp. 351–366.
30. Savarensky, E.F. (1975). "Seismic Waves", Mir Publishers, Moscow, Russia.
31. Singh, S.J. (1970). "Static Deformation of a Multilayered Half-Space by Internal Sources", *Journal of Geophysical Research*, Vol. 75, No. 17, pp. 3257–3263.
32. Singh, S.J. and Garg, N.R. (1985). "On Two-Dimensional Elastic Dislocations in a Multilayered Half-Space", *Physics of the Earth and Planetary Interiors*, Vol. 40, No. 2, pp. 135–145.
33. Small, J.C. and Booker, J.R. (1984). "Finite Layer Analysis of Layered Elastic Materials Using a Flexibility Approach. Part 1—Strip Loadings", *International Journal for Numerical Methods in Engineering*, Vol. 20, No. 6, pp. 1025–1037.

34. Talebian, M., Fielding, E.J., Funning, G.J., Ghorashi, M., Jackson, J., Nazari, H., Parsons, B., Priestley, K., Rosen, P.A., Walker, R. and Wright, T.J. (2004). "The 2003 Bam (Iran) Earthquake: Rupture of a Blind Strike-Slip Fault", *Geophysical Research Letters*, Vol. 31, No. 11, pp. L11611: 1–4.
35. Verma, R.K. (1960). "Elasticity of Some High-Density Crystals", *Journal of Geophysical Research*, Vol. 65, No. 2, pp. 757–766.
36. Wang, R., Martin, F.L. and Roth, F. (2003). "Computation of Deformation Induced by Earthquakes in a Multi-layered Elastic Crust—FORTRAN Programs EDGRN/EDCMP", *Computers & Geosciences*, Vol. 29, No. 2, pp. 195–207.
37. Wang, R., Martin, F.L. and Roth, F. (2006). "PSGRN/PSCMP—A New Code for Calculating Co- and Post-Seismic Deformation, Geoid and Gravity Changes Based on the Viscoelastic-Gravitational Dislocation Theory", *Computers & Geosciences*, Vol. 32, No. 4, pp. 527–541.